THE NANOSTRUCTURAL ROLE OF WATER IN LAMELLAR BONE AND ITS IMPLICATIONS ON OSTEONAL BONE MECHANICS: A MICROGRAPHIC AND OPTOMECHANICAL STUDY

by

Feride Şermin Utku

BSc, in Biochemistry, Earlham College, Richmond, IN., 1985

MSc, in Biomedical Engineering, Boğaziçi University, Istanbul, Turkey, 2001

Submitted to the Institute of Biomedical Engineering

in partial fulfillment of the requirements

for the degree of

Doctor

of

Philosophy

Boğaziçi University

January 18 2008

ACKNOWLEDGMENTS

I am pleased to acknowledge that the research for this thesis has been supported partially by the NIH, the National Institute of Dental and Craniofacial Research (grant RO1 DE006954 to Dr. Stephen Weiner) and partially by the Boğaziçi University Scientific Research Project (grant 05X101D to Dr. Hale Saybaşılı).

I would kindly like to thank all members of my immediate and extended family for making life all the more meaningful and lively by showing support during this challanging period; Prof. Turkan Kumbaracı-Gardenier, Doris B. Stebbins and Ripley Tracy for their contribution to my pedagogic and personal formation; Şeküre Coral and Aysel Kumbaracı for teaching us that "Alim'in bilgisinin kıyılarında gezineyim diye, bilginin erişiminin de idrakiyle, kurgulanmış bir sınavdan, hevesle gidiyorum bir diğerine"; Prof. Stephen Weiner for his extensive advice and support through each and every step of this research; advisor Prof. Hale Saybaşılı and co-advisor Assis. Prof. Can Yücesoy for co-funding this research and advising; Dr. Eugenia Klein for demonstrating her expertise on the ESEM; Prof. John Currey for guiding us through bone mechanics with his extensive knowledge on bones; Prof. Yorgo Istefanopoulos for displaying a pro-active approach on behalf of his students; Prof. Yekta Ülgen, Prof. Mehmet Özkan, Assoc. Prof. Özcan Halil Gülçür, Prof. Dr. Önder Aydıngöz, Assoc. Prof. Şebnem Özüpek, Prof. Ron Shahar, Prof. Lia Addadi and BME secretariat and staff for their kind support and collaboration; Dr. Paul Zaslansky and Dr. Meir Barak for the long hours on the ESPI, the long discussions on the results and for their solidarity; BME research assistants for their kind friendship and help during my doctoral course; and finally Işık, Pelin, Esim, Necbah and Ahmet for making the world a warm and lovely place to live in through their "on-line" presence.

ABSTRACT

THE NANOSTRUCTURAL ROLE OF WATER IN LAMELLAR BONE AND ITS IMPLICATIONS ON OSTEONAL BONE MECHANICS: A MICROGRAPHIC AND OPTOMECHANICAL STUDY

The microstructural organization of water in bone was investigated using the environmental scanning electron microscope to analyze the dimensional changes that occur during dehydration of equine osteonal bone. In longitudinal sections, 1.2% contraction perpendicular to the lamellae, 0% parallel to the lamellae; in transverse sections,1.4% contraction both parallel and perpendicular to the lamellae were observed. Scanning electron microscopy back scattered electron images showed that about half of an individual lamella is less mineralized, thus more hydrated, indicating that contractions perpendicular to lamellae are due to the presence of more water-filled rather than mineral-filled channels within the mineralized collagen fibril arrays. As these channels are also aligned with the crystal planes, the crystal arrays facilitate or hinder contraction in different directions. The mineralized collagen fibril arrays, laid down in the form of primary circumferential lamellar bone are replaced with secondary osteonal lamellar bone. The mechanical properties of these two types of lamellar bone are studied to understand how bone functions under load during the remodelling process. Twenty minipig cortical bone samples were tested using an optomechanical testing system. Deformation of tissue after each 2-micrometer compression increment was detected orthogonally in-plane (x,y) and out-of-plane (z). Linear regression of stress and strain of partially remodelled bones gave an E_1 and ν_{12} of 7.9 $\pm$ 2.1 GPa and 0.3. The circumferential lamellar bone had an average E_1 of 9.4 $\pm$ 2.0 GPa compared to the average E_1 of 6.8 $\pm$ 0.8 GPa for the osteonal bone.

Keywords: environmental scanning electron microscope, mineralized collagen fibril, bone water, electronic speckle pattern interferometry, mechanical properties of compact bone.

ÖZET

LAMELER KEMİĞİN NANOYAPISINDA SUYUN KONUMU VE OSTEONAL KEMİK MEKANİĞİNE ETKİLERİ: MİKROSKOPİK VE OPTOMEKANİK YÖNTEMLERLE İNCELEME

Suyun taze kemikteki yapısal organizasyonun incelenmesinde, çevresel taramalı elektron mikroskobu kullanılarak kemiğin kurutulması sırasında oluşan boyut değişimine bakılmıştır. Dikey kesitlerde, lamellere dikey yönde %1.2, lamellere paralel yönde %0 kısalma; yatay kesitlerdeyse, her iki yönde de %1.4 kısalma görülmüştür. Çevresel taramalı elektron mikroskobunun geri dağılımlı elektron detektörü görüntüleri lamellerin yarısında daha az minerallenme, daha fazla su bulunduğunu göstermiştir. Bu nedenle, lamellere dik yöndeki kısalmanın, mineralize olmuş kolajen fibrili dizileri arasında mineral yerine daha fazla su dolu kanalların bulunması nedeniyle olduğunu öneriyoruz. Kanalların, rotatif kontraplaklar şeklinde modellenmiş lameler kemikteki kristal yüzeylerine paralel olmaları nedeniyle, kristal dizileri değişik yönlerdeki kısalmayı yönlendirmekte ya da engellemektedir. Minerallenmiş kolajen fibrili dizilerinin oluşturduğu primer çepersel lameler kemiğin yerini, daha sonra ikincil osteonal lameler kemik alır. Bu iki tür lameler kemiğin mekanik özellikleri, kemiğin yeniden modellenme sırasında yük altındaki işlevini anlamak amacıyla incelenmiştir. Yirmi minipig kortikal kemik örneğinin 2-mikrometrelik deplasman kademeleri sırasında oluşan yük altında gösterdiği deformasyon, ortogonal olarak düzlem içi (x,y) ve düzlem dışı (z) yönde optomekanik yöntemle incelenmiştir. Stress ve gerinimin lineer regresyonu sonucunda kısmen modellenmiş kemikte ortalama E_1 ve ν_{12} değerleri 7.9 $\pm$ 2.1 GPa ve 0.3 olarak bulunmuştur. Çepersel lameler kemikte E_1, ortalama 9.4 $\pm$ 2.0 GPa, ve osteonal kemikte E_1, ortalama 6.8 $\pm$ 0.8 GPa olarak bulunmuştur.

Anahtar Sözcükler: çevresel taramalı elektron mikroskop, minerallenmiş kolajen fibrili, kemikteki su, elektronik benek tarama girişim ölçer, kompakt kemiğin mekanik özellikleri.

TABLE OF CONTENTS

LIST OF FIGURES

LIST OF TABLES

LIST OF SYMBOLS

E	Elastic Modulus
G	Shear Modulus
ν	Poisson Ratio
Å	Angstrom
ϵ	Normal Strain
γ	Shear Strain
α	Alpha
σ	Normal Stress

LIST OF ABBREVIATIONS

HAp	Hydroxyapatite
OCP	Octocalcium Phosphate
GAG	Glycosaminoglycan
PGs	Proteoglycans
ECM	Extracellular Matrix
ESEM	Environmental Scanning Electron Microscope
ESPI	Electronic Speckle Pattern Interferometer
SMD	Sterred Molecular Dynamics
NMR	Nuclear Magnetic Resonance
LS	Longitudinal Section
TS	Transverse Section
HS-PG	Heparan Sulphate-Proteoglycan
IR	Infrared
US	Ultrasound
EM	Electron Microscope
XRD	X-Ray Diffraction
PV	Vascular Porosity
PLC	Lacunar Canalicular Porosity
PCA	Collagen Apatite Porosity
IC	Cellular Interface
ILC	Lacunae Canaliculi Interface
Gly	Glycine
Pro	Proline
hPro	Hydroxyproline

1. INTRODUCTION

Biomineralization is the formation of minerals by organisms. It is a process observed widely among the prokaryotes and eukaryotes, involving more than 60 different minerals [1]. The early phase of biomineralization dates back to 3.5 billion years ago in the Precambrian, preceding the age of visible life. The biologically induced biomineralization, where ions are secreted from the cell into the environment, where they form insoluble precipitates into minerals, started around 1.6 billion years ago. Biologically controlled biomineralization, where crystals form in the vesicles, spicules, etc. started around about 1.5 billion years ago. Composite skeletal formation was observed around 570 million years ago, most probably involving the construction of organic scaffolds composed of macromolecules to control the mineralization process. In this period, the evolution of biomineralization branched into biogenic carbonate, biogenic phosphate and biogenic opal evolution, all taking place at about the same time in the different taxonomic groups. The fish emerged about 470 million years ago, as jawless fish, and continued to evolve as nonteleost bony fish to teleost fish about 65 million years ago. The amphibians evolved around 350 million years ago, leading to reptiles evolving on land around 285 million years ago. The mammals began their evolution about 200 million years ago. The birds were last to evolve around mid-Jurassic about 170 million years ago [1].

The concern of this study, the Chordata, use phosphate ions in biomineralization, probably as a means to maintain temporary storage of large amounts of this ion, highly needed in the energy metabolism. In the bone, the hydroxyapatite crystal (brittle-mineral), collagen (elastic-organic) and liquid (water) are organized into hierarchical structures which give the necessary strength, within an elastic and light material. Just like straw has been used in the manufacture of bricks for fiber reinforcement to increase strength and to maintain structural integrity since the Chalcolithic age, bone as a complex composite material with excellent adaptation properties, designs its mineral particles and fibrous organic components according to the local mechanical demands.

Bone tissue varies in composition to embody different mechanical properties in different locations of the organism. The composition of the three basic elements of biomineralization within the bone varies according to the environmental conditions and mechanical demands, e.g. birds and fish, which require lightness in the air and water. Although less mobile chordates contain mainly primary parallel-fibered bone and circumferential lamellar bone, animals of higher mobility seem to have evolved to have remodelled osteonal bone. As increased mobility implies higher fracture risk, the lighter, better hydrated bone, where collagen integrity is maintained, may provide features to the organisms, which, under the constraint of microstructural (modelling/remodelling of bone tissue) and biomechanical concerns (attachment of muscles, connective tissues) and aiming to save energy during movement by limiting mass under space-constrained conditions, survive as a result of the adaptation of structural design to meet functional requirements in a mechanically viable solution.

As a structure that has both biomechanical and biochemical importance for the organism, the mineral and organic components of bone have been investigated extensively both with respect to their structural organization and in terms of their contributions to the mechanical properties of bone [2, 3, 4, 5] using various invasive and non-invasive methods since late 1800's, and recently, the optomechanics technology, which has enabled researchers to perform non-contact optical measurement and obtain information about the meso-scale dynamic behavior of wet bone samples to carry out both qualitative and quantitative point and field analysis. However, the third component, water, although it clearly is an integral part of the structure [6, 7, 8, 9] and plays an important role in the mechanical properties of bone and ossified tissues is less well understood [10, 11, 12, 13].

This doctoral thesis focuses both on bone microstructure and bone biomechanics and studies not only the role of water in bone by examining the effect of dehydration on the lamellar microstructure of equine osteonal cortical bone with a particular emphasis on the location of water within the organization of collagen fibrils and carbonated hydroxyapatite crystals, but also how bone functions under load during the remodelling process, the formation of osteonal bone from circumferential lamellar bone, laid down

on periosteal and endosteal surfaces as primary lamellar bone. In the bone biomechanics section of this study, we aim to understand how the elastic moduli, the Poisson's ratio and the strain distribution in bone differ between the completely osteonal minipig bone and bone that contains both the circumferential and osteonal sections adjacent to one other, by optomechanically testing the proximo-anterior minipig tibial cortical bones and investigating the variation in strain and elastic modulus distribution between circumferential lamellar bone and osteonal bone. Discourse of this thesis covers the basics of bone components, bone microstructure, the interdependency of bone porosity and hydration, the effect of dehydration on osteonal bone, the mechanical properties of bone and how the two types of bone deform under load.

2. MICROSTRUCTURE of BONE

2.1 Components of Bone

Bone is a viscoelastic, fiber reinforced, anisotropic composite material. The three major components of mature bone are Type I collagen (the bulk of the organic matrix), carbonated hydroxyapatite (the mineral) and water, which are organized into a hierarchical structure. The relative proportions of these three major components may vary within the bone, thus making it also a graded material [14]. The hierarchical organization of bone components has been modeled to consist of seven levels: at level 1, are the hydroxyapatite crystals and collagen fibrils; at level 2, is the mineralized collagen fibril; at level 3, mineralized fibrils form an array; at level 4, fibril arrays form patterns making the various types of collagen scaffold; at level 5, osteonal structures are observed; at level 6, trabecular and compact bone tissues having different porosities are formed; and at level 7, the whole bone is observed [14].

2.1.1 Collagen

Collagen is the most abundant animal protein, making up about 25% of proteins in humans. Collagen is secreted by the connective tissue cells, i.e. chondroblasts, fibroblasts and osteoblasts. There are more than 20 different types of collagen molecules. Type I collagen, found mainly in the skin and the bone is the most common type. Type I, II, III, V and XI collagen are found in the connective tissue. Type IX and XII are fibril-associated collagens, linking the collagen fibrils and other molecules in the extracellular matrix. Types IV and VII are network-forming collagens, where Type IV collagen forms a basal lamina by assembling into a sheet and Type VII collagen anchors the basal lamina to the connective tissue [15].

A collagen molecule is made up of an alpha chain of amino acids, mainly glycine

and proline. Each one of the alpha chains has been coded by a separate gene, forming 25 different chains. Glycine, Gly, the smallest amino acid, is regularly repeated at every third residue, forming the backbone of the triple helical molecule, leaving the glycine molecule inside the helix as the chain winds around. Proline, Pro, with its ring structure stabilizes the helical conformation. In the Type I collagen in bone, the third major amino acid is hydroxyproline, hPro. The Gly - Pro - hPro triplet increases the thermal stability of the polypeptide chain by 15°C, adjusting flexibility of collagen at body temperature [16].

The organic material in bone consists mainly of 90% collagen and 10% PGs [17]. Type I tropocollagen molecule, the basic scaffold of bone tissue, is secreted as a helical rod by the osteoblast, and is oriented and aligned [18] according to the local shear and tangential strain pattern in bone [4]. A Type I tropocollagen molecule consists of three left-handed helices of approximately 1000 aminoacids, containing repetitions of Gly - Pro - hPro triplets. Two of the chains are α 1 helices, while the other one is an α 2. The N- and C- propeptide ends of the tropocollagen molecule, marked by non-helical domains, are cleaved off, allowing the right handed coiling of left handed triple helical rods to form a collagen molecule of 300 nm in length and 1.5 nm in diameter, with a helical repeat length of 8.6 nm (Fig. 2.1) [15]. Five triple helical collagen molecules are then arranged in a linear staggered array named as the Hodge-Petruska model (Figs. 2.2 and 2.3) to form a microfibril, where the head and tail of each collagen molecule are 64 - 70 nm apart, with a hole of about 35 nm in between [19, 6]. Associations between polar side groups also contribute to the known displayed arrangement of collagen. Aldehyde deriven cross-links have been shown to occur at a ratio of 3.5:1 between an α1 or an α2 chain [20]. Lysyl and hydroxylysyl groups located at the C and N terminals are condensed by lysyl hydroxylase forming a divalent bond, a reducable ketoimine cross-link, which, reacting with another hydoxylysyl aldehyde forms pyrodinoline, a trivalent crosslink. Hydroxylysyl aldehyde may react with non-hydroxlated lysine to form another enzymatic cross-link, pyyrole. Cross-linking by glycation occurs non-enymatically by the reaction of lysine and arginine with glucose, resulting in aldimine linkage, which rearranges itself into an Amadori product, a more stable keto-imine linkage. Advanced glycation end-products may occur with other

amino acid residues over time [21].

Collagen molecules are packed stereospecifically concentrically in a quasi-hexagonal lattice in cross-section to form a microfibril, stabilized by covalent cross-links; however, the exact full 3D arrangement is still debatable. The microfibril, with a diameter of approximately 3.5 nm, grows by fusion of shorter intermediaries to form collagen fibers, embedded in a proteoglycan-rich matrix [22, 23, 24]. Many models for collagen packing have been suggested specifically in the orderly packed rat tail tendon. Packing of microfibrillar substructures, where the microfibrils may have supercoiled or straight-tilted [25], quasi-hexagonal and generalized, with fibers organized in rhomboids, have been suggested based on data for equatorial diffraction spacing of collagen as a function of water content [26]. The two-dimensional liquid structure model is based on the observation that in a liquid model as the density of molecules decreases, the molecular spacing increases, with the collagen spacing is shown to be regular in the axial direction, but irregular in the lateral direction, as has been observed in 2D fluid computer simulations, which support the observation that collagen spacing behaves liquidlike as wet and quasi-hexagonal as dry [27].

2.1.2 Extracellular Matrix

The extracellular matrix (ECM) of collagenous tissues, produced by fibroblasts, chondroblasts and osteoblasts, consist of water, proteoglycans with polysaccharide chains of glycosaminoglycans (GAGs), fibrous proteins, such as collagen and elastin, more than 200 types of non-fibrillar collagens and globular cell adhesion proteins, such as laminin and fibronectin, containing binding sites for ECM proteins and cell surface receptors and laminin binding heparan sulphate proteoglycan (HS-PG), perlecan, osteonectin and chondroitin sulphate PGs [28].

Proteoglycans, make about 1% of cortical bone. They are classified according to the type of attached GAG chain molecules, as chondroitin sulphate, dermatan sulphate, heparin and heparan sulphate and keratan sulphate. GAGs are unbranched polysaccha-

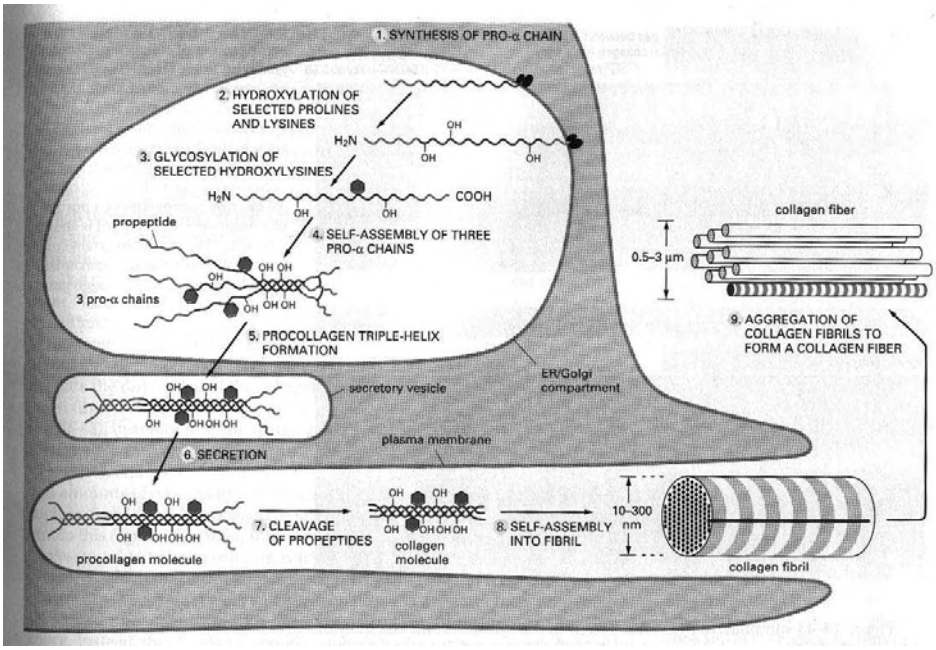

Figure 2.1 Collagen fibril formation. Collagen fibril formation from the basic unit of helical collagen molecule as pro-α chain. Hydroxylation and glycosylation is followed by the self assembly of three pro-α chains forming the procollagen triple helix molecule in the ER/Golgi apparatus. Post secretion from the cell and cleavage of propeptides, collagen fibrils are self-assembled in the extracellular space, within an infolding of the plasma membrane. Reproduced from [1].

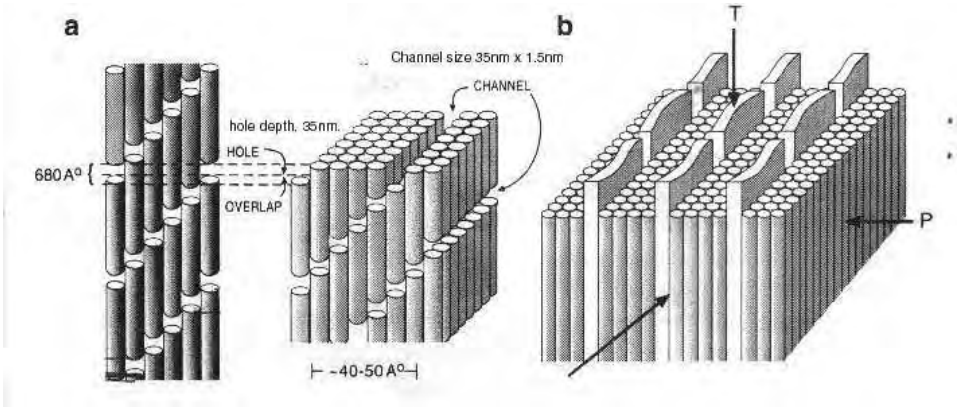

Figure 2.2 Schematic of collagen array. The stagger-array pattern of collagen triple helical molecules. (a) A gap of about 35 nm is formed by a stagger pattern of 68 nm., leaving holes which will form channels. (b) Stacking of collagen triple helical molecules to form channels, in which the hydroxyapatite crystals are located. (c) Mineralization of collagen fibril within the 3D framework of the 2D Hodge - Petruska model of collagen stagger array. T and P show tranverse and periosteal faces of the bone. The schematic is not drawn to scale. Reproduced from [2].

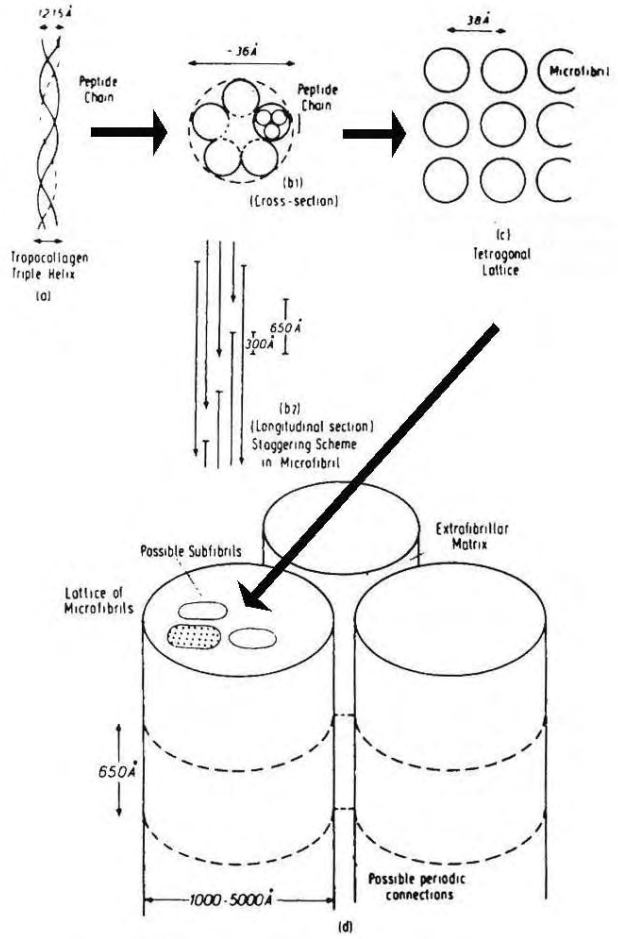

Figure 2.3 Schematic showing the organization of collagen molecules from the triple helix to microfibril to collagen fibril. (a) The tropocollagen molecule, (b1) the microfibril in a cross-sectional view, (b2) in axial view, (c) lattice of microfibrils (Reprinted with permission of John Wiley and Sons, Inc.) [3].

ride chains with repeating disaccharide units of an amino sugar (N-acetylglucosamine or N-acetylgalactosamine) with sulphate groups and uronic acid (glucuronic or iduronic acid). GAG chains are distinguished from one another based on the type of sugar residues and their linkages and the number and location of sulphate groups. The high number of negative charges make GAGs highly hydrophilic, attracting cations and water. At physiological pH, GAG chains contain one to three negative charges. Where as hyaluronan is excreted by an enzyme in the cell membrane, GAGs are synthesized in the cell and released into the matrix by exocytosis. Hyaluronate interacts with PGs to form versican, aggrecan in the musculoskeletal system. Despite their small quantity in bone, PGs are strongly hydrophilic and can form hydrogen bonds with water 1000 times their volume and thus provide resistance to compressive loading. Hyaluronan

has a capacity to bind to large amounts of water and fill large volumes as well [29].

2.1.3 Mineral

The third component of bone that water associates with is carbonated hydroxyapatite, also known as dahllite, plate-shaped crystal, with typical dimensions of 50 x 25 x 1.5 - 4.0 nm. (measured by small angle X-ray scattering (SAXS)) and hexagonal crystal symmetry [14, 24]. The unit cell dimension in the a axis direction is 9.37 Å, thus the crystals of 20 - 50 Å thickness are only a few unit cells thick. The size of HAp crystals is still controversial, estimated to be much longer than 50 nm. as a single crystal can extend along the entire length of the groove. The unit cell of the carbonated hydroxyapatite crystal consists of $Ca_{10}(PO_4)_6(OH)_2$. About 4 - 6% of the phosphate is replaced by carbonate and, at lower percentages, by fluoride and aluminum ions. It is always calcium deficient and contains CO_3^{-2} and HPO_4^{-2} ions in the crystal lattice [30]. Therefore, the general formula may be $Ca_{8.3}(PO_4)_{4.3}(CO_3)_x(HPO_4)_y(OH)_{0.3}$, where y decreases and x increases with age, (x+y) remains constant around 1.7. Mineral forms about 50 to 85% of the dry and degreased weight of the bone. Carbonated hydroxyapatite crystal may grow from octocalcium phosphate (OCP) which contains a hydrated layer that carbonated hydroxyapatite crystals lack. The exact shape of the crystals, needle shaped vs. plate-like has also been controversial, the differences cited in the literature are likely to be due to sample preparation processes and imaging angle. The electrostatic forces about the mineral attract more than 35 mg water per gram of mineral [31] forming a water layer on each side of the crystal as was shown using NMR [32, 33]. The strongly adsorbed water layer may not only lubricate the crystal-collagen interface, but also contain an excess of calcium ions which balance the phosphate and carbonate ions on the crystallite surface [34].

2.1.4 Water

Water content of bone has been studied using thermogravimetric, calorimetric, mechanical and dielectric methods, XRD, IR, US, EM, NMR and dynamic mechanical spectroscopy. An average 10 - 12 wt% of cortical bone and 20% of bone matrix consist of water [8]. The three main components of bone, collagen, other ECM constituents and mineral associate chemically with water.

Nomura et al. [6] identify four types of water in bone: structural water, forming hydrogen bonds within the triple helix of collagen molecules (0 - 0.07 g/g), water bound to the polar side chains (of glycine, hxdroxyproline, carboxyl and hydroxylysine) and located in the interhelical regions (0.07 - 0.25 g/g), water in a transition region where both bound and free water are absorbed (0.25 - 0.45 g/g), and free water (>0.45 g/g)). Marzec and Warchol [35] have used dielectric spectroscopy to identify four types of water based on the ranges of temperatures and the activation energies as: up to 50°C, 17 kJ/mol, up to 120°C, -39 kJ/mol, and up to 200°C, -12 kJ/mol for wet bone and state that in dry bone, the activation energy of 50 kJ/mol at 100°C, indicates the release of strongly bound water. Pineri et al. [7] add another group of water (0.010 g/g) evaporated at 10^{-4} Torr at 100°C (Table 2.1).

Listed in Table 2.1, Regimes I and II are structural water and intimately bound water respectively, which, due to their strong association with the triple helix molecules and the phosphate and calcium groups of the mineral, are almost impossible to remove even at very high temperatures and under vacuum. Removable water in bone tissue, Regimes III - V, is part of the extracellular matrix consisting of PGs, collagen and the mineral apatite surface, and the lacunar-canalicular and vascular porosities respectively. Regime V consists of the bulk water within the microfibrils and the vascular system and can be easily evaporated [36].

Table 2.1
Types of Water Regimes in Bone.

Regime	Absorp	Desorp	Characteristics	Suggested Mechanism
I	0-0.010		Water extractable at 100°C under 10^{-4} Torr, high energy of fixation (>18 kcal/mol), distinct sites, nonrotationally hydrated water.	Triple hydrogen bonding inside the triple helix and involving hydroxyproline.
II	0.010-0.070	0.010-0.110	Heat of sorption; 17 kcal/mol, heat of desorption; 18 kcal/mol, no change in equatorial spacing, small changes in the rigidity modulus, beta peak corresponding to an exchange reaction involving the water molecules, decrease in temperature of the gamma peak position, nonrotationally hydrated water (NMR).	Double hydrogen bonding of the water molecules in the available sites inside the triple helix.
III	0.071-0.235	0.110-0.235	Heat of sorption; 14 kcal/mol, heat of desorption; 12 kcal/mol, large increase in the modulus, large changes of the equatorial spacing, no change of the beta peak, nonrotationally hydrated water (NMR).	Double hydrogen bonding of the water molecules between the triple helix and between the microfibrils.
IV	0.235-0.50	0.235-0.50	Heat of sorption and desorption 9 kcal/mol, no change in the modulus at low temperatures, no large change in equatorial spacing, new peak at 225°K, mobile water molecules (NMR).	Water fixed by one hydrogen bond between the microfibrils or water fixed in the hole zones adjacent to the end of the tropocollagen molecule.
V	>0.50	>0.50	Alpha peak at 273°K, large decreases in modulus at 273°K, appearance of freezing bound state for water corresponding to 0.54 g water/g collagen (NMR) and 0.48 (calorimetric), no further change in IR spectrum	Free water between microfibrils.

Compiled from Pineri et al., 1978 (Regime I) and Nomura et al., 1977 (Regimes II-V)

2.2 Formation and Mineralization of the Collagen Scaffold

2.2.1 Microstructure and Hierarchical Organization of Osteonal Bone

The microstructure of bone displays collagen fibers with carbonated hydroxyapatite crystals, living cells (osteocytes, osteoblasts and osteoclasts), lacunae (which contain the osteocytes), blood vessels and canals (canaliculi, Haversian and Volkman) which contain these vessels and nerves. Bone structure organizes its organic and mineral matrix from the lowest scale, i.e. the collagen fibril and the mineral, to the highest, i.e. the bulk bone, based on the mechanical needs of the tissue [37, 38, 39]. Therefore, the outer shell of bone providing support needed for the mobility for the organism, has a more compactly organized (parallel-fibred bone) collagen scaffold than the interior, which, depending on the amount of weight to be supported and distributed, may be organized more trabecularly. Cancellous (trabecular) bone is a highly porous compact bone found at the ends of the long bones and at the endosteum. The rounded ends of the long bones, as a result of their large volume, reduce the amount of stress and provide support against loads by orienting its trabeculae in the direction of maximum load over time. [30].

2.2.2 Collagen Scaffold Formation

Ossified tissue formation basically is the process of mineralization of a protein/glycoprotein scaffold, formed by various cells producing the mesodermal tissue, i.e. fibroblasts, chondroblasts and osteoblasts. In bone, scaffold formation takes place through two different processes: endochondral and membraneous. The basic molecular mechanisms of ossification being similar, these two different mechanisms allow bone tissue to grow and ossify longitudinally on a cartilaginous scaffold (endochondral) and circumferentially on a collagenous scaffold (membraneous).

The cartilaginous matrix of bone is deposited by the mesenchymal cells, which have differentiated into chondroblasts. In the diaphysis region of the bone, the outer

layer of the matrix, perichondrium, mineralizes into the periosteum shaft with two large masses of cartilage at the ends (epiphyses). Mineralization of the cartilage continues along the midshaft, and along with mineralization, angiogenesis and collagen producing osteoblastic cell generation continues circumferentially and axially. Endochondral scaffold formation continues as the ossification of the preexisting cartilage of the epiphyseal plate with four zones: first, most proximally, resting cartilage, with randomly distributed chondrocytes; second, the zone of chondrocyte multiplication, where cells line up in rows parallel to the long axis of the bone; third, zone of chondrocyte with hypertrophy, cells enlarging and beginning to disintegrate; and fourth, zone of cartilage calcification, with mineralized bone replacing the disintegrating cartilage. Bone elongation continues till the epiphyseal plates are completely replaced by ossified tissue [40].

In membraneous scaffold formation, the osteoblasts are involved. They are the bone forming cells derived from the blood vessels and the bone-lining cells, which cover the surface of the bones, the periosteum. The layer of mesenchymal tissue surrounding the developing bone, the periosteal sheath, gives rise to further osteoblasts and adds new concentric layers of ossified bone. The collagen fibrils are laid down around the blood vessels in various orientations by the osteoblasts. As the organic matrix is deposited, the osteoblasts embed themselves in the tissue in cavities (the ossified lacunae) and connect with each other through gap junctions through the canaliculi. The maintenance of already formed bone tissue takes place by the resorption of less hydrated, brittle and micro-cracked parts, which change the strain pattern in the tissue by the osteoclasts. The osteoclasts, multinucleated cells which originate from precursor cells in the blood, form tight seals and dissolve the bone tissue within that seal by the acids they secrete. The dissolved tissue then is packed in vesicles and transported through the cell body. The osteoclasts and osteoblasts, which compose the bone forming unit (bfu), collaborate with each other in the resorption and deposition of bone.

New collagen scaffold is then deposited by the osteoblasts [40, 30] forming the various bone types, i.e. woven bone, parallel-fibred bone and lamellar bone. Woven bone is formed mainly in the two main phases of life, i.e. in the fetus/young animals and

during bone repair. Woven bone scaffold, which is comparable to a felt-material, with irregularly placed fibers, is made very quickly, proceeding at a speed of four micrometers a day. In order to cover up a large area as quickly as possible with minimal material, collagen fibrils are laid down randomly, without an orientation (Figure 2.4a), making it quite porous, highly mineralized and brittle [30]. Parallel-fibred bone is typically found in bone sections in the outer shell of the bone, where support is needed. Contrary to woven bone, it has an orderly arrangement of collagen fibrils. Fibrils, oriented parallel to each other form the sub-lamellae, are set-off at approximately at an 80 degree angle to one another and are more mineralized than lamellar bone [30]. Lamellar bone replaces woven bone at a rate of one micrometer a day. It consists of orderly arranged fibrils making the scaffold set at specific orientations. The collagen fibrils are arranged as layers, or lamellae, with the general orientation of fibrils within a lamella varying to form a rotated plywood arrangement of sub-lamellae (Fig. 2.4b), where the angle between the fibrils of each sub-lamella varies coarsely around 30^{o} as well as the crystal planes in the fibrils of each sub-lamellae (Fig. 2.5) [30, 41, 42]. Circumferential lamellar bone displays collagen fibrils, arranged in sublamellae which are set at approximately 30^{o} angles from one another. It is categorically seen in reptiles, mammals and birds. Osteonal lamellar bone is formed, when, for mechanical and biochemical/metabolic reasons, the originally deposited primary bone may be resorbed and replaced by the later deposited secondary bone, which forms itself in the shape of osteons, with Haversian systems. Osteonal lamellar bone seems to exist in larger mobile animals, which demand minimum material with optimum strength. Fibro-lamellar bone, also known as plexiform bone, is typically seen in large animals, such as, bovine. It is a combination of lamellar bone and woven bone, where the boundaries between the lamellae are made of the brittle woven bone [30].

2.2.3 Mineralization of Collagen Scaffold

Bone mineralization involves the localization of mineral formation, the mineralogical identities of the first mineral precipitates, the continued growth of crystals inside the collagen fibrils (in the gaps and/or grooves) and the possibility of direct

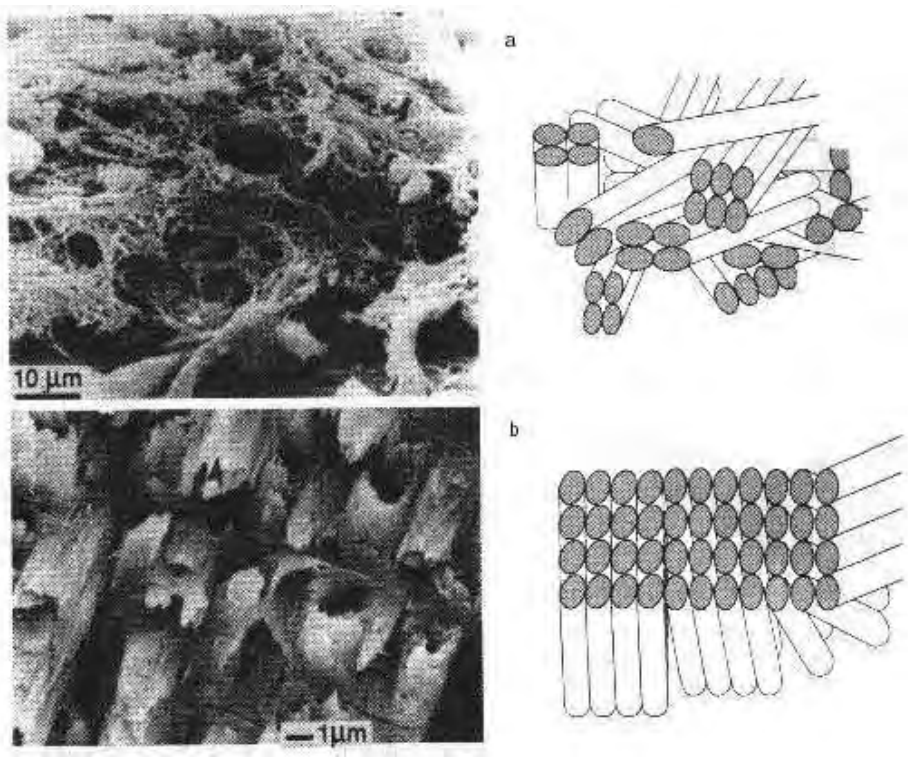

Figure 2.4 Various collagen fibril scaffold arrangements of bone. (a) Woven bone microstructure; (b) rotated plywood structure in lamellar bone. Modified from [4].

crystal-crystal contacts [1]. The mineralization process is facilitated by the organic molecules of the ECM 24 hours after collagen secretion by osteoblasts into the EC space, where they self-assemble into a three dimensional framework. The acidic proteins are directly secreted by a different pathway into the site of mineralization, where ions diffuse through the permeable collagen matrix to the mineralization sites. The mineral precipitates from a saturated solution [1]. The osteoblasts, which form the mother liquor, actively pump ions of choice into the mineralizing compartment or allow passive diffusion of specific ions as needed, into the solution in a controlled sequence, i.e. calcium first enters the ECM followed by phosphate after a significant lapse of time. Acidic matrix glycoproteins first associate with calcium ions and fold into their ordered conformations. In order to prevent sudden nucleation with the introduction of the anion, the acidic matrix glycoproteins probably interact with the mineral in its transition phase as amorphous calcium phosphate (ACP) stabilizing it and preventing from converting to the crystalline phase suddenly. ATP and Mg have also been shown to prevent transition from ACP to HAp [1].

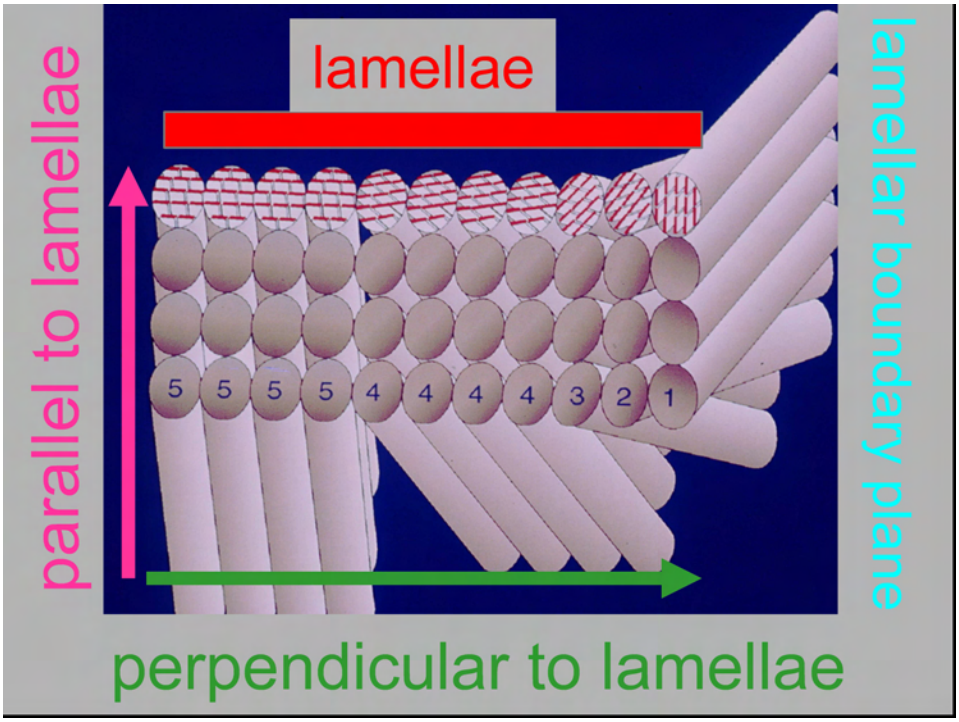

Figure 2.5 Schematic illustration of the five sublayer rotated plywood model for lamellar bone. The five sublayers have differences in thickness, reflecting the features unique to baboon lamellar bone. The crystals in the collagen fibrils are oriented at different angles to form the rotated plywood feature of sub-lamellae. The extent of crystal rotation is arbitrarily depicted. Modified from [5].

ECM molecules with highly complex nucleation sites may induce formation of multi or single crystal nucleation as is seen in bone. When the atomic (lattice) arrangement in the substrate matches the lattice arrangement of the nucleating phase nucleation occurs by epitaxy, the oriented overgrowth of one crystalline phase on the face of another. During crystal growth, relatively unstable crystal faces are formed as the acidic glycoproteins in the solution specifically interact stereospecifically with a set of crystal faces. In bones and teeth crystal growth stops when the crystals come into contact with the formed surface of the matrix. To date, bone crystals have not been observed in the act of formation.

In bone, the initial precipitate is in the form of ACP, which then forms OCP, which acts as a template upon which HAp nucleates. X-Ray diffraction patterns indicate that the c-axis (002) is fast growing direction in HAp [1]. In mineralized turkey tendon, TEM, X-Ray and neutron diffraction studies of the mineralizing zone show that the first formed crystals are in the collagen gap regions at a sharply defined locus

and continue to overlap zones between the collagen molecules directed by cross-links between the collagen triple helices [27]. Crystal growth taking place rapidly within the gap/groove volume inside the fibrils account for about two-thirds of the final mineral content (Fig. 2.2). TEM stereomicrographs of individual isolated collagen fibrils also show that plate-shaped crystals are located at the gap level. The models of collagen fibril organization predict that extended groves arranged in parallel rows are formed with lengths and thicknesses of about 36nm and 1.5nm and widths running along the fibril diameter length [43]. The average equatorial spacing of collagen molecules being 1.5nm, only a single crystal may occupy this void. As 40% of water in the non-mineralized bone matrix is located between the fibrils, water is expected to be replaced with mineral at these sites [8]. TEM results show the presence of crystals oriented with their c-axes parallel to the long axis of the collagen molecules in the overlap region of the fibrils (Fig. 2.2). Structural water may still remain either in the crystal lattice, substituting for OH^- [34] or as ordered layers of structural water sandwiched between the mineral and organic collagen fibers [32, 33].

Water content of ossified tissue is related to its mineralization, hydration and collagen fibril arrangement. Using X-ray diffraction, the equatorial spacing, i.e. the distance between the triple helical molecules of mineralized turkey leg tendon was found to have intermediate values between fresh and dry unmineralized collagen indicating that as water was replaced with mineral, the lateral spacing of the collagen fibrils gets more compact due a reduction in water-filled space between molecules and that upon rehydrating the freeze-dried calcified and non-calcified tendons, original dimensions were attained (Table 2.2). Mineralized and nonmineralized wet and dry collagen fibrils displayed only lateral contraction without any change in the axial direction [44, 45, 46, 27].

Table 2.2
Principal Equatorial Reflection Spacing from Turkey Leg Tendon (TLT)

	Fresh TLT		Freeze-dried TLT		Rehydrated TLT	
	Calcified	Noncalcified	Calcified	Noncalcified	Calcified	Noncalcified
Mean Value	13.3 Å	14.4 Å	11.3 Å	11.2 Å	13.7 Å	15.4 Å
Range	12.6 - 14.1 Å	14.1 - 14.7 Å	11.0 - 11.8 Å	10.9 - 11.4 Å	13.1 - 14.6 Å	14.9 - 16.2 Å
Number of Samples	7	4	5	5	5	5
Level of Significance			not significant $0.7>p>0.6$		highly significant $0.01>p>0.001$	

Compiled from Eanes et al. 1970, 1976.

2.3 Porosity and Hydration of Bone

2.3.1 Porosity of Bone

Porosity of bone is very intimately related to its hydration, which is achieved via the vascular system by fluid diffusion mechanisms. There are three levels of bone porosity within the cortical and cancellous bone, and two interfaces between the three levels of porosity have been suggested [36]. The porosities in bone are filled with blood, bone fluid or trabecular substances. The fluid residing outside the vessels is referred to as bone serum, while the ECM is filled with the extracellular fluid. The porosities in bone can be categorized as the vascular porosity (PV), the lacunar-canalicular porosity (PLC) and the collagen-apatite porosity (PCA). The PV, with an approximate diameter of 20 micrometers contains the vascular and nerve systems and the bulk water as categorized by Pineri et al. and Nomura et al. [7, 6]. Total PV volume is less than PLC volume (1.8%). The PV blood pressure in bone is around 40-60 mm Hg. PLC porosity size is around 0.1 micrometer, the radius of the canaliculi. The bone fluid in PLC can sustain high pressures arising from mechanical loading for long periods [36]. Probably due to the smallness of its lineal dimension, the PLC fluid pressure is greater than that of PV, PLC fluid provides a transition range enabling an easy exchange of bulk with bound water. The PLC fluid, containing the osteocytes, the osteocytic processes and cell glycocalyx is thought to behave as a gel [36]. PCA has a porosity of 10 nm radius. Associated with the PGs in the ECM, the crystal and collagen in PCA is bound

and structural water, found to be about 7% canine cortical bone volume [9]. There is negligible movement of bone fluid as the structural water is associated with the ionic crystal [32, 33]. Associated with the trabecular bone, is the largest lineal dimension of bone porosity, 1 mm., the inter-trabecular porosity (PIT), containing bone marrow, fat and blood vessels, with a twice as much viscosity than bone fluid (Fig. 2.6).

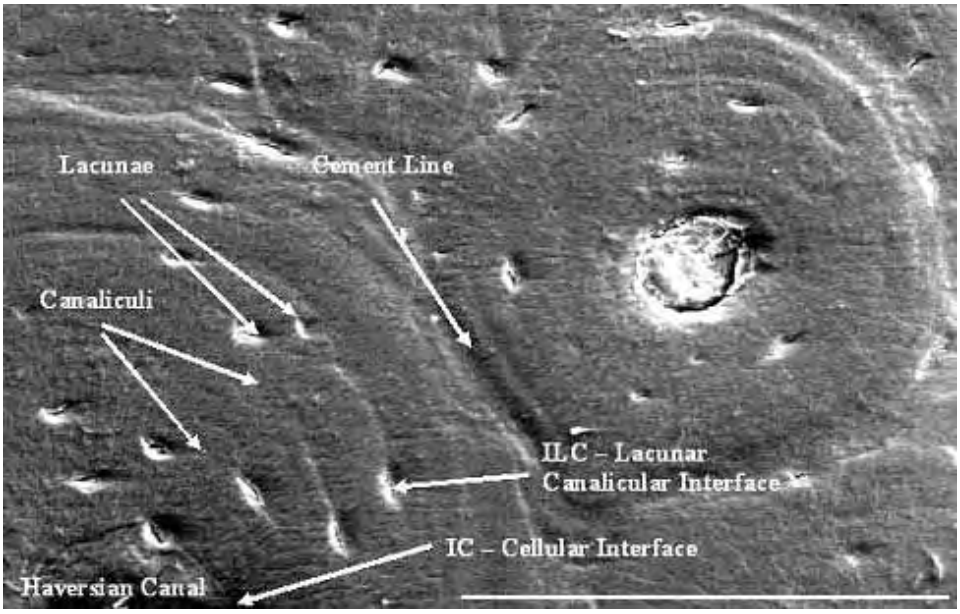

Figure 2.6 Porosity of compact bone. Image showing the various porosities and interfaces observed in bone; the Haversian canal with the blood vessel lined with the IC, connecting the osteocytes in their lacunae and lined with the ILC, are the canaliculi reaching the cement line. The connections between the osteocytes are to be imagined as a 3D network of connections between the cells. Scale bar, 50 micrometers.

2.3.2 Hydration of Bone

Adequate hydration of bone tissue is achieved by the positive blood pressure gradient and the complex vascularization network, and manifests itself both at the nanoscale and the microscale. At the nanoscale, it maintains the integrity of both the collagen by preventing the triple helices from unwinding and forming direct inter-helical bonds [47] and the mineral by associating with the charged groups of bone mineral (PO_4^{-3} or Ca^{+2}) and acting as a lubricant increasing the flexibility of the crystal [34]. At the microscale, bone hydration determines bone mechanical viscoelastic properties. As mineralization replaces bone water, the more mineralized tissue contains less bound water reducing the viscoelastic properties of bone, while improving its strength [8].

The movement of bone fluid between the porosities is governed by the interfaces that exist between them. These interfaces are the periosteum, the cellular interface (IC), the interface of the lacunae and the canaliculi (ILC) and the cement lines. The periosteum covers the outer surface of the bone and consists of an outer layer with collagenous fibers and fibroblasts and an inner layer with multilayered, differentiated bone cells. Highly vascularized, it acts as an outer sheath preventing bone fluid outflow. The IC is a continuous layer of bone lining cells with tight junctions coating the vascular structure. Transient pressure gradients across the interface transport the fluids through the interface, where during bone loading the blood serum mixes with the bone ECM fluid. IC hydraulic conductivity may be altered by Ca^{+2}, calcitonin, cAMP and parathyroid hormone. The ILC may be quite porous at birth and decrease its porosity as it becomes ossified. In mature bone, the ILC is relatively impermeable to even very small solutes of MW 300 - 400. Actually, in young animals larger discrete pores exist with spacings similar to the canaliculi. At the boundary of secondary osteons, cement lines contain lipids, different concentrations of collagenous proteins, mineral and proteoglycan that the osteoid does not [36, 48].

2.4 Materials and Methods Used in Microstructural Studies

In this section of the thesis, we studied the structural role of water in lamellae by measuring the extent of contraction of osteonal lamellar bone in different directions during dehydration and rehydration using an ESEM. Since the water content of bone is inversely proportional to its level of mineralization [8], we also studied the variations in mineralization in lamellae using a scanning electron microscope with two different backscattered electron detectors. In this way, we studied different depths of the specimen using primary electron beams of different energies.

2.4.1 Environmental Scanning Electron Microscope (ESEM)

XL30 ESEM-FEG Microscope (FEI) at the Weizmann Institute of Science, Electron Microscopy Unit, Rehovot, Israel, was used to study the effects of dehydration on structural changes in bone as a function of changing relative humidity (rh). The ESEM achieves control of relative humidity by controlling vapor pressure in the observation chamber using the isobar charts for different temperature settings. During the course of this study, the temperature and voltage were kept stationary at 5°C and at 10kV. ESEM with FEG allows high-resolution secondary electron imaging of samples at pressures up to 10 Torr and at temperatures up to 1000°C using Schottky field emission source as electron gun at voltages ranging from 0.2 to 30kV. Non-conductive samples can be examined without any coating at different humidities.

2.4.2 Materials Used in ESEM Imaging

Fresh and fresh frozen bone samples of approximately 1 cubic mm. of entirely osteonal bone were obtained from the cranial section of the third metatarsal of a 5 yr. old female Arab horse and an 11 yr. old male horse.

2.4.3 Methods Used in ESEM Imaging

2.4.3.1 Sample Preparation for ESEM Imaging. Fresh-frozen samples were thawed and cut using a diamond saw, exposing either the surface perpendicular to the bone long axis (the transverse section) or parallel to the long axis and the natural surface of the bone (the longitudinal section). Bone samples were prepared by the author by initially grinding the surface and then polishing with 5-micrometer, then 1-micrometer diamond paste and finally 0.05-micrometer alumina paste. Polished samples were then kept refrigerated.

2.4.3.2 Image Acquisition Using the ESEM. The images were acquired by the author and Dr. Eugenia Klein from the Weizmann Institute of Science, Electron Microscopy Unit. In each wet sample three to ten sites were selected for imaging at 350X and/or 1200X magnifications. The exact coordinates for these sites were recorded for re-imaging under the below mentioned rehydration conditions. These specific sites were first imaged wet at 100% rh (6.5 Torr) (referred to as wet). They were then dried at 0% rh (0.1 Torr) for 60 minutes (referred to as dry). The same sites were re-imaged as the samples were rehydrated either to 28% rh (1.9 Torr) and/or to 42% rh (2.9 Torr). After each change in conditions, the samples were allowed to equilibrate for 45 minutes. All samples were fully rehydrated back to 100% rh (6.5 Torr) (referred to as completely rewet) and imaged. Various magnifications and pressures were tested on the first sample (EQL404a) in order to find an optimum setting for the remainder of the experiments. One of the longitudinally sectioned samples studied by ESEM (Sample EQL202a) was further examined by scanning electron microscope back-scattered electron imaging (SEM-BSE), in order to visualize differences in the degree of mineralization within the lamellae.

(a) Longitudinally Sectioned Samples

i - Sample EQL404a :

Sample EQL404a was first examined at 6.5 Torr and images of 6 different regions of interest (ROI) were taken at 800X, 1600X and 3200X magnification. Pressure was then lowered to 0.1 Torr, maintained there for 45 min. and increased slightly (1.9 Torr) to allow adequate visualization and image acquisition. After a 45-minute period of rehydration, images were taken. The same procedure was repeated at 2.9 Torr. In order to determine the amount of mineralization, GSE and BSE images were taken at 1600X and 3200X magnification.

ii - Sample EQL404b :

Results of sample EQL404a indicated that repeatability was higher at 800X to 1200X magnification, since at higher magnifications a higher percentage of error is more probable. Therefore, in EQL404b, only 800X, 1200X and 1600X magnification were used. As a control, two sets of images of the wet sample were taken wet at 6.5 Torr. Pressure was then lowered to 0.1 Torr and maintained there for 45 minutes. Better-defined images were taken at 2.9 Torr. Sample was rehydrated for 45 minutes, during which, images of the rehydrating sample as well as the rehydrated images were taken.

Table 2.3
List of Images - Sample EQL404a.

404a	Wet			Dry (1.9 Torr)			Dry (2.9 Torr)			Rewet			BSE/GSE	
ROI	800	1600	3200	800	1600	3200	800	1600	3200	800	1600	3200	BSE	GSE
1	1,2			9			17			32			42	41
2	3			11	10		18,19			33			43,45	44,46
3	4			12			20			34			48	47
4	5			13			21			35			51(800) 53(6400)	49,50(800) 52(6400)
5		6			14			22			36		55(1600)	54(1600)
6			7			15			23			37	57(3200)	56(3200)
7		8			16			24			38		59(1600) 61(3200	58(1600) 60(3200)

Table 2.4
List of Images - Sample EQL404b.

404b	Wet			Dry (2.9 Torr)			Rewet			
ROI	800	1200	1600	800	1200	1600	800	1200	1600	Extra
1	3,11			18,21,22			32,37			21
2		2,1			20,23			33,38		
3			9			19,24			34	
4	4,13			25						
5		5,12			26			35,39		
6			14			28				
7	6,15			29						52,53
8		7,16			30			36,4		
9			8,17			31				

iii - Sample EQL303a :

Measurements from sample EQL404b indicated that 800X magnification was too low, therefore, in EQL303a 1000X and 1200X magnifications were used. Four sets of images of the wet sample were used as controls at 6.5 Torr. Pressure was then lowered to 0.1 Torr and maintained there for 45 minutes. Well-defined images were taken at 1.9 Torr. Sample was rehydrated for 75 minutes.

Table 2.5
List of Images - Sample EQL303a.

303a	Wet		Dry (1.9 Torr)		Rewet	
ROI	1200x	1000X	1200x	1000X	1200x	1000X
1	1,2,3,5	4,6	13	14	31	32
2	7	8			48	49
3	9	10			50	52
4	11	12			53	54
5			15	16	33	34
6			17	18	35	36
7			19	20,21	37,38,39	40
8			22	23	41,42	43
9			24	25	44	45
10			26	27	46	47

iv - Sample EQL303b :

Measurements from sample EQL303a indicated that 1200X magnification was adequate. One set of images of the wet sample was used as control at 6.5 Torr. Pressure was then lowered to 0.1 Torr and maintained there for 45 minutes. Well-defined images were taken at 1.9 Torr. Sample was rehydrated for 45 minutes.

v - Sample EQL202a :

Only 1200X magnification was used. One set of images of the wet sample was taken as control at 6.5 Torr. Pressure was then lowered and maintained at 0.1 Torr for 45 minutes. Images were taken at 1.9 Torr. Sample was rehydrated for 45 minutes.

Table 2.6
List of Images - Sample EQL303b.

303b	Wet	Dry (1.9 Torr)	Rewet
ROI	1200 X	1200 X	1200 X
1	1	12	
2	2	13	
3	3	14	
4	5	15	
5	6	16	
6	7	21	
7	8	17	
8	9	18	29
9	10	19	
10	11	20	

(b) Transversely Sectioned Samples

i - Sample EQL404c :

In order to see the larger picture and the changes taking place throughout the sample, images of 9 ROI were taken both at 350X and 1200X at 100% rh as wet. Pressure was then lowered to 0.1 Torr and maintained there for 45 minutes. Better-defined images were taken at 2.9 Torr. Sample was rehydrated for 45 minutes, during which images of the rehydrating sample as well as the fully rehydrated images were taken.

ii - Sample EQL202c :

In the imaging of sample EQT202c only 1200X magnification were used. Ten sets of images of the wet sample was taken at 6.5 Torr. Pressure was then lowered to 0.1 Torr and maintained there for 45 minutes. Well-defined images were taken at 1.9 Torr. Sample was rehydrated for 45 minutes.

Table 2.7
List of Images - Sample EQL202a.

202a	Wet	Dry (1.9 Torr)	Rewet
ROI	1200 X	1200 X	1200 X
1	1	12	
2	2	13	
3	3	14	
4	4	15	
5	5	16	
6	6	17	
7	7	20	
8	8	21	27
9	9	22	
10	11	23	

2.4.3.3 Analysis of ESEM Images. The changes in the lamellar structure of five longitudinally and two transversely sectioned sample were studied. Data points, as percent change in length, were collected from 59 sites (n=1451) and 20 sites (n=672) from longitudinal and transverse sections respectively. Haversian canals, lacunae and lamellar striations were used as landmarks to choose the two points between which the distance will be measured (referred to as a "measurement"). Only measurements longer than 15 micrometers were included in the data as the precision decreased significantly for shorter distances. In longitudinal sections (Fig. 2.7), lengths perpendicular to lamellae (radial to the long axis of the bone), and parallel to the lamellae (along the long axis of the bone); and in transverse sections (Fig. 2.7), lengths radial and tangential to the osteon were measured. Note that in a transverse section, radial and tangential segments are the respective equivalent of segments perpendicular and parallel to the lamellae in a longitudinal section. In both longitudinal and transverse sections lengths across the cement line were also measured (Fig. 2.12).

The length of a measurement in a dehydrated sample (Fig. 2.8b) was subtracted from its wet length (Fig. 2.8a). The difference was divided by the original wet length and multiplied by 100 to obtain the percent change in length. The percent change in length for each bone sample were then averaged and standard deviations

Table 2.8
List of Images - Sample EQT404c.

404c	Wet		Dry (2.9 Torr)		Rewet	
ROI	350	1200	350	1200	350	1200
1	1		21			
2	2		22			
3	3		23			
4	4		24			
5	5		25			
6	6		14		36	
7		7		13		27-35
8	8		15		37	
9		9		16 (2400)		38
10	10		17		40	
11		11		18,19		41
12		12		20		42

were calculated. Positive values indicated contraction of tissue upon dehydration.

$$Change(\%) = \frac{L_w - L_r}{L_w} 100 \tag{2.1}$$

where L_w and L_r refer to wet and dehydrated length respectively. Sites in which osteons intersected the section obliquely were avoided in order to observe only orthogonally cut lamellae. In longitudinal sections (Fig. 2.7a), segments perpendicular to lamellae (radial to the long axis of the bone), and parallel to lamellae (along the long axis of the bone); and in transverse sections (Fig. 2.7b), segments radial and tangential to the osteon were measured.

2.4.3.4 Statistical Analysis of ESEM Data. Averages, standard deviations (sd), the minima and maxima of the measurements under each condition were determined. As the homogeneity of variance was established between the compared groups, data with normal and skewed distributions were statistically analyzed using a parametric

Table 2.9
List of Images - Sample EQT202c.

202c	Wet	Dry (1.9 Torr)
ROI	1200X	1200X
1	1	12
2	2	13
3	3	14
4	4	15
5	5	16
6	6	17
7	7	18
8	8	19
9	9,10	20
10	11	21

test, Student's t-test for large samples, and a non-parametric test, Mann-Whitney U-test respectively. Differences were considered significant at $p<0.05$.

2.4.3.5 (SEM-BSE) Back Scattered Electron Imaging . The longitudinally sectioned sample (EQL202a), initially prepared by the author, and further prepared for SEM-BSE imaging at the Weizmann Institute of Science Electron Microscopy Unit by Dr. Eugenia Klein, was imaged under the supervision of Prof. Dr. Steve Weiner. The sample was prepared by grinding it to 20-30 micrometer pieces and embedding in a high-conductive epoxy resin (Polymer adhesive EP75-1, Master Bond Inc., Hackensack, New Jersey) in order to minimize electron charging. It was then polished following the above described procedure for ESEM sample preparation and coated with a 2 nm layer of chromium and imaged in a Zeiss Ultra 55 (Carl Zeiss NTS GmbH) with two BSE detectors: Quadra (QBSD; a solid state detector able to detect electrons with energies 5 keV and higher and an EsB in-lens detector that detects every electron backscattered in the direction of the primary beam, with energies high enough to overcome the potential of the grid (Steigewald) (from 448 eV to 4000 eV).

2.5 Results

2.5.1 ESEM Secondary Electron Imaging

2.5.1.1 Control Groups. The key issue in this study, the reproducibility of the measurements, depended on the time it took for a sample to reach equilibrium after each change in the relative humidity conditions, as well as the imaging quality in the ESEM, which is a function of both the relative humidity and the measurement reproducibility. Therefore, two different sets of control data were obtained: for measurement reproducibility and for experimental reproducibility. Data used to determine measurement reproducibility were obtained from a total of 19 sites (n=251) and 4 sites (n=125) from longitudinal and transverse sections respectively. The measurement reproducibility was determined using Adobe Photoshop within an image and between images taken under the same condition to determine presence of any drifts in experimental settings. The error of measurement within an image showed a standard deviation of ± 0.09% (n=25) for a wet sample and ± 0.07% (n=25) for a rehydrated sample. The error of measurement between the two images of the same site taken under the same rh conditions was 0.19% ± 0.20% (n=10). Images of wet and completely rehydrated samples were compared (this comparison is referred to as control data) to ensure that length changes were reversible and that the samples had reached equilibrium with the new relative humidity conditions. Various equilibration times (5-60 minutes) at a specific site were tested at five minute intervals to determine that no further change took place after 35 minutes. Another indication that equilibrium was reached was that the reproducibility of these measurements were lower than those obtained without changing humidity conditions. In longitudinal sections, the control data showed an average change in length of -0.37% ± 1.24% (n=110) perpendicular to the lamellae and -0.19% ± 1.31% (n=91) parallel to the lamellae. In transverse sections, the average radial change between wet and completely rehydrated samples was 0.11% ± 0.32%. The experiment was repeated using fresh unfrozen bones at 28% rh to obtain results for the direction perpendicular to lamellae of 1.51% ± 0.72% (n=22) and parallel to the lamellae of -0.20% ± 0.32% (n=19), which correlate with the results for fresh frozen specimens, showing that the freeze-thaw process for bone does not affect the manner

in which it contracts during dehydration.

2.5.1.2 Longitudinal Sections. Significant length changes perpendicular to lamellae were observed. Table 2.11 compares these length changes and the significance values for measurements perpendicular and parallel to lamellae. The observed length changes during rehydration perpendicular to lamellae were much greater than the reproducibility of the measurements of control data (-0.37% $\pm$ 1.24%). However, the length change parallel to the lamellae was almost the same as the control data (-0.19% $\pm$ 1.31%), showing that the lamellae respond to altered humidity anisotropically. There is an angular dependence vis a vis the lamellar boundaries, where the highest contraction is perpendicular to the lamellar planes (Fig. 2.9). The length changes as a function of the angle a segment of a given length intercepts with the lamellar front demonstrate that contraction in the tissue is a function of not only the number of lamellae but also the less mineralized sublamellae included within that segment. A hypothetical analysis was performed on the correlation between the number of more mineralized and less mineralized sublamellae and the amount of contraction observed. With a calculated contraction of 10% in the less mineralized collagen fibril and assignment of different weights to more and less-mineralized sublamellae at the ratios of 3:2, 4:1, 4.05:0.95, 4.3:0.7, 4.4:0.6, 4.45:0.55, and 4.55:0.45, the respective calculated contractions of 4%, 2%, 1.9%, 1.4%, 1.2%, 1.1% and 0.9% were attained. Details of this analysis are listed in Table 2.10 for a contraction of 1.4% and graphed in Fig. 2.10.

2.5.1.3 Transverse Sections. Radial and tangential length changes in transverse sections are listed in Table 2.12. Note that in transverse sections, radial measurements are the equivalent of those perpendicular to lamellae in longitudinal sections and tangential measurements are almost the equivalent of those parallel to lamellae. The results showed that in contrast to the longitudinal section results, in transverse sections significant contraction took place in both the radial and tangential directions, such that at 28% rh, they were almost equal ($pT<0.45$).

Table 2.10
Hypothetical Distribution of Percent Length Change vs. Number of More and Less Mineralized Lamellae Contained in the Length

more min. lam.	less min. lam.	unit length mml.	unit length lml.	weight mml.	weight lml.	contracted length	original length	% length change
12	12	1	0.9	4.3	0.7	59.16	60	1.4
12	11	1	0.9	4.3	0.7	58.53	59.3	1.298
11	12	1	0.9	4.3	0.7	54.86	55.7	1.508
11	11	1	0.9	4.3	0.7	54.23	55	1.4
11	10	1	0.9	4.3	0.7	53.6	54.3	1.289
10	11	1	0.9	4.3	0.7	49.93	50.7	1.519
10	10	1	0.9	4.3	0.7	49.3	50	1.4
10	9	1	0.9	4.3	0.7	48.67	49.3	1.278
9	10	1	0.9	4.3	0.7	45	45.7	1.532
9	9	1	0.9	4.3	0.7	44.37	45	1.4
9	8	1	0.9	4.3	0.7	43.74	44.3	1.264
8	9	1	0.9	4.3	0.7	40.07	40.7	1.548
8	8	1	0.9	4.3	0.7	39.44	40	1.4
8	7	1	0.9	4.3	0.7	38.81	39.3	1.247
7	8	1	0.9	4.3	0.7	35.14	35.7	1.569
7	7	1	0.9	4.3	0.7	34.51	35	1.4
7	6	1	0.9	4.3	0.7	33.88	34.3	1.224
6	7	1	0.9	4.3	0.7	30.21	30.7	1.596
6	6	1	0.9	4.3	0.7	29.58	30	1.4
6	5	1	0.9	4.3	0.7	28.95	29.3	1.195
5	6	1	0.9	4.3	0.7	25.28	25.7	1.634
5	5	1	0.9	4.3	0.7	24.65	25	1.4
5	4	1	0.9	4.3	0.7	24.02	24.3	1.152
4	5	1	0.9	4.3	0.7	20.35	20.7	1.691
4	4	1	0.9	4.3	0.7	19.72	20	1.4
4	3	1	0.9	4.3	0.7	19.09	19.3	1.088
3	4	1	0.9	4.3	0.7	15.42	15.7	1.783
3	3	1	0.9	4.3	0.7	14.79	15	1.4
3	2	1	0.9	4.3	0.7	14.16	14.3	0.979
2	3	1	0.9	4.3	0.7	10.49	10.7	1.963
2	2	1	0.9	4.3	0.7	9.86	10	1.4
							Ave.	1.412
							Sd.	0.202

min. lam.=minearalized lamellae, mml.=more mineralized lamellae, lml.=less mineralized lamellae

Table 2.11
Length Changes in Longitudinal Sections as a Function of Relative Humidity.

	Perpendicular to Lamellae (radial in transverse sections)				Parallel to Lamellae (axial)			
Relative Humidity	Ave (%)	Min (%)	Max (%)	Significance (U Test)	Ave (%)	Min (%)	Max (%)	Significance (U Test)
28%	1.19 ± 0.8 (n=359)	-0.30	8.02	p<0.0005	-0.12 ± 0.8 (n=357)	-4.64	4.52	p<0.313
42%	0.97 ± 1.0 (n=74)	-1.20	4.45	p<0.0005	-0.08 ± 0.8 (n=67)	-2.68	1.49	p<0.313

Table 2.12
Length Changes in Transverse Sections as a Function of Relative Humidity.

	Radial				Tangential			
Relative Humidity	Ave (%)	Min (%)	Max (%)	Significance (U Test)	Ave (%)	Min (%)	Max (%)	Significance (T Test)
28%	1.39 ± 0.87 (n=143)	-0.46	2.87	p<0.007	1.41 ± 0.57 (n=75)	0.46	2.38	p<0.45
42%	1.11 ± 0.79 (n=90)	0.21	3.43	p<0.007	0.91 ± 0.36 (n=46)	0.49	1.45	p<0.45

Figure 2.11 displays a graphic summary of longitudinal and transverse sections results without the standard deviations. The manner in which bone contracts parallel to lamellae in longitudinal sections is very different from the contraction behavior both perpendicular to lamellae in the same sections and radial and tangential directions in transverse sections. There are other small but statistically significant differences. At 42% rh length changes perpendicular to lamellae were significantly different from radial (pU<0.0030) but not from tangential (pU< 0.13) values of transverse sections; however, at 28% rh they were significantly different from both radial (pU<1.66×10^{-5}) and tangential (pU<3.52×10^{-5}). At 42% rh axial (parallel) values were significantly different from radial and tangential (pU<4.79×10^{-12}). The contractions perpendicular to lamellae and radial to the osteon have almost the same slope, indicating that water

is removed from tissue in the same manner.

2.5.1.4 Cement Line. Changes in length across the cement line (Tables 2.15, 2.17, 2.19, 2.20) were observed both in longitudinal and transverse sections. Samples were examined at 350X and 1200X magnifications. In transverse samples, the cement line contraction was almost same as that of the radial. At 28% rh, contraction across the cement line (1.4%), was almost equal to radial (1.3%) and tangential (1.4%) contractions; as it was true for 42% rh: cement line (0.95%), tangential (0.91%) and radial (1.11%), showing that cement line contraction was mainly due to the contraction within the osteon. In longitudinal sections, at lower rh, there was a difference of approximately 1% between contraction across the cement line (2.09%) and perpendicular to lamellae (0.97%), indicating possibly that in these sections, at this relative humidity, the contracting element across the cement line was independent of that within the osteonal lamellae.

2.5.2 SEM - Back Scattered Electron Imaging

In order to better understand the structural basis for this unusual contraction behavior, we examined polished longitudinal sections in the SEM using two different backscattered electron (BSE) detectors and primary beam energies; one that samples the material very close to the surface (up to about 300nm) and the other one that samples deeper into the structure (up to about a micrometer). Figure 2.12 is a low magnification view image using the shallow outcoming backscattered electron (detector EsB), clearly showing darker and lighter stripes. As BSE images are sensitive to material density (and hence mineral content) [49], this is consistent with parts of the lamella being more mineralized. At higher magnification, first surface sensitive secondary electron imaging (Fig 2.13) and then shallow penetrating BSE imaging of another area were obtained (Fig 2.13). The stripes, clearly seen in both images, apparently correspond to roughly half a lamella. The fact that the stripes are also seen in the secondary image is probably due to local topographic changes, which are expected to occur during

polishing of a material with zones of higher and lower mineral density. Figure 2.14 is an image of another area from which the deeper outcoming signal was detected by the Quadra BSE detector from a depth of about one micrometer. Although the stripes in this image are present but less obvious, it can however be seen that the less contrasting areas, namely those with less mineral, correspond mainly to the part of the lamella in which the collagen fibrils are more or less in the plane of the section.

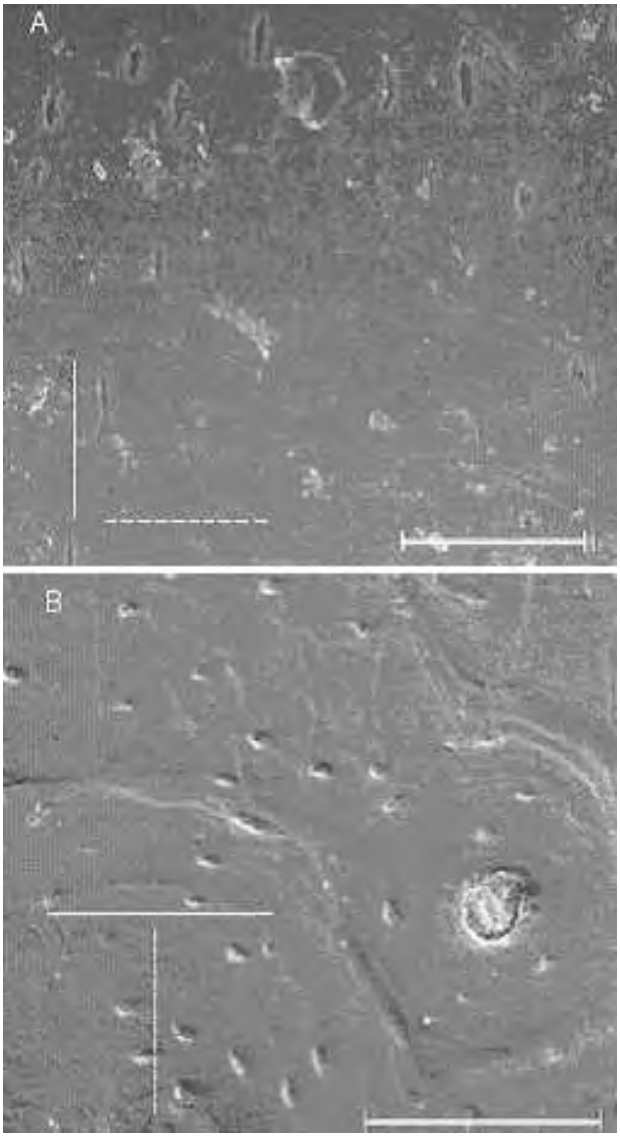

Figure 2.7 A. Longitudinal equine cortical bone section. Solid and dashed lines indicate direction parallel and perpendicular to the lamellae respectively. Lacunae orientation was used as an indicator of lamellar orientation. Note that direction parallel and perpendicular to the lamellae are axial and radial to the third metatarsal bone shaft. Scale bar, 50 micrometers. B. Transverse equine cortical bone section. Solid and dashed lines indicate tangential and radial orientations. Scale bar, 50 micrometers.

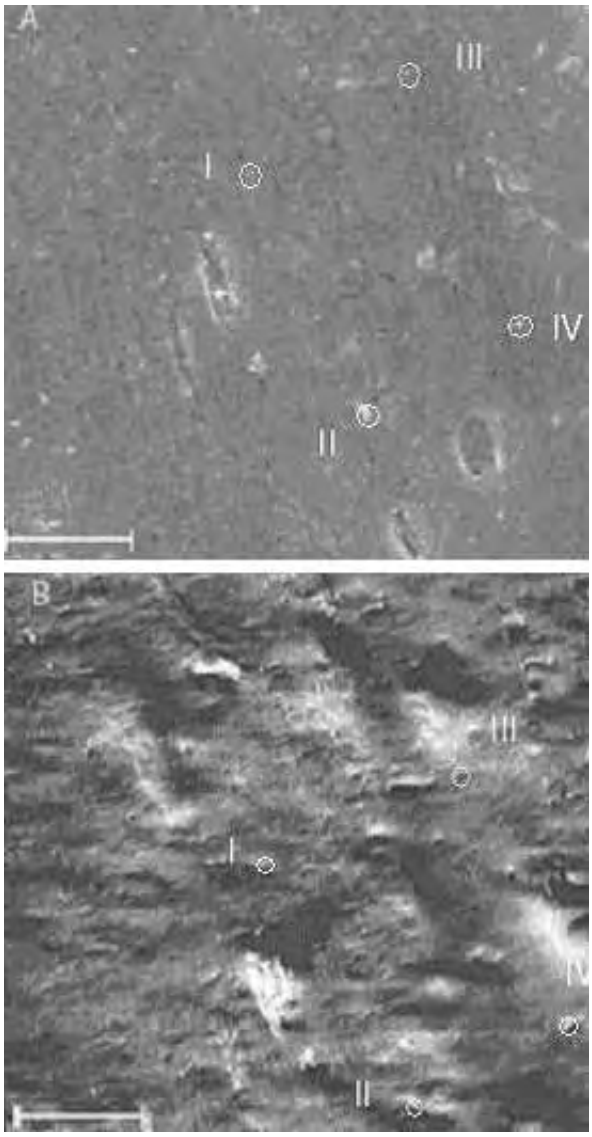

Figure 2.8 A. Longitudinally cut wet equine cortical bone. As the lamellae are curved, segments that intercepted the lamellar front at an angle between 70° to 110° were considered to be perpendicular to the lamellae, and between -20° to 20°, parallel to the lamellae. In this figure, measurements I-III and II-IV were perpendicular to the lamellae, and measurements I-II and III-IV were parallel to the lamellae. Scale bar, 20 micrometers. B. Longitudinally cut dry equine cortical bone. Same site imaged at 28% relative humidity. Scale bar, 20 micrometers.

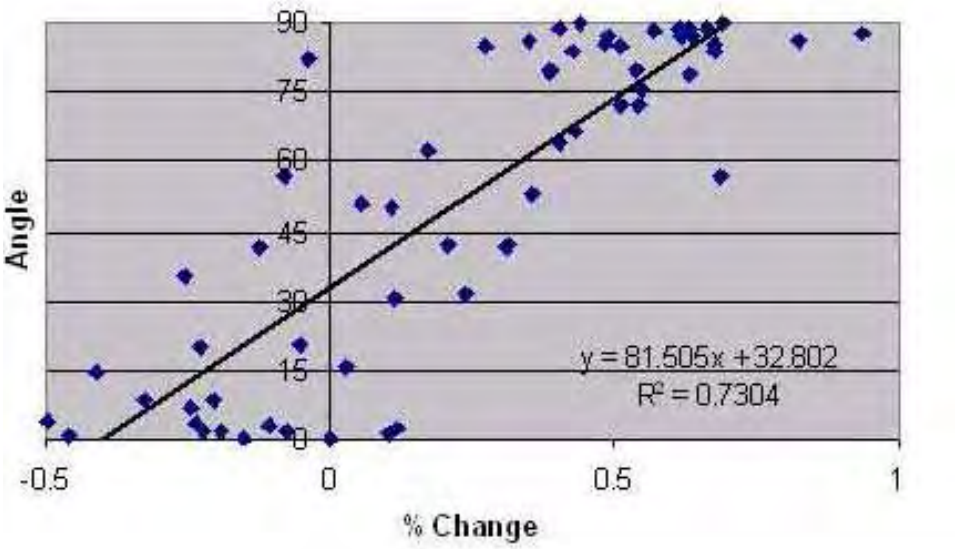

Figure 2.9 Change in length versus angular orientation to lamellar front in sample EQL3b, longitudinal section observed at 28% rh. Explanations are within the text.

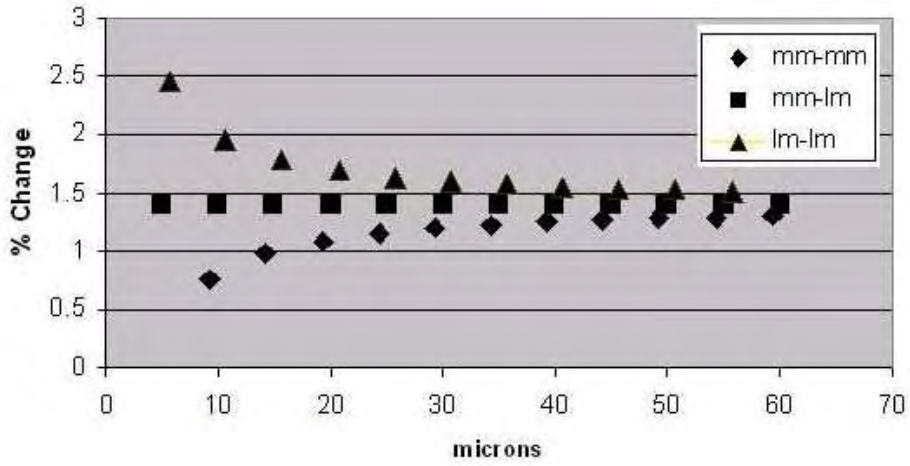

Figure 2.10 Hypothethical distribution of percent length change versus number of more and less mineralized lamellae contained in the measured length. mm-mm, ml-lm and lm-lm indicate respectively that the number of more mineralized lamellae contained in the measured length are greater than, equal to and less than that of less mineralized lamellae.

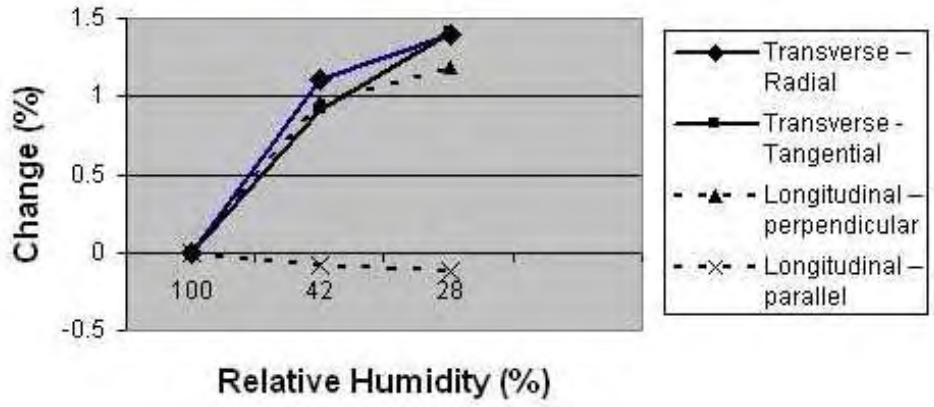

Figure 2.11 Cumulated average length change in longitudinal and transverse sections at 42% and 28% rh. Explanations are within the text.

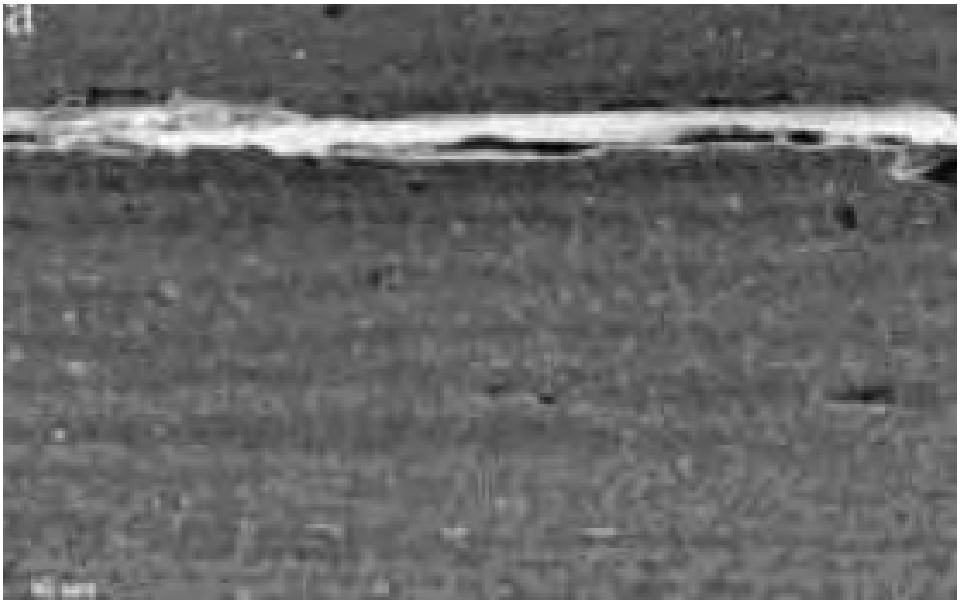

Figure 2.12 A low magnification SEM-BSE image of longitudinally cut equine bone acquired using a shallow penetrating BSE detector. As the BSE images are sensitive to material density and hence mineral content, the darker and lighter stripes are consistent with the parts of the lamellae being more mineralized. Note the highly mineralized cement line in the sample. Scale bar, 10 micrometers.

Table 2.13
Summary of Results - Sample EQL404a.

ROI	Wet Image	Dry Image	Perpendicular to Lamellae	Parallel to Lamellae
Cntrl 1	1	32	0.26 ± 0.48 (n=5)	-1.09 ± 1.18 (n=5)
Cntrl 2	3	33	-0.98 ± 0.28 (n=8)	-0.30 ± 0.44 (n=7)
Cntrl 3	4	34	0.28 ± 0.41 (n=7)	0.53 ± 0.41 (n=8)
Cntrl 5	6	36	-3.19 ± 2.86 (n=5)	-1.30 ± 0.66 (n=2)
Cntrl 6	7	37	-2.62 ± 0.41 (n=6)	-3.89 ± 1.74 (n=6)
	Ave.		**-1.17 ± 1.77 (n=31)**	**-1.05 ± 1.88 (n=28)**
1.9 T.	1	9	0.67 ± 0.29 (n=6)	-0.21 ± 0.43 (n=7)
2.9 T.	1	17	0.63 ± 0.47 (n=6)	-0.29 ± 0.33 (n=7)
1.9 T.	3	11	0.98 ± 0.57 (n=8)	-1.32 ± 0.33 (n=7)
2.9 T.	3	18	0.59 ± 0.24 (n=8)	-1.21 ± 0.39 (n=7)
1.9 T.	4	12	3.60 ± 2.21 (n=7)	0.67 ± 2.04 (n=8)
2.9 T.	4	20	2.60 ± 0.53 (n=7)	0.35 ± 0.77 (n=8)
1.9 T.	6	14	0.68 ± 0.12 (n=6)	-1.77 ± 1.74 (n=6)
2.9 T.	6	22	0.39 ± 0.27 (n=6)	0.29 ± 0.53 (n=6)
1.9 T.	7	15	0.93 ± 0.55 (n=6)	-0.74 ± 1.74 (n=6)
2.9 T.	7	23	0.52 ± 0.39 (n=6)	-0.84 ± 1.26 (n=6)
0.7 T.	1	41	1.88 ± 0.64 (n=6)	-3.07 ± 2.14 (n=7)
0.7 T.	3	44	1.02 ± 0.34 (n=8)	-0.38 ± 0.46 (n=7)
0.7 T.	4	47	4.78 ± 2.09 (n=7)	1.29 ± 1.53 (n=8)
0.7 T.	6	54	0.90 ± 0.21 (n=6)	-1.46 ± 1.61 (n=6)
0.7 T.	7	56	0.68 ± 0.38 (n=4)	-2.75 ± 1.49 (n=4)
0.7 T.	**Ave**		**1.96 ± 1.94 (n=30)**	**-1.05 ± 2.22 (n=32)**
1.9 T.	**Ave**		**1.41 ± 1.54 (n=33)**	**-0.60 ± 1.62 (n=34)**
2.9 T.	**Ave**		**0.97 ± 1.09 (n=41)**	**0.06 ± 0.83 (n=33)**

Table 2.14
Summary of Control Results - Sample EQL404b.

ROI	Wet Image	Rewet Image	Perpendicular to Lamellae	Parallel to Lamellae
2	2	10	0.19 ± 0.20 (n=10)	
2	2	43	-0.58 ± 0.64 (n=10)	
5	5	12	0.08 ± 0.19 (n=11)	
5	5	46	1.88 ± 2.14 (n=9)	
7	6	15	-0.29 ± 0.29 (n=16)	0.56 ± 0.12 (n=12)
	Ave.		**-0.29 ± 0.29 (n=16)**	**0.56 ± 0.12 (n=12)**

Table 2.15
Summary of Results - Sample EQL404b.

ROI	Wet Image	Rewet Image	Perpendicular to Lamellae	Parallel to Lamellae	Cement Line
2	10	23	1.53 ± 1.29 (n=9)	-0.147 ± 0.88 (n=6)	
5	12	26	1.06 ± 1.32 (n=16)	0.11 ± 0.52 (n=7)	2.09 ± 0.86 (n=6)
7	6	29	0.56 ± 0.38 (n=16)	0.52 ± 0.13 (n=12)	
2.9 T.	**Ave**		**0.97 ± 1.09 (n=41)**	**0.06 ± 0.83 (n=33)**	**2.09 ± 0.86 (n=6)**

Table 2.16
Summary of Controls Results - Sample EQT404c.

ROI	Wet Image	Dry Image	Radial	Cement Line
6	6	36	0.10 ± 0.36 (n=6)	0.23 ± 0.67 (n=12)
7	7	35	0.15 ± 0.25 (n=11)	0.08 ± 0.30 (n=24)
8	8	37	-0.07 ± 0.28 (n=13)	0.02 ± 0.28 (n=29)
9	9	38	0.27 ± 0.15 (n=7)	-0.002 ± 0.20 (n=23)
	Ave.		**0.11 ± 0.32 (n=37)**	**0.08 ± 0.44 (n=88)**

Table 2.17
Summary of Results - Sample EQT404c.

ROI	Wet Image	Dry Image	Radial	Tangential	Cement Line
1	1	21	1.09 ± 0.48 (n=10)	0.92 ± 0.34 (n=14)	0.67 ± 0.48 (n=16)
3	3	23	0.91 ± 0.37 (n=9)	0.77 ± 0.28 (n=13)	0.69 ± 0.24 (n=16)
5	5	25	0.80 ± 0.29 (n=23)	0.90 ± 0.23 (n=10)	0.80 ± 0.14 (n=11)
5	5a	25a	1.05 ± 0.32 (n=11)	1.04 ± 0.41 (n=9)	0.76 ± 0.23(n=10)
6	6	14	1.82 ± 1.61 (n=6)	NA	1.59 ± 1.01 (n=12)
7	7	13	0.95 ± 0.66 (n=11)	NA	1.10 ± 0.69 (n=12)
8	8	15	1.29 ± 0.51 (n=13)	NA	1.32 ± 0.56 (n=29)
9	9	16	1.02 ± 0.35 (n=7)	NA	0.65 ± 0.29 (n=23)
2.9 T.	**Ave.**		**1.11 ± 0.79 (n=90)**	**0.91 ± 0.36 (n=46)**	**0.95 ± 0.64 (n=129)**

Table 2.18
Summary of Results - Sample EQL303a.

ROI	Wet Image	Dry Image	Perpendicular to Lamellae	Parallel to Lamellae
Cntrl 1	5	31	-0.08 ± 0.35 (n=13)	0.001 ± 0.42 (n=11)
Cntrl 2	7	48	0.57 ± 0.80 (n=10)	0.20 ± 0.30 (n=11)
	Ave.		**-0.30 ± 0.63 (n=23)**	**0.001 ± 0.42 (n=12)**
1	5	13	0.88 ± 0.46 (n=13)	0.23 ± 0.29 (n=13)
5	15	33	1.44 ± 0.55(n=6)	-0.21 ± 0.67 (n=7)
6	17	35	0.85 ± 0.41 (n=8)	-0.10 ± 0.19 (n=7)
7	19	38	2.07 ± 0.30 (n=15)	0.57 ± 0.37 (n=9)
8	22	41	1.80 ± 1.12 (n=13)	0.60 ± 0.23 (n=13)
10	26	46	1.25 ± 0.91 (n=15)	0.17 ± 0.38 (n=13)
1.9 T.	**Ave.**		**1.47 ± 0.86 (n=72)**	**0.25 ± 0.51 (n=79)**

Table 2.19
Summary of Results - Sample EQT202c.

ROI	Wet Image	Dry Image	Radial	Tangential	Cement Line
3	3	14	1.12 ± 0.27 (n=24)	0.74 ± 0.28 (n=11)	1.03 ± 0.40 (n=11)
4	4	15	1.46 ± 0.65 (n=31)	1.42 ± 0.43 (n=18)	1.26 ± 0.61 (n=8)
5	5	16	0.95 ± 0.40 (n=13)	1.35 ± 0.30 (n=13)	1.17 ± 0.44 (n=13)
6	6	17	0.49 ± 0.95 (n=17)	1.05 ± 0.33 (n=9)	1.33 ± 0.18 (n=11)
7	7	18	2.16 ± 0.71 (n=17)	1.75 ± 0.16 (n=9)	2.04 ± 0.42 (n=11)
8	8	19	1.13 ± 0.69 (n=10)	NA	NA
9	9	20	1.76 ± 0.79 (n=6)	NA	NA
10	11	21	2.10 ± 0.39 (n=25)	2.15 ± 0.23 (n=15)	1.80 ± 0.41 (n=10)
1.9 T.	**Ave**		**1.39 ± 0.87 (n=143)**	**1.41 ± 0.57 (n=75)**	**1.44 ± 0.58 (n=56)**

Table 2.20
Summary of Results - Sample EQL202a.

ROI	Wet Image	Dry Image	Perpendicular to Lamellae	Parallel to Lamellae	Cement Line
Cntr 8			**1.02 ± 0.13 (n=11)**	**0.57 ± 0.35 (n=24)**	**NA**
3	3	14	0.81 ± 0.30 (n=15)	0.07 ± 0.36 (n=14)	NA
4	4	15	1.26 ± 0.65 (n=9)	-0.92 ± 0.73 (n=11)	NA
5	5	16	0.65 ± 0.31 (n=7)	-0.47 ± 0.66 (n=4)	NA
6	6	18	0.98 ± 0.42 (n=19)	-0.81 ± 0.74 (n=9)	1.06 ± 0.49 (n=16)
7	7	20	1.74 ± 0.26 (n=10)	-0.92 ± 0.33 (n=11)	1.29 ± 0.30 (n=11)
8	8	21	1.53 ± 0.42 (n=21)	0.24 ± 0.29 (n=22)	1.30 ± 0.49 (n=15)
9	9	22	1.49 ± 0.42 (n=10)	0.06 ± 0.75 (n=12)	1.12 ± 0.56 (n=10)
10	11	23	NA	-0.20 ± 0.54 (n=11)	2.18 ± 0.79 (n=10)
1.9 T.	**Ave.**		**1.22 ± 0.53 (n=92)**	**-0.25 ± 0.7 (n=97)**	**1.34 ± 0.63 (n=62)**

Table 2.21
Summary of Results - Sample EQL303b.

ROI	Wet Image	Dry Image	Perpendicular to Lamellae	Parallel to Lamellae
Cntrl.8	**Ave.**		**-0.15 ± 0.82 (n=29)**	**-0.56 ± 0.81 (n=15)**
1	1	12	1.11 ± 0.50 (n=27)	0.004 ± 0.62 (n=14)
2	2	13	0.956 ± 0.315 (n=12)	-0.305 ± 0.336 (n=12)
3	3	14	0.636 ± 0.18 (n=25)	0.129 ± 0.36 (n=14)
4	5	15	0.86 ± 0.35 (n=17)	0.047 ± 0.38 (n=17)
5	6	16	0.448 ± 0.25 (n=17)	-0.228 ± 0.29 (n=18)
6	7	21	0.53 ± 0.25 (n=19)	-0.21 ± 0.19 (n=14)
8	9	18	1.43 ± 0.51 (n=15)	-0.50 ± 0.47 (n=19)
9	10	19	NA	-0.09 ± 0.12 (n=17)
10	11	2	1.60 ± 0.51 (n=26)	0.006 ± 0.22 (n=20)
1.9 T.	**Ave.**		**0.99 ± 0.54 (n=162)**	**-0.12 ± 0.39 (n=147)**

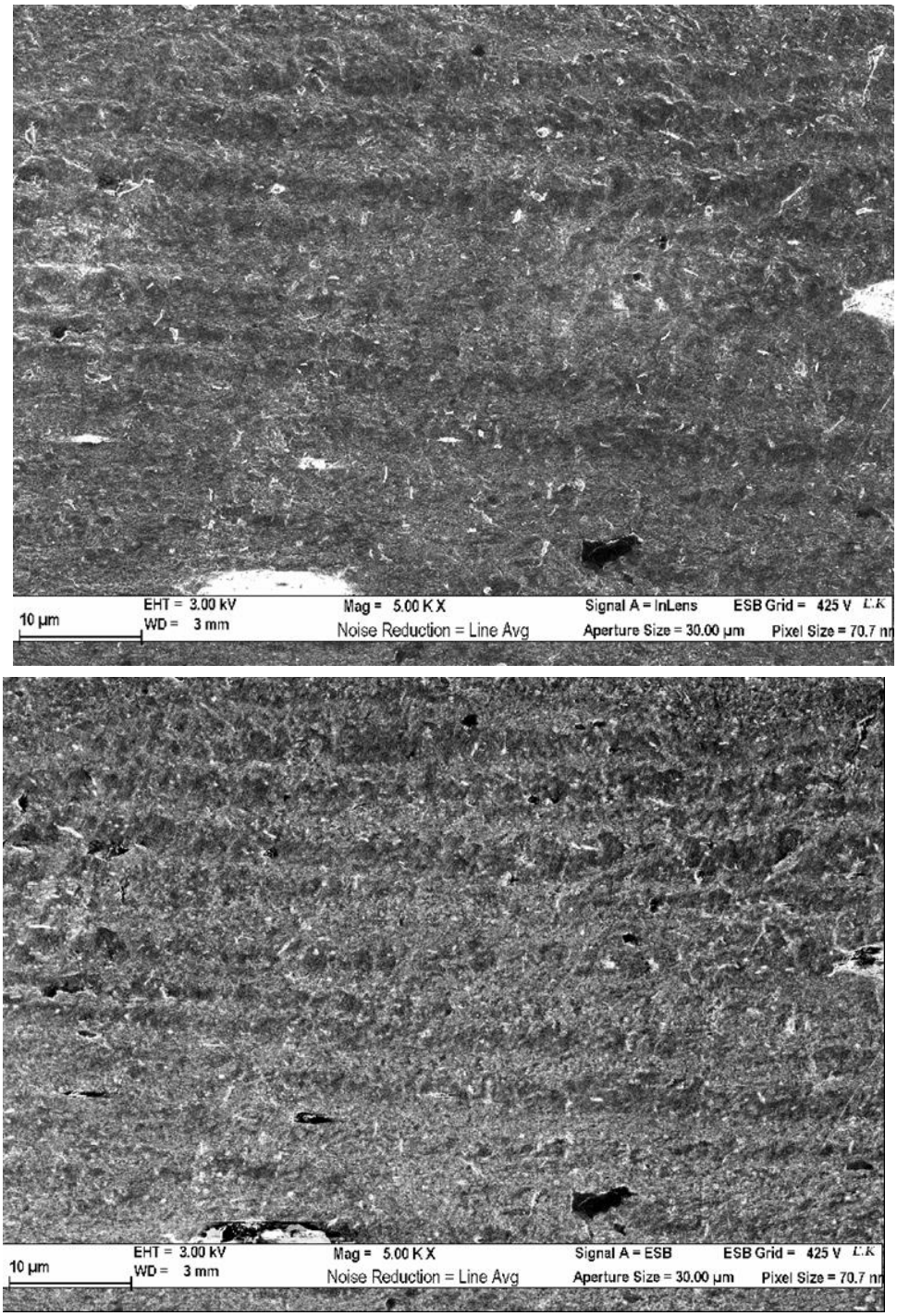

Figure 2.13 A. SEM image of longitudinally cut equine cortical bone. The SEM surface sensitive secondary electron image of a site. Scale bar, 10 micrometers. B. The same site imaged using SEM back scattered electron imaging. The variation in mineralization within the lamellar unit can be clearly observed in both images and they roughly correspond to half a lamella. Scale bar, 10 micrometers.

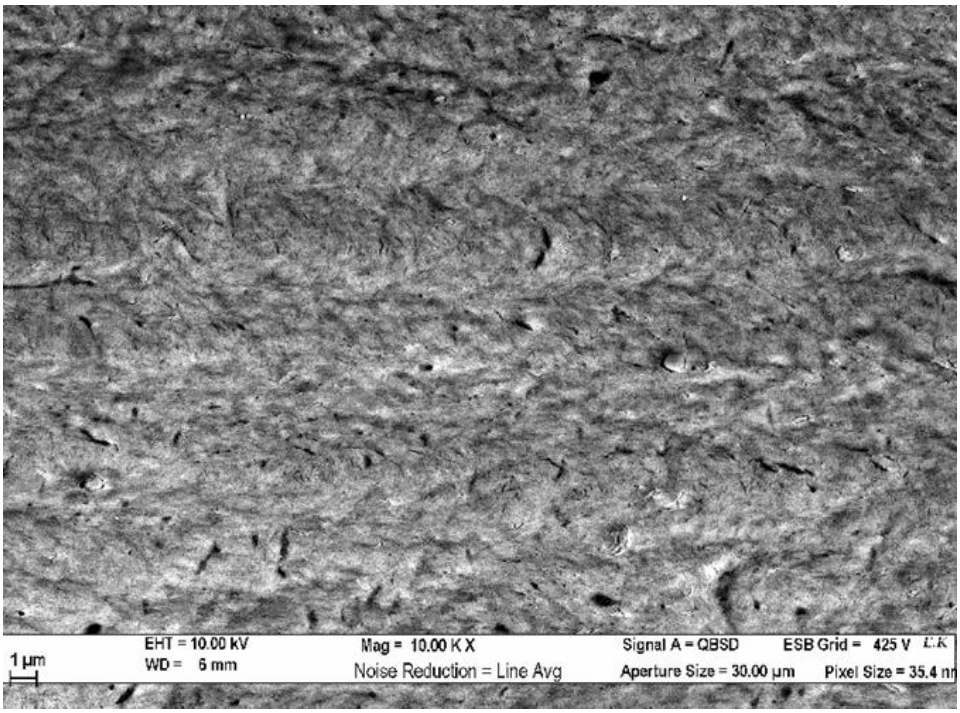

Figure 2.14 SEM-BSE image of a longitudinal section of equine cortical bone acquired using a deeper penetrating BSE detector. The stripes can still be observed in this figure. Scale bar, 1 micrometer.

3. MECHANICAL PROPERTIES of BONE

3.1 Mechanical Studies on Bone

Bone tissue varies in composition to embody different mechanical properties in different locations of the organism. The main concern is that of adaptation of structural design to meet functional requirements in a mechanically viable solution as the organism is under the constraint of microstructural (modelling/remodelling of bone tissue) and biomechanical concerns (attachment of muscles, connective tissues) and mass limitations under space constrained conditions. Basic mechanical testing methods are used to test the material properties of bone, i.e. its elastic and shear moduli, yield stress, ultimate tensile and compressive strength, toughness, etc. As a structure that has both biomechanical and biochemical implications for the organism, providing structural integrity and motility and acting as a source of calcium and phosphorus, bone has been studied extensively since late 1800's making use of various invasive (mechanical testing methods (i.e. compression, tension, and torsion, determination of fiber to volume, biomechanical testing using strain gages and extensometers, photoelastic coating), micrographic techniques (i.e. SEM, ESEM, TEM), X-Ray diffraction, holographic (moire) interferometry, speckle photography and ESPI) and non-invasive methods (X-Ray, DEXA, QCT, photon absorptiometry and ultrasound) [50].

3.1.1 Mechanical Properties of Hierarchically Organized Bone

As a composite material, made of three different phases, bone displays a mixture of the elastic properties of its phases, therefore, its strength may be quite different from the strength of its individual phases. The elastic modulus (E) of water is 2.1 GPa [51], its shear modulus (G) is about 0 GPa [52]; collagen has an E of 1.5 GPa [53], G of 1 GPa [54], and a poisson ratio, ν, of 0.38 [55]; hydroxyapatite has an E of 114 GPa [56], G of 44.5 GPa [56], and a ν of 0.30 [56].

The mechanical properties of bone may vary not only within the organism, but even within the sample [57]. This may be due to several factors, the orientation of the specimen, its hydration state, the strain rate of mechanical testing and the type of load applied [30]. All of the above factors are largely directly related to the collagen scaffold and therefore the mineral crystal orientation in the tissue. The collagen scaffold is organized anisotropically according to the highest strain pattern in bone. The material properties of bone vary according to type of mineralized collagen organization (woven, lamellar and parallel-fibred), the cortices of bones (anterior, posterior, lateral and medial), the loading types (tensile, compressive, torsion, bending, etc.), the loading directions (radial, tangential and longitudinal), the species studied, and the age and sex of organism, etc. Therefore it is crucial to give the specifics of each mechanical test performed and the samples used.

3.1.2 Mechanical Properties According to Type of Collagen Scaffold

The collagen is organized as woven, parallel-fibred, circumferential lamellar, osteonal and fibro-lamellar scaffold. Although the mechanical properties of woven bone are hard to determine, it is known to be very brittle and have a low modulus [30]. Parallel-fibred bone is assumed to have a high elastic modulus as its function is to provide support for the bone. It is hard to test the mechanical properties of parallel-fibred bone for they exist as very small strips within the cortical shell. The fibro-lamellar bone is made of both parallel-fibred bone and woven bone. There is a two-fold difference in stiffness in fibro-lamellar bone between axial and radial directions. Its compressive modulus is greater than its tensile modulus. The fibro-lamellar bone also has a higher compressive elastic modulus and strength and tensile strength than osteonal bone (Table 3.1) [30]. The circumferential lamellar bone is found in reptiles, mammals and birds as primary bone, and has a higher compressive elastic modulus and strength than osteonal bone.

Table 3.1
Comparison of Strength Properties of Osteonal and Fibrolamellar Cortical Bone.

Property	Human Haversian	Bovine Histology Undetermined
Tensile Strength (MPa)	158 ± 8.5	162 ± 14.2
Tensile Yield Stress(MPa)	128 ± 11.2	132 ± 10.6
Ultimate Tensile Strain	0.042 ± 0.0085	0.049 ± 0.0042
Compressive Strength(MPa)	213 ± 10.1	217 ± 26.8
Compressive Yield Stress(MPa)	180 ± 12.5	196 ± 18.5
Ultimate Compressive strain	0.026 ± 0.0056	0.033 ± 0.0056
Shear strength(MPa)	71 ± 7.8	76 ± 6.3
Shear yield stress(MPa)	53 ± 7.7	57 ± 8.4

3.1.3 Mechanical Properties According to Loading Direction and Collagen Fiber Orientation

The mechanical properties of bones are a function of the loading direction (Fig. 3.1). Taking the long shaft of the bones as the reference line, radial direction is from the periosteum to the endosteum (x axis), tangential direction is where the load is tangent to the curvature of the bone (y axis) and axial direction is along the length of the long shaft of the bone (z axis). The variation in the mechanical properties of bone according to three loading directions have been quite thoroughly studied by various researchers [14, 57, 58, 42, 59]. In the radial direction bone has the lowest compressive and tensile elastic modulus, or in a transversely isotropic bone, radial modulus equals the tangential modulus. In the axial direction, bone has the highest compressive or tensile elastic modulus (Table 3.2).

In sections of equine osteonal bone that experience tension and compression, collagen fibers, organized to resist loads in these sections show that the orientation of the fibers is a more important determinant of mechanical behavior than the differences in mineralization [60]. The histology and mechanical properties of bone from the anterior (cranial) and posterior (caudal) sections of horse radii indicate that the caudal

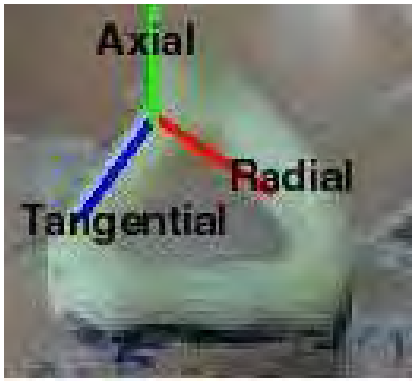

Figure 3.1 The three loading directions for bone. Radial (force applied in the periosteal-endosteal direction), tangential (force applied tangentially to circumference) and axial (along the long axis of bone) directions shown on the ring of minipig tibia.

cortex (compressive) with more transversely oriented fibers is much more remodeled, having greater number of osteons than the cranial (tensile) cortex. As the predominant fiber orientation changes from longitudinal to transverse, a reduction in tensile and an increase in compressive elastic moduli are observed (Table 3.3) [60].

3.1.4 Mechanical Properties According to Type of Loading

Different types of mechanical testing can be performed on bone, e.g. compression, tension, 3-point bending, 4-point bending, torsion, etc. During these tests as discussed above, the different sections of the sample experiences compression, tension or shear forces. The mechanical properties of osteonal bone in compression and tension, listed in Table 3.4, differ according to orientation of the sample as well as loading mode. The anisotropy in strength of bone in compression is not as high as it is in tension [30]. The ultimate compressive strain is greater in the radial direction than in the longitudinal, as the opposite is true in tension, where bone is stronger longitudinally than radially. When the difference in tensile strength is measured along and across grain (parallel vs. perpendicular to lamellae), bone is found to be weaker across (perpendicular) to the lamellae [30, 61].

Table 3.2
Elastic Moduli for Bone.

	Ashman et al.		Reilly and Burstein				
	Canine	Human Haversian	Human Haversian		Bovine Haversian		Bovine Fibrolamellar
	Ultrasound		Mechanical		Mechanical		
			Tension	Compression	Tension	Compression	Tension
E_1 (GPa)	12.8	12.0	12.8 ± 3.0	11.7 ± 1.01	10.4 ± 1.6	10.1 ± 1.8	11 ± 0.17
E_2 (GPa)	15.6	13.4	12.8 ± 3.0	11.7 ± 1.01	10.4 ± 1.6	10.1 ± 1.8	11 ± 0.17
E_3 (GPa)	20.1	20.0	17.7 ± 3.6	18.2 ± 0.85	23.1 ± 3.2	22.3 ± 4.6	26.5 ± 5.4
G_{12} (GPa)	4.7	4.5	-	-	-	-	-
G_{13} (GPa)	5.7	5.6	3.3 ± 0.42		3.6 ± 0.25		5.1 ± 0.39
G_{23} (GPa)	6.7	6.2	3.3 ± 0.42		3.6 ± 0.25		5.1 ± 0.39
v_{12}	0.28	0.38	0.53 ± 0.25	0.63 ± 0.20	0.51 ± 0.24	0.51 ± 0.12	0.63 ± 0.23
v_{13}	0.29	0.22	0.41 ± 0.15	0.38 ± 0.15	0.29 ± 0.08	0.40 ± 0.21	0.41 ± 0.23
v_{23}	0.26	0.24	-	-	-	-	-
v_{21}	0.37	0.42	0.53 ± 0.25	0.63 ± 0.20	0.51 ± 0.24	0.51 ± 0.12	0.63 ± 0.23
v_{31}	0.37	0.42	0.41 ± 0.15	0.38 ± 0.15	0.29 ± 0.08	0.40 ± 0.21	0.41 ± 0.23
v_{32}	0.34	0.35	-	-	-	-	-

3.1.5 Mechanical Properties of Dehydrated Bone

In the organic matrix of the forming bone initially all the voids are filled with water. Ossification starts with crystallization at the voids, occupying the space of water while the collagen constituent remains constant [8]. Water associated with collagen triple helix [62] is excluded by compression of the collagen fibrils. As mineralization removes water, the less hydrated collagen, stiffens as its fibril diameter decreases, with a parallel decrease in the equatorial spacing of collagen molecules [63, 46] thus generating pre-strains in bone [64]. Being a viscoelastic material, the strain-rate dependent mechanical properties of bone are very closely related to its water content. The reduced water content of bone initially increases the stiffness, strength, hardness and relaxation rate, then, after a water loss of 5% by weight, leads to a decrease in toughness and strain at fracture, energy to fracture and anelastic deformation. Age related changes, such as increased collagen cross-linking, may also cause changes in the structure of the scaffolding and thus the amount of water present in the tissue. In dehydrated bone, stiffness has been shown to increase while toughness decreases. Major changes,

Table 3.3
Mechanical Properties of Cortical Bone from Anterior (cranial) and Posterior (caudal) Cortices of Horse's Radius.

Loading Direction	Test Mode	Cortex	Young's Modulus (GPa)	Ultimate Stress (MPa)	Ultimate Strain
Longitudinal	Tension	Cranial(T)	22.1	161	0.028
		Caudal(C)	15.0	105	0.016
	Compression	Cranial(T)	18.6	185	-
		Caudal(C)	15.3	217	-
Transverse	Compression	Cranial(T)	8.2	-	-
		Caudal(C)	10.9	-	-
Note:T, loaded in tension in life; C, loaded in compression in life.					

observed between 4-13% by weight water loss show that while removal of water from the organic phase may lead to a decrease in toughness, removal of water from the mineral leads to a decrease in both toughness and strength of bone. The initial increase and later decrease in strength with dehydration at gradually increasing temperatures is explained as the removal of water associated with the organic and inorganic phases respectively [21, 65].

3.1.6 Mechanical Properties of Osteonal Bone

Osteonal bones are secondary bones, which are therefore younger than the primary bone. The less mineralized bone in the younger Haversian systems has a lower modulus than the older surrounding bone as observed in nanoindentation and Vicker's indentation studies, where the interstitial lamellae have a higher hardness value and recover more slowly than the osteonal lamellae [66, 59]. Katz et al. modeled the Haversian systems as hexagonally packed structures, where the systems and the interstitial lamellae have different elastic moduli [67]. The cement lines, having very low moduli are thought to allow relative movement of the osteons [48, 68]. Frasca et al. have observed higher viscosity and a lower shear modulus and elasticity as the number of

Table 3.4
Strength Properties of Cortical Bone.

	Human		Bovine					
	Haversian		Haversian			Fibrolamellar		
	Axial	Tangential	Axial	Tangential	Radial	Axial	Tangential	Radial
TENSION								
Strength (MPa)	133 ± 16	53 ± 11	150 ± 11	54 ± 6	39 ± 5	167 ± 9	55 ± 9	30 ± 3
Yield Stress (MPa)	114 ± 7	-	141 ± 12	-	-	156 ± 8	-	-
Ultimate Strain	0.031 ± 0.006	0.007 ± 0.0014	0.020 ± 0.005	0.007 ± 0.004	0.007 ± 0.002	0.033 ± 0.0049	0.007 ± 0.0013	0.002 ± 0.001
COMPRESSION								
Strength (MPa)	205 ± 17	131 ± 21	272 ± 3	171 ± 25	190 ± 18	-	-	-
Ultimate Strain	0.019 ± 0.003	0.050 ± 0.011	0.016 ± 0.0015	0.042 ± 0.01	0.072 ± 0.014	-	-	-
SHEAR Strength (MPa)	67 ± 3.5		70 ± 9			64 ± 7		

osteons in the sample increases [69]. Studies on the tension and compression cortices of equine osteonal bone have shown that with the arrangement of collagen fibers as transverse versus longitudinal, osteonal bone provides the extra strength needed locally to the organism, which is provided by the rotated plywood organization of collagen fibers as these fibers also dictate the orientation of minerals as well. The tubular shape of the osteons and their concentration in a unit area provides both toughness and strength needed in the direction of the osteon [60]. Although a fibro-lamellar bone specimen can be 1-1.5 times stronger than osteonal bone made entirely of osteons, the osteonal bone with cement lines, possibly preventing micro-crack propagation, has a higher toughness [30].

3.2 Materials and Methods Used in Studies on Bone Mechanics

The hierarchical organization of collagen in the modelling and remodelling bone, from completely circumferential lamellar bone to partially circumferential lamellar/

partially osteonal to completely osteonal bone may provide an example of how function determines the structure of the organism. After the primary bone is laid down as circumferential lamellar bone in the periosteal and endosteal sections of the bone, it is replaced with osteonal bone as the organism grows over time. In this study, we aimed to understand how the elastic moduli, the Poisson's ratio and the strain distribution in bone differ between the completely osteonal bone and bone that contains both the circumferential and osteonal sections adjacent to one other, by optomechanically testing the proximo-anterior minipig tibial cortical bones radially. In this direction, the load is applied perpendicular to the layers of circumferential lamellar and osteonal bone arranged alternatingly as in the Maxwell model, giving us some insight into the mechanical behavior of circumferential lamellar bone and osteonal bones sections.

3.2.1 Electronic Speckle Pattern Interferometer

Electronic Speckle Pattern Interferometry (ESPI), has been developed by Jones and Wykes to determine the full displacement field on any point of a diffuse reflecting object in 1989 [70]. Combined with the mechanical testing methods, ESPI has, for the first time, technologically enabled researchers in this field to obtain information about the meso-scale dynamic behavior of wet bone samples providing non-contact optical measurements, without application of force or sensor mass, and enabling both qualitative and quantitative point and field analyses. Accurate acquisition of quantitative data of the deformations and graphic display of large number of data points at a higher density leads to a better understanding of the sample under load. Optomechanical testing of bone using ESPI has been used by a number of researchers; and is increasingly becoming a more common research technique used in orthopedics [71, 72, 73, 57] and dentistry [74, 75, 76]. Initially the orthopaedics researchers have used ESPI to determine the bulk properties of bone, the elastic moduli and Poisson's ratios, which need to be investigated using more accurate methods since the mechanical properties of bone vary not only within the tissue, but also within the sample. Stempniewicz et al. [72] have studied the anisotropic mechanical behavior of bone and compared ESPI results with SEM images to determine the contribution of the anisotropic microstructure of

bone to the mechanical behavior of bulk bone. Performing 3-point bending test, they have observed differences not only among the samples, but also among the different surfaces of the same sample.

The optomechanical set-up [74] used in this study consisted of the electronic speckle pattern interferometer, ESPI system (Fig. 3.2)(Q300, Ettemeyer AG, Ulm, Germany) with a 50 mW laser diode ($\lambda = 780$ nm) as the coherent light source, three interferometers, an optical head integrating the three interferometers and a laser source aligned in the orthogonal axis with a single CCD array (768 x 576 detectors) camera detecting the interference speckle images at a rate of 12 frames/sec., the mechanical compression apparatus and a special water chamber to mount the specimen in were used. The set-up was enclosed in an acoustically insulated box mounted on a vibration damping sand bed, placed on a floating optical table. The X and Y interferometers detected in-plane displacements, the Z-interferometer detected out-of-plane displacements. The whole set-up was computer-controlled and measurements were done by rapidly switching between the three speckle interferometers.

3.2.2 Mechanical Compression Apparatus

The mechanical compression apparatus used in this study (Fig. 3.3) was developed by Zaslansky et al. [74] and Shahar et al. [57]. In order to maintain the physiological viscoelastic properties of bone samples, experiments were conducted with the bones fully immersed in water in a specially made water cell, which was mounted on the mechanical compression apparatus orthogonal to the optical axis of the CCD detector array. A custom-built positioning rack with precision positioning rails prevented any horizontal displacements of the water cell.

The system was calibrated using an isotropic material, aluminum (Aluminum 6061 T651) [74] and Ultem [57]), and the mechanical values obtained using the ESPI were compared with those obtained using classical mechanical testing methods. A 3% difference in compression elastic modulus of aluminum was found with the values

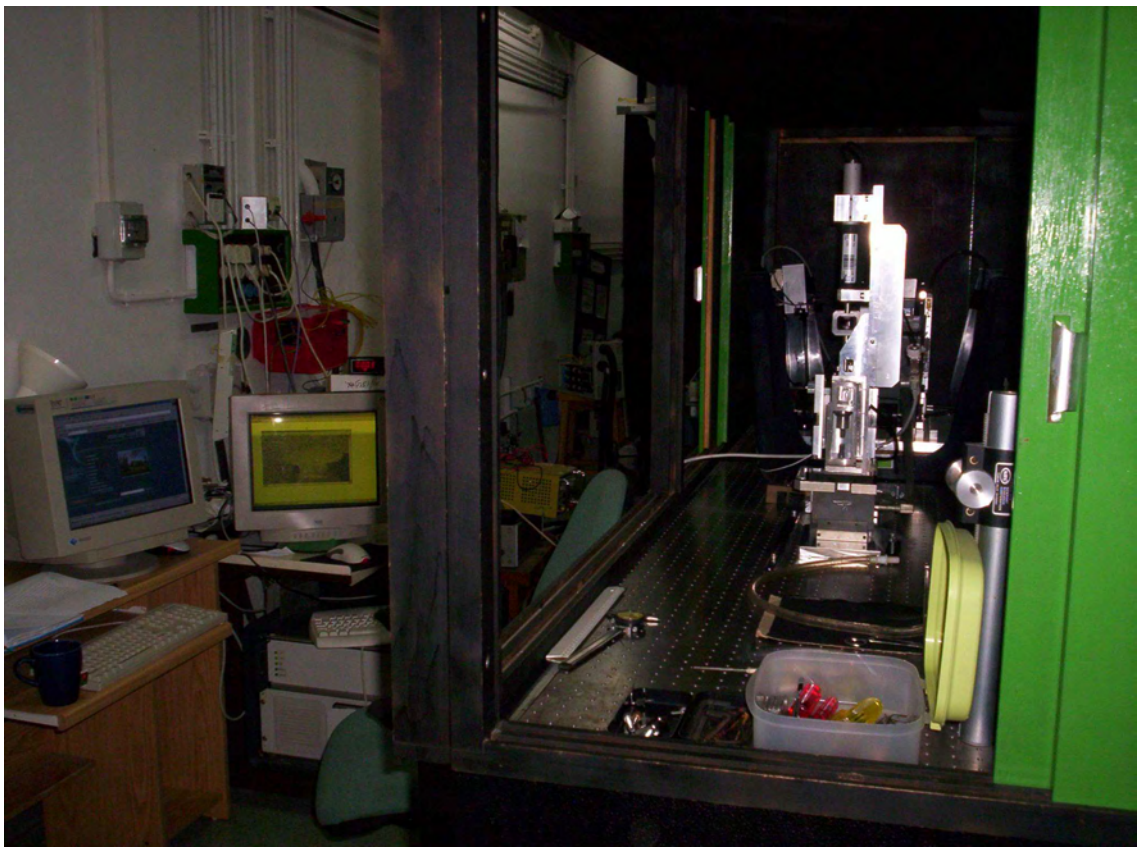

Figure 3.2 ESPI Set-Up. The computer-controlled optomechanical set-up consisting of three interferometers, an optical head integrating the three interferometers and a laser source aligned in the orthogonal axis with a single CCD array camera, the mechanical compression apparatus and a special water chamber to mount the specimen in. The set-up is enclosed in an acoustically insulated box mounted on a vibration damping sand bed, placed on a floating optical table.

Figure 3.3 Mechanical testing apparatus. A stainless steel rod, attached to a sub-micrometer high precision DC motor and controller and coupled with a water-proof load-cell is used as an upper compression anvil, while the lower anvil is stationary. In order to maintain the physiological viscoelastic properties of bone samples, a specially made water cell is mounted on the mechanical compression apparatus orthogonal to the optical axis of the CCD detector array. A custom-built positioning rack with precision positioning rails prevents any horizontal displacements of the water cell.

cited in the literature, compared to a 2% difference in compression elastic modulus of brass found by [73] using ESPI. Calibration of the whole system, involving that of the intricately related mechanical and optical set-up, is complicated due to the fact that the experiments were being conducted with the sample completely immersed in water, which creates time-dependent random variations in the phase of speckles probably due to turbulence and convection currents in the sub-volumes of water and leads to aquatic modulation of phase variations. Calibration of the set-up using aluminum indicated that for an isotropic material, shear strain was at least an order of magnitude smaller than the axial strain. Despite speckle decorrelation, the relatively fast rate of image acquisition (12 frames/sec) enabled reliable detection of small differences in the optical path length.

3.2.3 Materials Used in ESPI Analysis

Goettingen minipig bones were used in this study. Minipigs are miniature swine, first developed at the Hormel Institute at the University of Minnesota in 1949 with the primary cross between guinea hogs from Alabama and wild boars from Catalina lsland. Goettingen miniature swine was developed in 1980 at the University of Goettingen in West Germany from a cross between a Minnesota miniature and a small Vietnamese pig. The specimen were obtained from proximo-anterior minipig tibia of four minipigs. Bones were fresh frozen immediately after acquisition and kept wet and refrigerated in sealed test tubes during the course of this study.

3.2.4 Methods Used in ESPI Analysis

3.2.4.1 Sample Preparation for ESPI Analysis. An approximately 4 mm thick ring, cut from proximal tibia, was coarsely ground with 400, 600, 800 grinding paper and finished with the 5-micrometer diamond polisher. The polished ring was then examined under the microscope to determine microstructure. Two different bone types, namely the circumferential lamellar bone as primary bone and osteonal bone as secondary bone, were observed and their locations were marked. The ring was then further cut into approximately 10 mm^3 cubic samples, which contain completely osteonal or partially osteonal bone sections. Dimensions of each cube were determined and the circumferential lamellar (CLB) and/or osteonal (OB) sections of the samples were photographed. Figs. 3.4 and 3.5 show partially osteonal bone and completely osteonal control bone samples.

3.2.4.2 Data Acquisition Using the ESPI. ESPI experiments were conducted under the supervision of Prof. Steve Weiner, Prof. Ron Shahar, Dr. Paul Zaslansky and Prof. John Currey, who was consulted in the initial phases of the experiments, which were carried out by Dr. Meir Barak and the author of this thesis. In order to eliminate large decorrelating signals and a high level of noise due to capillary flow of

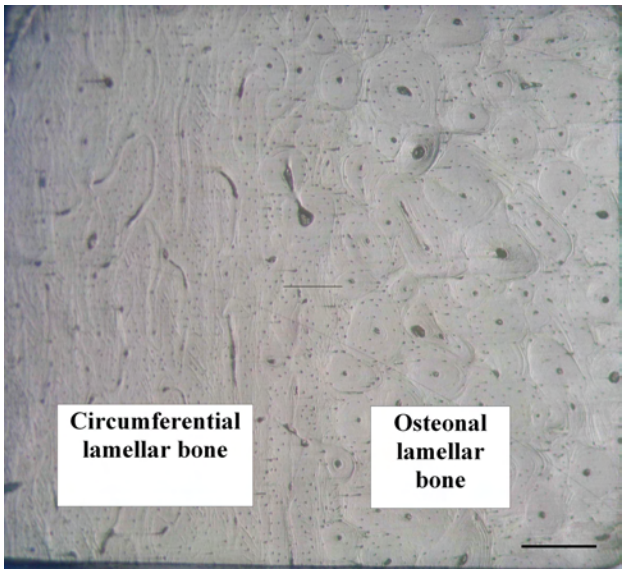

Figure 3.4 Micrograph of a partially osteonal bone sample containing both circumferential lamellar and osteonal bone types. The circumferential lamellar bone is to the left of the image, at the periosteal side of the sample; while the osteonal lamellar bone is to the right of the image, towards the endosteal side. Scale bar, 300 micrometers.

water upon compression, the sample surfaces were coated with a layer of Tipex. To ensure complete and uniform transmission of applied force and to prevent rotation and shear, each sample was mounted with a thin layer of dental composite material (Z-250, 3M ESPE, Saint Paul, Minnesota) placed above and below the specimen, pressed slightly and UV-cured. Photos of each sample with and without Tipex, with a grid to determine pixel size and with the region of interest (ROI) outlined in each bone and the x, y and z speckle images were taken. The experiment consisted of a series of five to ten compression tests with 25 compression increments at a 1.33 micrometer per second (2 um/1.5 sec.) loading rate. While all samples were compressed in the radial (force applied from the periosteum to the endosteum) (PU) and the opposite (force applied from the endosteum to the periosteum) (PD) directions, three samples (O1, B1 and B2) were compressed in radial (PU), tangential (force applied tangentially to circumference) and axial (along the long axis of bone) directions as well. Data was acquired as a matrix of displacements using the methodology determined by Zaslansky et al. [74]. All displacements were measured relative to an arbitrarily chosen reference point, vertical v(i,j) and horizontal u(i,j) displacements were observed within a plane with a displacement gradient along and across the sample, and the w(i,j) displacements observed as out of plane displacements relative to the laser source.

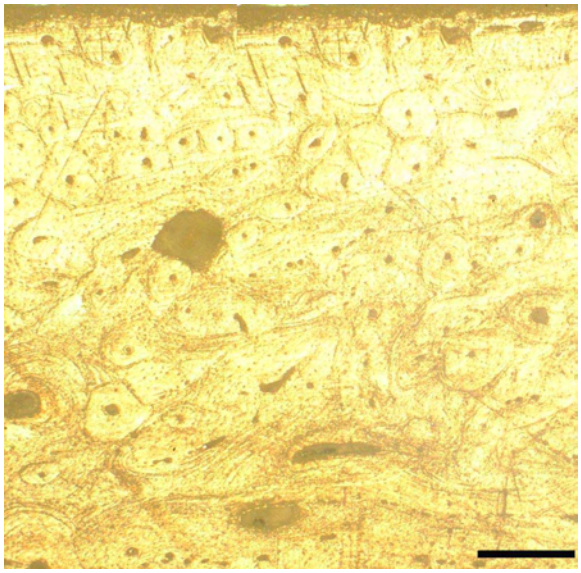

Figure 3.5 Micrograph of a completely osteonal control bone sample. The periosteum is at the top of the image, while the endosteum is towards the bottom of the image. Note the circular hole in the center of the image, a resorption cavity, which will be the site of a new, emerging osteon. Scale bar, 45 micrometers.

3.2.4.3 Data Analysis. Data was analyzed in several consecuitive steps: imaging of total displacements, X and Y linearity of displacements, linearity of gradients and the presence of irregularities in the Y displacement plots. Factors such as the thickness of the circumferential lamellar region and the presence of holes, the presence of internal cavities and holes on the opposite side of the sample may create irregularities in the average displacement plots. Data within the accepted confidence interval were further analyzed to determine strains, Poisson's ratio, elastic moduli, and strain and elastic modulus distributions. According to the Maxwell model, the circumferential lamellar region was expected to displace like a dashpot, steadily yet with a lower slope; while the osteonal bone region was predicted to displace like a spring, more rapidly with a higher slope. The differences in mechanical response of the two parts were calculated from the linearity plots obtained as explained below.

(a) Imaging of Total Displacements

All displacements were measured with reference to a point, vertical v(i,j) and horizontal u(i,j) displacements were observed within a plane with a displacement gradient along and across the sample. Data was processed as a matrix of displacements

using the methodology of Zaslansky et al. [74]. Displacements outlying the average ± standard deviation (for a 95% confidence interval) for each row of data from the reference point were replaced by the average ± standard deviation (for a 95% confidence interval) for that row. The processed displacement matrices of the displacements of the individual 25 compression increments were summed and the resultant matrices were imaged using a Matlab program to show a linear horizontal gradient in the x direction, a linear vertical gradient in the y direction and an out of plane gradient in the z direction.

(b) X and Y Linearity of Displacements

The linearity of the X(i) displacements in the direction perpendicular to the load was determined by averaging the total displacement along the vertical direction (u(i,:)), while the linearity of the Y(j) displacements in the direction parallel to the load, along the horizontal direction v(:,j), by averaging all the values in a single row of pixels. The points that were equally distant to the arbitrary reference point in the Y(i) displacement maps displayed a slope of zero, which was determined by averaging the total Y displacement data along the vertical direction v(i,:) (Fig. 3.6). The averages were plotted as a function of pixel number and the regression value (R^2) for each plot was determined. The mechanical behavior of the completely osteonal control bones and the partially osteonal bones containing both circumferential lamellar and osteonal sections could be differentiated from one another on the basis of their display of linearity. The Y v(i,:) linearity was defined by a regression value (R^2) of ≤ 0.10; while, X u(i,:) and Y v(:,j) linearities were defined by a regression value (R^2) of ≥ 0.95. Data from samples that fulfilled the criteria was further examined for the number of irregularities in the plot, and samples with high numbers of irregularities were rejected.

(c) Strain and Poisson's Ratio Calculations Using Linear Regression

As all distances are measured with reference to a point, vertical v(i,j) and horizontal u(i,j) displacements were observed within a plane with a displacement gradient along and across the sample. Calculating the gradient in the difference of displace-

ments and differentiating the displacements within a known area (x and y pixel size), the full field strain measurement was obtained. Strain-displacement equations were used to calculate the normal and shear strains.

For y normal strain,

$$\epsilon_y = \frac{\partial v}{\partial y} \tag{3.1}$$

,

For x normal strain,

$$\epsilon_x = \frac{\partial u}{\partial x} \tag{3.2}$$

,

and for xy shear strain.

$$\gamma_{xy} = (\frac{\partial u}{\partial y} + \frac{\partial v}{\partial x})/2 \tag{3.3}$$

Poisson ratio, -ϵ_x divided by ϵ_y, was calculated using the strain value for each compression increment.

(d) Elastic Modulus Calculations Using Linear Regression and Stress-Strain Curve

Three different methods were used to calculate the elastic moduli of the samples: using the stress-strain curve, calculating from the mean strain value for each compression and using the linearity plots.

i - A two point gradient analysis was used to calculate the mean strain, giving a single strain value, i.e. the slope for the gradient (displacement) divided by the calculated pizel size in micrometers. The calculated strain and stress for each compression

step were used to calculate the elastic modulus of the samples for that compression step. The strains and elastic moduli calculated for each compression step were then averaged to give the mean for all the compression steps of the samples.

ii - The elastic moduli of the samples were determined from the stress-strain curve, which were obtained from calculations of axial strain for a series of load increments. The mean value for cumulative strain for each compression increment was used to create the stress-strain curve. The cumulative stress and cumulative strain were divided (regressed) to give the compression modulus of elasticity for the bone samples in the direction tested.

iii - As the third method, the Y(j) linearity plot was analyzed to calculate the elastic moduli of circumferential lamellar and osteonal regions of the partially osteonal bone samples. The slopes for the circumferential lamellar and the osteonal regions were calculated by finding the difference in displacement and dividing the difference by the difference in pixel number and further dividing by the pixel size to find the strain. The elastic moduli were then calculated by dividing the stress by the calculated strain.

(e) Determining Strain and Elastic Modulus Distribution Using Linear Regression

The strain distribution across the surface of the bones was calculated using 20x20 pixel regression analysis [77]. A weight of one was assigned to the elements contained within a 20x20 pixel frame, and the frame was moved along (i) and across (j) the matrix elements, finding the linear regression value for the 20x20 pixel plane. Using the strain formulas, dividing by pixel size, the x-, xy- and y- strains were determined. The strain value for each $i_{1:20}$ x $j_{1:20}$ frame was then assigned to pixel (i_1,j_1), which at the end of the analysis resulted in a matrix of strain values, which was correlated with microstructure. In the x-normal strain distribution, the (+) and (-) values indicate that the sample displays strains to the right and left of the reference point respectively. The (+) and (-) values in the y-normal strain distribution indicate that the sample has moved towards or away from the reference point respectively.

3.3 Results

3.3.1 Completely Osteonal Controls

The completely osteonal control bones were compressed radially as PU and PD, tangentially and axially. Although nine osteonal bones were tested, data from only two samples were shown to fulfill the criteria. Microscopic examination of the rejected samples displayed circumferential lamellar regions within the osteonal sections, which we think has affected the results obtained from these bones. As the data for the accepted bones complied with the equine osteonal bones and Ultem results of Shahar et al. [57], they were considered to be sufficient to be used as controls.

3.3.1.1 Imaging of Total Displacements. The X, Y and Z total displacement maps for compression tests conducted in the radial, tangential and axial directions for the completely osteonal control bone, O1, (micrographic image shown in Fig. 3.5) are displayed in Fig. 3.7. In the X and Y total displacement maps, a horizontal and a vertical gradient can be seen. In the Z total displacement map, the gradient is coming out of the plane of this page.

3.3.1.2 X and Y Linearity of Displacements. The regression values for the X, Y(i) and Y(j) averaged total displacements were determined as described in Section 3.2.4.3(b) and listed in Table 3.5. The regression values obtained from tangential and axial compression tests do not fulfill the criteria completely. Although we will be listing and analyzing the results of our control sample and other samples compressed tangentially and axialy, during the course of this analysis we will be concentrating mainly on the analysis of radial and tangential compression test results. The Y(j) linearity plot for the completely osteonal control bone compressed radially is displayed in Fig. 3.8. The plot is linear with minimal number of irregularities.

Table 3.5
Regression Values for the Completely Osteonal Controls

	Regression Values (R^2)		
	X	Y_i	Y_j
O1 Radial	0.9708	0.9709	0.0612
O1 Tangential	0.5576	0.9083	0.3468
O1 Axial	0.2560	0.3086	0.0003
OB13 PU	0.4117	0.9870	0.0458
OB13 PD	0.7630	0.9869	0.1386

3.3.1.3 Strains, Poisson's Ratios and Elastic Moduli. The mechanical properties of the radially, tangentially and axially compressed completely osteonal controls, obtained using the optomechanical testing method, are presented to compare with the values obtained using classical mechanical testing methods in Table 3.6 [78, 79, 30]. Except for those of Crenshaw, values in this table have been acquired from Currey [30]. (Reilly and Burstein, considering bone to be transversely isotropic, have compression tested bovine femur only in directions E_1 and E_3. Ashman et al. have tested canine femur and human femoral osteonal bone by ultrasound.)

3.3.1.4 Strain and Elastic Modulus Distributions. The y-normal, x-normal, xy-shear strain distributions for the complete surface, as well as the y-normal strain profile and elastic modulus distribution profile of the completely osteonal control bone tested radially is shown in Fig. 3.10. In the radially compressed completely osteonal control bone, the y- normal strain varies between $0.5x10^{-4}$ and $3x10^{-4}$, corresponding respectively to the periosteal and endosteal sections of the sample. Stress, calculated by the amount of force applied per compression by the area of the sample, for the completely osteonal control bone tested in various orientations is shown in Fig. 3.9 as stress per compression step. The elastic modulus distribution profile, calculated using the stress and strain distribution for the radially compressed completely osteonal control bone, varies gradually betrween 10 to 6 GPa between the periosteal and endosteal.

Table 3.6
Results of Mechanical Properties of Completely Osteonal Controls

Elastic Moduli	E_1 (GPa)	E_2 (GPa)	E_3 (GPa)
Thesis Results (ESPI)	6.81 ± 0.80	14.35 ± 0.28	25.75 ± 2.18
Crenshaw et.al. (1981)	8.82 ± 1.51	-	-
Reilly and Burstein (1975) bovine osteonal	10.1 ± 1.8	10.1 ± 1.8	22.3 ± 4.6
Reilly and Burstein (1975) human osteonal	11.7 ± 1.01	11.7 ± 1.01	18.2 ± 0.85
Ashman et al. (1984) canine	12.8	15.6	20.1
Ashman et al. (1984) human osteonal	12.0	13.4	20.0
Poisson's Ratios	ν_{12}	ν_{21}	ν_{31}
Thesis Results (ESPI)	0.24	0.332	0.421
Reilly and Burstein bovine osteonal	0.51 ± 0.12	0.51 ± 0.12	0.40 ± 0.21
Ashman et al. (1984) canine	0.28	0.37	0.45

3.3.1.5 Tangential and Axial Compressions. Tangential and axial compression results of completely osteonal bones are given below.

(a) Tangential Compression

The strain and elastic modulus distribution profiles of the tangentially compressed completely osteonal control bone are shown in Fig. 3.11. Note that according to the Maxwell model of viscoelasticity, the radially compressed sample experiences equal amount of stress, while the amount of strain experienced varies in different parts of the sample. On the other hand, while the tangentially compressed sample experiences equal amount strain, the amount of stress experienced varies in the different parts of the sample. Therefore, while, the elastic modulus distribution was calculated by dividing the stress matrix by the strain matrix of the radially compressed sample, for the tangentially compressed sample, the elastic modulus distribution was approximated by taking the reciprocal of the strain matrix of that sample. In the tangentially compressed completely osteonal control bone, the y-strain profile displays and even

distribution, around $0.8x10^{-4}$, without any major variation between the periosteal and endosteal regions of the sample. The stiffness approximations also indicate an even distribution across the surface of the bone as well, fluctuating around 15 GPa.

(b) Axial Compression

The strain distribution and elastic modulus distribution profiles of the axially compressed completely osteonal control bone are shown in Fig. 3.12. In the axially compressed samples, compressed such that both the circumferential lamellar and osteonal sections could be observed, the elastic modulus distribution was approximated by taking the reciprocal of the strain matrix of that sample. In the axially compressed completely osteonal control bone, both the y-strain and elastic modulus distribution profiles do not diplay any variation between the periosteal and endosteal regions.

3.3.2 Partially Osteonal Bones

According to the criteria stated in Section 3.2.4.3, five partially osteonal bones which fulfilled the criteria, namely B4, B5, B8, B14 and B20 were chosen. Table 3.7 lists the percentage of circumferential (CLB) and osteonal (OB) sections the bones contain.

3.3.2.1 Imaging of Total Displacements. The total displacement maps were created and visually inspected for the presence of linear horizontal gradients for x-displacements and vertical gradients for y-displacements. The results for the selected bone samples are shown in Fig. 3.13. In all of the images horizontal and vertical gradients exist for the X and Y total displacement maps.

3.3.2.2 X and Y Linearity of Displacements. The X(i) and Y(j)-linearity regression values of the chosen samples were greater than 0.95. The Y(i)-linearity re-

Table 3.7
Osteonal Bone Content in Radially Compressed Partially Osteonal Bones

Sample	% CLB	% OB
B1 PU	15 (25 pixels)	85 (141 pixels)
B2 PU	28 (48 pixels)	72 (122 pixels)
B3 PU	40 (52 pixels)	60 (78 pixels)
B3 PD	40 (52 pixels)	60 (78 pixels)
B4 PU	40 (52 pixels)	60 (78 pixels)
B4 PD	40 (52 pixels)	60 (78 pixels)
B5 PU	46 (61 pixels)	54 (72 pixels)
B5 PD	46 (61 pixels)	54 (72 pixels)
B6 PU	37 (50 pixels)	63 (87 pixels)
B6 PD	37 (50 pixels)	63 (87 pixels)
B7 PU	40 (62 pixels)	60 (94 pixels)
B7 PD	40 (62 pixels)	60 (94 pixels)
B8 PU	28 (42 pixels)	72 (109 pixels)
B8 PD	28 (42 pixels)	72 (109 pixels)
B12 PU	9 (13 pixels)	91 (117 pixels)
B12 PD	9 (13 pixels)	91 (117 pixels)
B14 PU	26 (29 pixels)	74 (84 pixels)
B14 PD	26 (29 pixels)	74 (84 pixels)
B20 PU	11(12 pixels)	89 (113 pixels)
B20 PD	11(12 pixels)	89 (113 pixels)

gression values, which detect sloping displacement maps, were less than 0.10. The visual inspection of the gradient in Y-total displacement maps, the X(i)-linearity, Y(j)-linearity and Y(i)-linearity regression values obtained from all the radially compressed bones are listed in Table 3.8. The Y(j)-linearity plots for the chosen bones are given in Figure 3.14. In the final step, the linearity plots for these samples were examined and those that did not contain any irregularities and peaks were chosen, i.e. data from sample B20 PU was not included as its linearity plot contained many peaks and irregularities. Data from tests B4 PU, B5 PD, B8 PU, B8 PD, B14 PD and B20 PD were chosen for further analysis to determine the differences in the elastic moduli of the circumferential and osteonal sections for bones.

3.3.2.3 Strains, Poisson's Ratios and Elastic Moduli. The mechanical properties of partially osteonal bones, listed in Table 3.9, have been obtained by the two-point linear regression analysis described in Section 3.2.4.3(d)i, and by regression of cumulative stress against cumulative strain as described in Section 3.2.4.3(d)ii.

The partially osteonal bones displayed differing displacement slopes within the plot, where the slope was slightly less in the circumferential lamellar section (at the periosteum) than in the osteonal section. The elastic moduli for the circumferential lamellar and osteonal sections, calculated as described in the Section 3.2.4.3(d)iii, are listed in Table 3.10, where E stands for elastic modulus. The elastic moduli for the circumferential lamellar bone and osteonal bone were found to be 9.43 ± 2.06 and 6.13 ± 0.90 respectively. The elastic moduli calculated from stress and y-strain for the circumferential lamellar and osteonal lamellar sections of the partially osteonal bones have been plotted against the strain values in Fig. 3.15, showing a distinct separation between the two types of bone, where the circumferential lamellar bone is stiffer than the osteonal bone.

3.3.2.4 Strain and Elastic Modulus Distributions. The data for the partially osteonal bones was analyzed for strain and elastic modulus distribution using linear

Table 3.8
Regression Values for Radially Compressed Partially Osteonal Bones

Sample	Y Total Displacement	X(i)-Linearity	Y(i)-Linearity	Y(j)-Linearity
B1 PU	OK	0.5661	0.9585	0.7193
B2 PU	OK	0.2580	0.9474	0.2446
B3 PU	-	-	0.7471	-
B3 PD	-	0.9913	0.9856	0.3966
B4 PU	OK	0.9860	0.9641	0.0584
B4 PD	-	0.9778	0.9918	0.6054
B5 PU	-	0.9845	0.8469	0.9558
B5 PD	OK	0.9912	0.9894	0.1035
B6 PU	-	0.9830	0.963	0.0657
B6 PD	-	0.9896	0.9797	0.2859
B7 PU	-	-	0.9338	-
B7 PD	-	-	0.9432	-
B8 PU	OK	0.9760	0.9905	0.0800
B8 PD	OK	0.9816	0.9758	0.0223
B12 PU	-	-	0.9171	-
B12 PD	-	-	0.994	-
B14 PU	-	0.9890	0.9211	0.9717
B14 PD	OK	0.9893	0.9946	0.0515
B20 PU	OK	0.9696	0.9843	0.0567
B20 PD	OK	0.9925	0.9786	0.1083

Table 3.9
Results of Mechanical Properties of Radially Compressed Partially Osteonal Bones

Sample	R^2	Elastic Modulus (GPa)		Poisson's Ratio
		Stress-Strain Curve	Two-Point Linear Regression	
B1 PU	0.996	10.3 ± 0.2	10.4 ± 0.2	0.17
B2 PU	0.999	9.8 ± 0.1	9.9 ± 0.1	0.13
B3 PU	0.999	7.2 ± 0.4	7.7 ± 0.1	0.20
B3 PD	0.999	11.2 ± 1.1	11.2 ± 2.4	0.44
B4 PU	0.999	6.4 ± 3.1	7.6 ± 0.2	0.20
B4 PD	0.999	7.6 ± 1.3	8.7 ± 0.2	0.27
B5 PU	0.999	15.8± 3.8	13.7 ± 0.2	0.40
B5 PD	0.999	7.6 ± 1.3	8.1 ± 0.3	0.36
B6 PU	0.999	11.5 ± 5.7	9.2 ± 0.4	0.33
B6 PD	0.990	9.2 ± 2.2	10.3 ± 0.5	0.32
B7 PU	0.999	8.6 ± 1.3	8.7 ± 0.2	0.34
B7 PD	0.999	6.6 ± 0.9	6.6 ± 0.2	0.30
B8 PU	0.996	8.0 ± 1.2	8.1 ± 0.3	0.24
B8 PD	0.999	8.4 ± 0.9	8.0 ± 0.2	0.17
B12 PU	0.999	11.4± 0.5	11.7 ± 0.6	0.41
B12 PD	0.999	7.2± 0.4	7.5 ± 0.4	0.20
B14 PU	0.999	10.0± 1.2	10.3 ± 0.5	0.56
B14 PD	0.999	6.4 ± 0.9	6.4 ± 0.2	0.38
B20 PU	0.997	11.2± 1.8	12.5 ± 0.6	0.34
B20 PD	0.999	12.4± 0.5	11.9 ± 0.3	0.49

Table 3.10
Results of Mechanical Properties of Circumferential Lamellar and Osteonal Bones

		Set 1	**Set 2**	**Set 3**	**Set 4**	**Set 5**	**Average ± Sd**
B4 PU	ϵ_{CLB}	2.1E-3	2.2E-3	2.2E-3	1.8E-3	1.9E-3	2.4E-3 ± 1.8E-4
	ϵ_{OB}	3.6E-3	3.9E-3	3.5E-3	4.1E-3	4.3E-3	3.9E-3 ± 3.1E-4
	σ	18.6	18.6	18.7	18.6	18.7	18.6 ± 4.9E-2
	E_{CLB}	8.9	8.9	8.6	10.2	9.9	**9.2 ± 0.8**
	E_{OB}	5.2	4.7	5.3	4.5	4.4	**4.8 ± 0.4**
B5 PD	ϵ_{CLB}	1.8E-3	1.6E-3	1.7E-3	1.7E-3	1.9E-3	1.7E-3 ± 1.2E-4
	ϵ_{OB}	2.5E-3	3.0E-3	3.2E-3	2.9E-3	2.8E-3	2.9E-3 ± 2.6E-4
	σ	17.8	18.0	18.9	18.3	18.4	18.1 ± 2.2E-01
	E_{CLB}	9.8	11.1	10.8	10.9	9.6	**10.4 ± 0.7**
	E_{OB}	7.2	6.1	5.6	6.3	6.5	**6.3 ± 0.6**
B8 PU	ϵ_{CLB}	2.3E-3	2.0E-3	2.1E-3	2.2E-3	2.1E-3	2.1E-3 ± 9.7E-05
	ϵ_{OB}	3.1E-3	3.1E-3	3.4E-3	3.2E-3	3.2E-3	3.2E-3 ± 1.2E-4
	σ	20.5	20.5	20.4	20.4	20.4	20.4 ± 0.1
	E_{CLB}	8.9	10.0	9.7	9.5	9.7	**9.6 ± 0.4**
	E_{OB}	6.7	6.6	6	6.4	6.3	**6.4 ± 0.3**
B8 PD	ϵ_{CLB}	2.8E-3	2.6E-3	2.5E-3	2.4E-3	2.5E-3	2.6E-3 ± 1.5E-4
	ϵ_{OB}	3.1E-3	3.2E-3	3.3E-3	3.1E-3	2.9E-3	3.1E-3 ± 1.6E-4
	σ	20.7	20.7	20.7	20.7	20.8	20.7 ± 0.1
	E_{CLB}	7.4	7.9	8.3	8.6	8.3	**8.1 ± 0.5**
	E_{OB}	6.6	6.5	6.3	6.6	7.3	**6.7 ± 0.4**
B14 PD	ϵ_{CLB}	2.8E-3	2.9E-3	3.2E-3	2.8E-3	3.2E-3	3.0E-3 ± 2.0E-4
	ϵ_{OB}	3.8E-3	3.5E-3	3.6E-3	3.7E-3	4.4E-3	3.8E-3 ± 3.6E-4
	σ	20.4	20.5	20.5	20.4	20.4	20.4 ± 4.8E-2
	E_{CLB}	7.2	7.0	6.4	7.2	6.3	**6.8 ± 0.5**
	E_{OB}	5.4	5.8	5.6	5.6	4.6	**5.4 ± 0.5**
B20 PD	ϵ_{CLB}	2.0E-3	1.9E-3	1.9E-3	1.3E-3	1.6E-3	1.8E-3 ± 2.9E-4
	ϵ_{OB}	2.9E-3	2.7E-3	2.9E-3	3.3E-3	3.2E-3	3.0E-3 ± 2.2E-4
	σ	21.6	21.7	21.6	21.6	21.7	21.6 ± 5.20E-2
	E_{CLB}	10.6	11.1	11.1	16.2	13.3	**12.5 ± 2.3**
	E_{OB}	7.4	8.0	7.3	6.6	6.8	**7.2 ± 0.5**
CLB	**ave E**	(GPa)					**9.4 ± 2.1**
OB	**ave E**	(GPa)					**6.1 ± 0.9**

regression analysis as described in Section 3.2.4.3(e). X-, xy- and y-strains were calculated using the strain formulae. The strain and elastic distributions of samples B4 PU, B5 PD, B8 PU, B8 PD, B14 PD and B20 PD are given in Appendix A. Fig. 3.16 shows the x-, xy- and y-strain distribution across the whole surface, the y-strain distribution profile, the microscopic image and the [3x3] median filtered elastic modulus distribution profile. X-normal strain distribution varies between -2x10^{-5} and 8x10^{-5}, xy-shear strain distribution varies between -1x10^{-4} and 2.5x10^{-4}, while the y-normal strain distribution varies between 0.5x10^{-4} and 2.5x10^{-4} in the osteonal section and between 0.5x10^{-4} and 1.5x10^{-4} in the circumferential lamellar section of the sample. The elastic modulus varies between 5-10 GPa in the osteonal section and 8-14 GPa in the circumferential lamellar section of the bone.

In addition to one of the completely osteonal control bone samples, two partially osteonal bone samples, B1 and B2 were tested in radial, tangential and axial directions. The total displacement maps for the radially, tangentially and axially compressed partially osteonal bone, B1, are given in Fig. 3.17. The mechanical properties for these bones obtained using the ESPI have been compared with those of other researchers obtained using classical mechanical testing methods in Table 3.11. The strain and elastic modulus distributions for the radially compressed partially osteonal bones, B1 and B2 are displayed in Figs. 3.18 and 3.19. In the radially compressed partially osteonal bone, B1, the x-normal strain distribution variation is greater between the circumferential lamellar and osteonal sections (ranging from 1.4x10^{-4} to -2x10^{-5}), than the xy-shear strain distribution (ranging from 0.6x10^{-4} to 2.25x10^{-4}). The y-normal strain distribution displays values ranging from 0.5x10^{-4} to 1.5x10^{-4} between the circumferential lamellar and the osteonal section of the sample, corresponding to moduli of 40 GPa and 8 GPa for the circumferential lamellar and osteonal sections of the bone. In the radially compressed partially osteonal bone, B2, the x-normal strain distribution variation between the circumferential lamellar and osteonal sections is more pronounced than B1 (ranging from -2 to 4x10^{-5}), ranging from -10x10^{-5} to 8x10^{-5}. In the xy-shear strain distribution the variation between circumferential lamellar and the osteonal sections is from 0.5x10^{-4} to 4x10^{-4}. The y-normal strain distribution displays values ranging from 0.5x10^{-4} to 1.5x10^{-4} between the circumferential lamellar and osteonal sections

Table 3.11
Results of Mechanical Properties of Partially Osteonal Bones Tested in Three Orthogonal Directions

	B1			**B2**		
Elastic Moduli	**E_1 (GPa)**	**E_2(GPa)**	**E_3(GPa)**	**E_1(GPa)**	**E_2(GPa)**	**E_3(GPa)**
Thesis Results (ESPI)	10.35 ± 0.25	15.60 ± 0.38	20.90 ± 1.61	9.84 ± 0.04	19.75 ± 0.7	44.19 ± 5.14
Crenshaw (1981)	8.82 ± 1.51	-	-	8.82 ± 1.51	-	-
Reilly and Burstein (1975) bovine osteonal	10.1 ± 1.8	10.1 ± 1.8	22.3 ± 4.6	10.10 ± 1.8	10.10 ± 1.8	22.30 ± 4.6
Reilly and Burstein (1975) human osteonal	11.7 ± 1.01	11.7 ± 1.01	18.2 ± 0.85	11.7 ± 1.01	11.7 ± 1.01	18.2 ± 0.85
Ashman et al. (1984) canine	12.8	15.6	20.1	12.8	15.6	20.1
Ashman et al. (1984) human osteonal	12.0	13.4	20.0	12.0	13.4	20.0
Poisson's Ratios	ν_{12}	ν_{21}	ν_{31}	ν_{12}	ν_{21}	ν_{31}
Thesis Results (ESPI)	0.174	0.167	0.341	0.139	0.38	0.562
Reilly and Burstein (1975)	0.51 ± 0.12	0.51 ± 0.12	0.40 ± 0.21	0.51 ± 0.12	0.51 ± 0.12	0.40 ± 0.21
Ashman et al. (1984)	0.28	0.37	0.45	0.28	0.37	0.45

of the sample, corresponding to moduli of 20-25 GPa and 5 GPa for the circumferential lamellar and osteonal sections of the bone respectively.

3.3.2.5 Tangential and Axial Compressions. Tangential and axial compression results of partially osteonal bones are given below.

(a) Tangential Compression

The profile for y-strain and elastic modulus distributions for the tangentially compressed partially osteonal bones, B1 and B2 are displayed in Figs. 3.20 and 3.21. In the tangentially compressed partially osteonal bone, B1, the y-normal strain distribution displays values ranging from $0.5\text{x}10^{-4}$ to $0.6\text{x}10^{-4}$ between the circumferential

lamellar and the osteonal sections of the sample, corresponding to moduli of 22 GPa and 16 GPa for the two respective sections of the bone. In the tangentially compressed partially osteonal bone, B2, the y-normal strain distribution displays values ranging from $0.6\text{x}10^{-4}$ to $0.85\text{x}10^{-4}$ between the circumferential lamellar and the osteonal sections of the sample, corresponding to moduli of 16 GPa and 12 GPa for the two respective sections of the bone.

(b) Axial Compression

The profile for y-strain and elastic modulus distributions for the axially compressed partially osteonal bones, B1 and B2 are displayed in Figs. 3.22 and 3.23. In the axially compressed partially osteonal bone, B1, the y-normal strain distribution displays values ranging from $0.5\text{x}10^{-4}$ to $0.6\text{x}10^{-4}$ between the circumferential lamellar and the osteonal sections of the sample, corresponding to moduli of 18 GPa and 15 GPa for the two respective sections of the bone. In the axially compressed partially osteonal bone, B2, the y-normal strain distribution displays values ranging from $0.2\text{x}10^{-4}$ to $0.3\text{x}10^{-4}$ between the circumferential lamellar and the osteonal section of the sample, corresponding to moduli of 45 GPa and 30 GPa for the two respective sections of the bone.

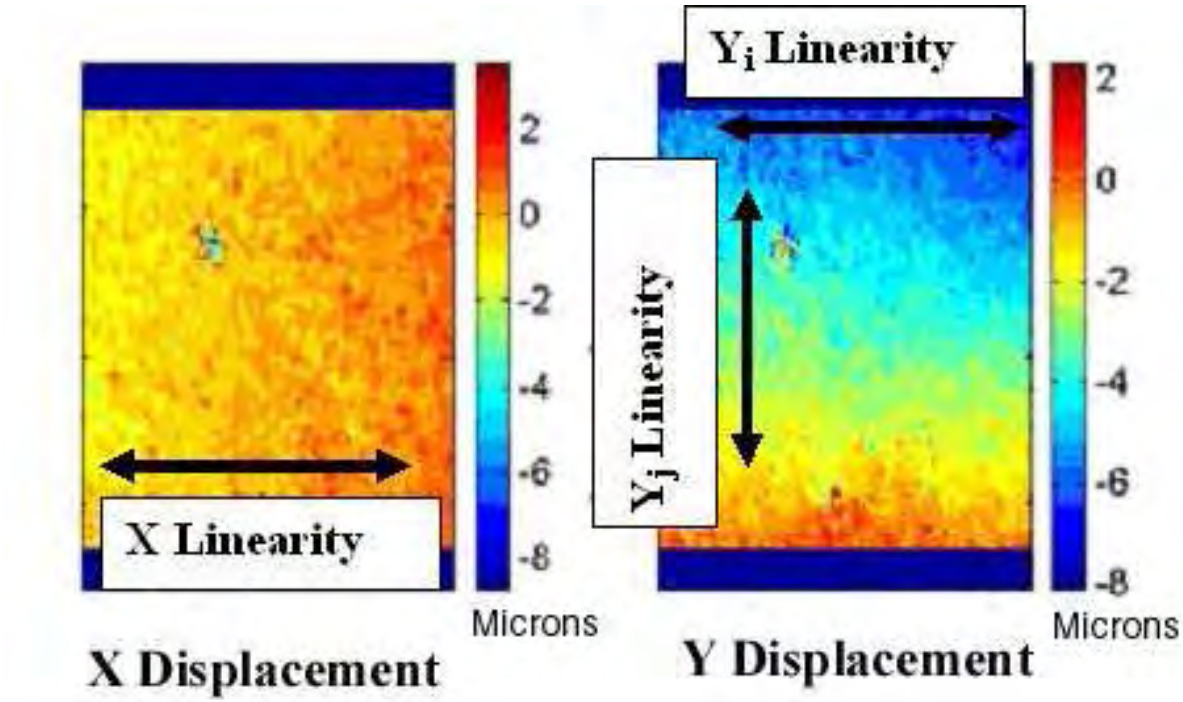

Figure 3.6 The directions for X and Y displacement gradients and linearity of the displacements shown on X and Y total displacement maps showing the bone surface. The load is applied vertically as shown in the image; while the matrix is transformed to obtain this image. X(i) and Y(i) linearity are determined by averaging all the values in a single row of pixels parallel to the load, while Y(j) linearity is determined by averaging perpendicular to the load. Colorbars indicate displacement in micrometers. The unit of length for the abscissa and ordinate is pixel number, where the pixel size is approximately 12 micrometers.

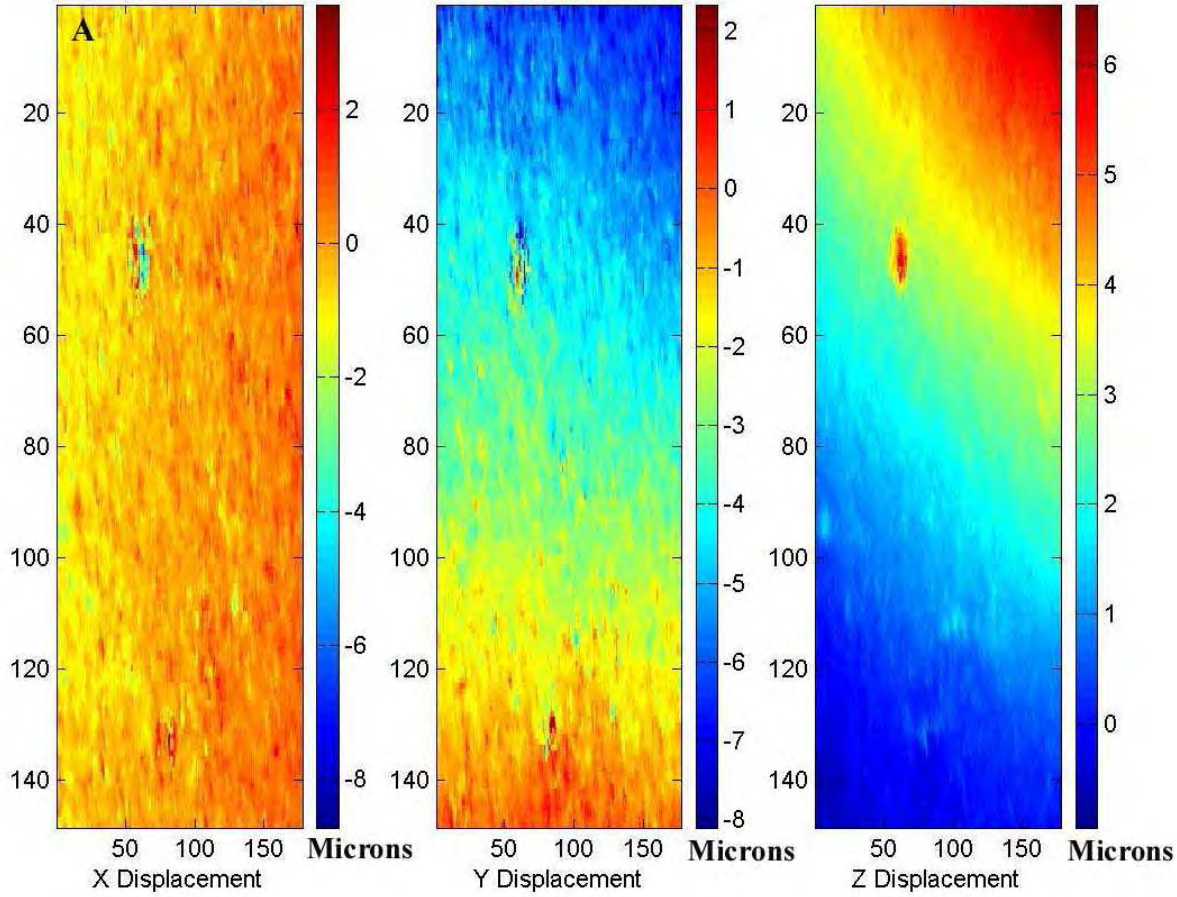

Figure 3.7 The total displacement maps for the radially, tangentially and axially compressed completely osteonal control bone. Images show X, Y and Z total displacements in the radial compression test (A), followed by the tangential (B) and axial (C) compression tests. The load is applied vertically. Colorbars indicate displacement in micrometers. The unit of length for the abscissa and ordinate is pixel number, where the pixel size is approximately 12 micrometers.

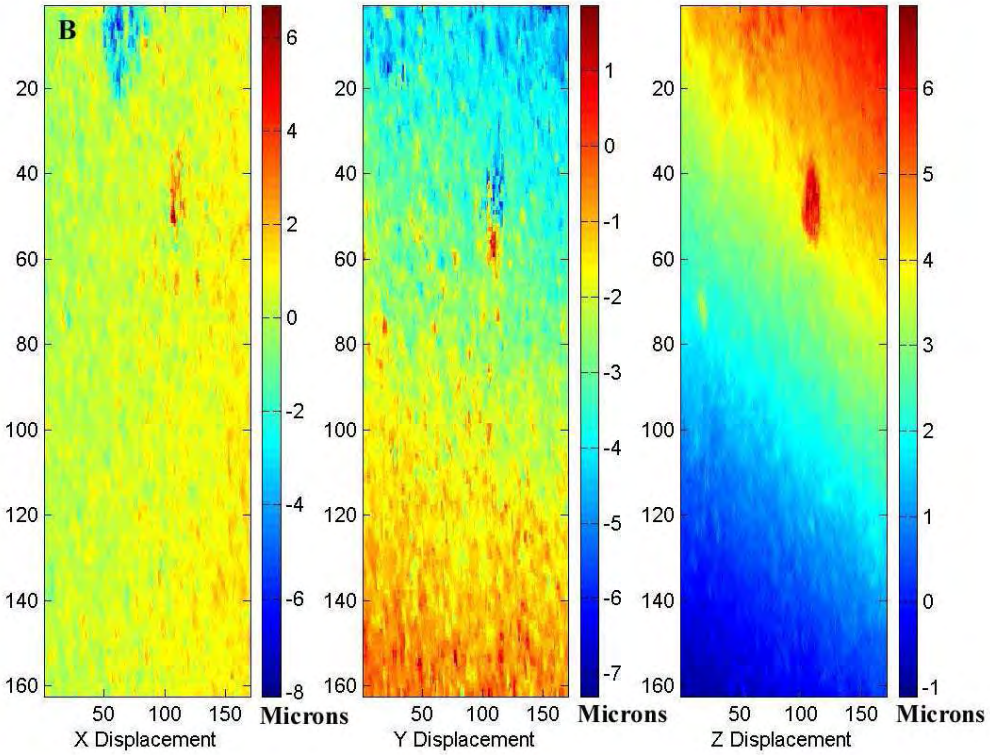
B
X Displacement
Y Displacement
Z Displacement
Microns
Microns
Microns

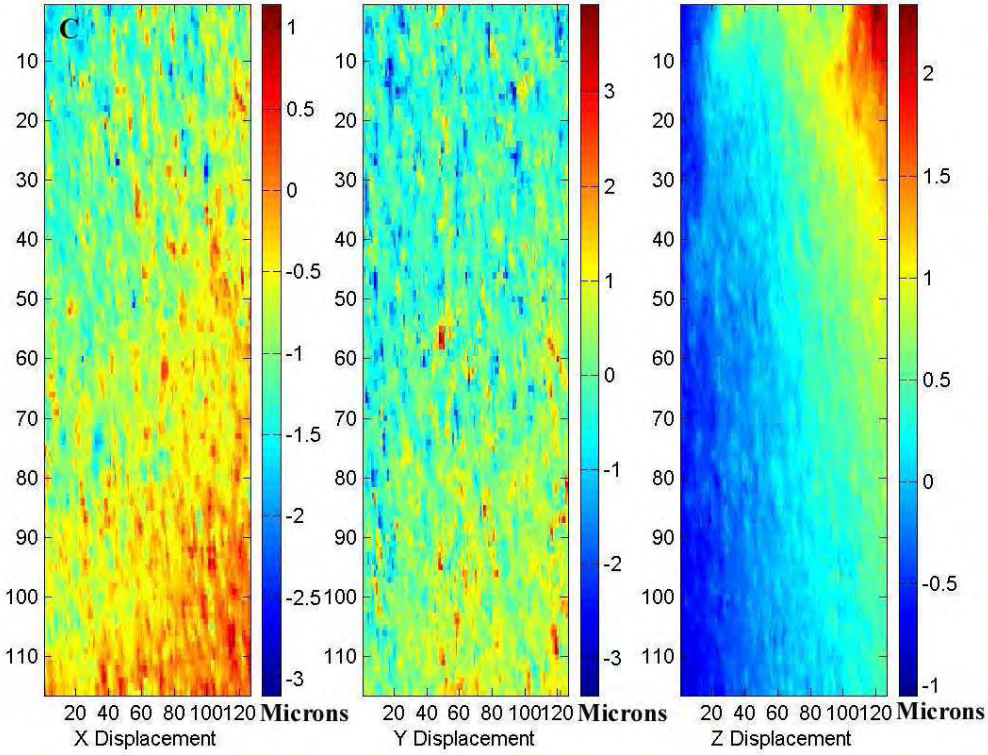
C
X Displacement
Y Displacement
Z Displacement
Microns
Microns
Microns

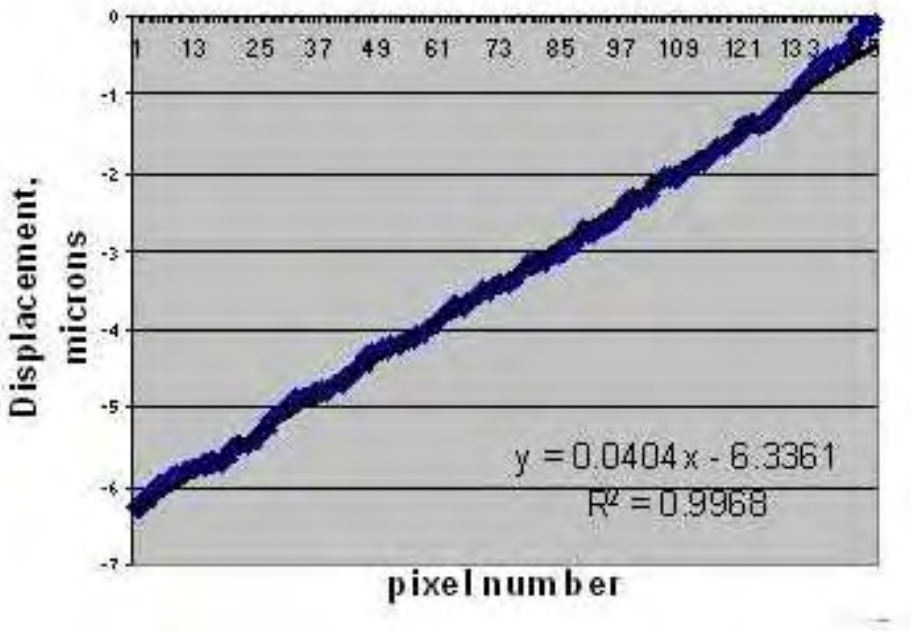

Figure 3.8 Y(j) Linearity plot for completely osteonal control bone compressed radially. Displacements in micrometers per pixel number are regressed, with the regression value and equation given in the figure.

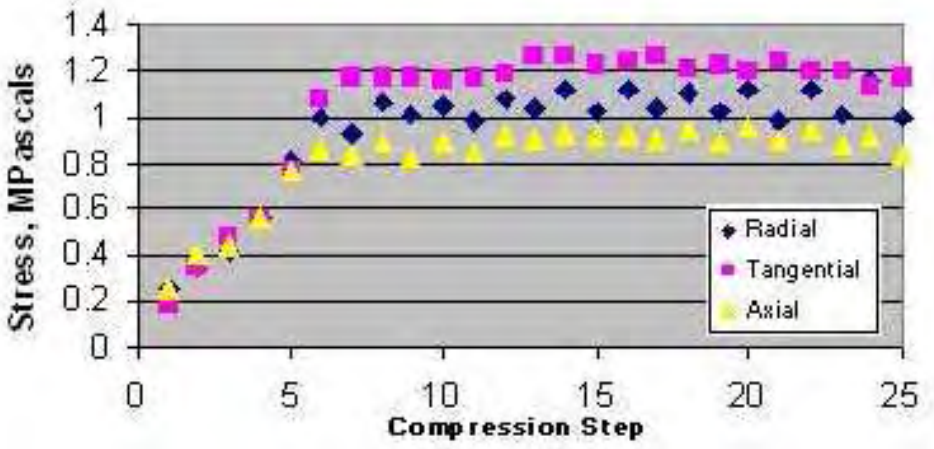

Figure 3.9 Stress per compression for the completely osteonal control bone samples. The first five compression steps make the tail portion of the compression test, where the stress is increasing till the linear elastic portion of the compression is reached. Stress experienced by radially compressed samples displays spring-like behavior.

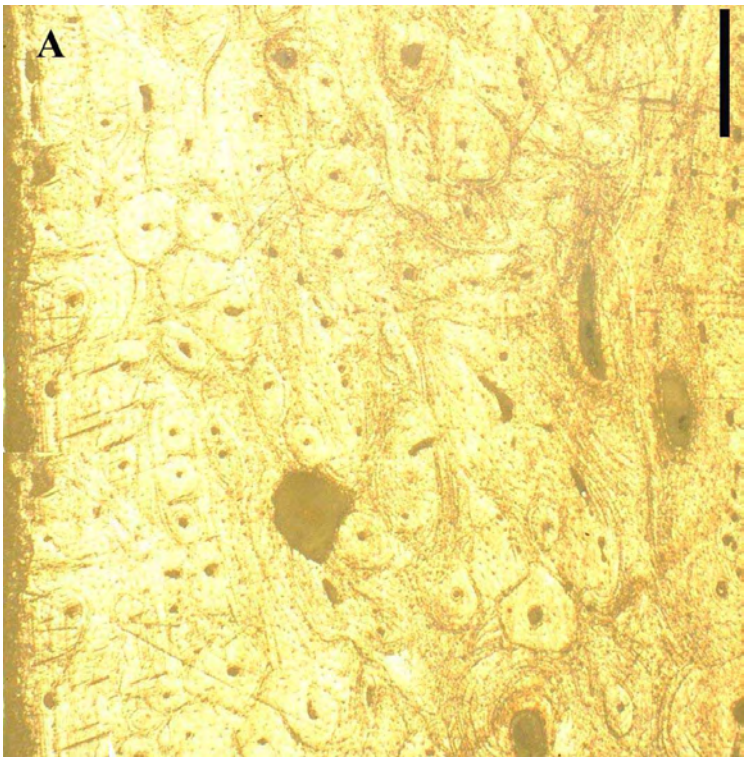

Figure 3.10 Strain and elastic modulus distributions for the radially compressed completely osteonal control bone sample O1 PU. Images are oriented such that the bone sample appears to have been loaded from left to right. In the following images, periosteum is to the left and endosteum is to the right. For images B-D, colorbars indicate strain and the unit of length for the abscissa and ordinate is pixel number, where the pixel length is approximately 12 micrometers. (A) The micrograph of sample O1 PU (scale bar, 300 micrometers) ; (B) X-strain distribution across the surface of the bone, obtained from X-displacement data, u(i,j); (C) xy-shear strain distribution across the surface of the bone, obtained from X and Y-displacement data; (D) Y-strain distribution across the surface of bone, obtained from Y-displacement data, v(i,j). Compare strain distribution image with the locations of the holes in the micrograph in this figure. For images E-F, the unit of length for the abscissa is pixel number, where the pixel length is approximately 12 micrometers. (E) Y-strain distribution profile, the ordinate indicates strain. (F) Elastic modulus distribution profile obtained from strain distribution data. The ordinate indicates elastic modulus in GPa.

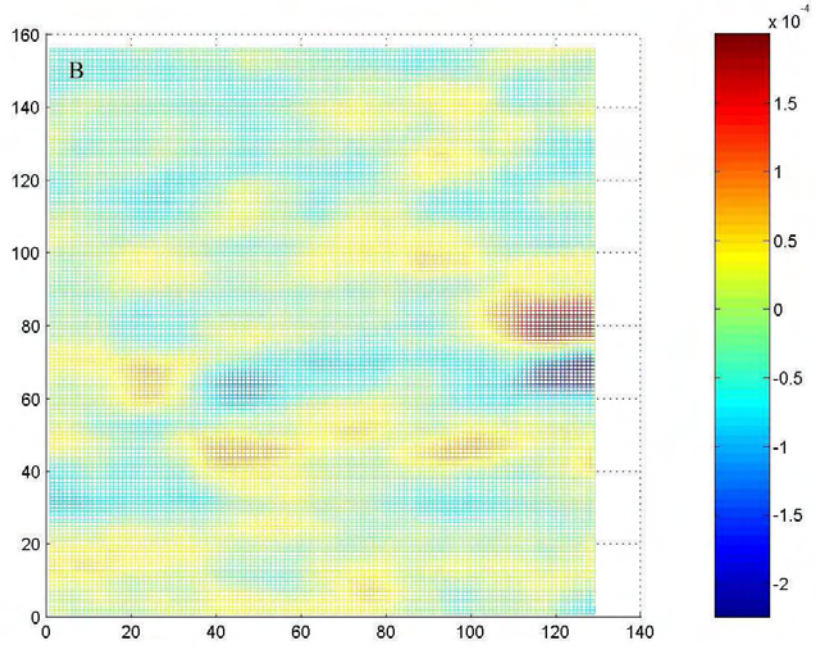
B
x 10^-4
1.5
1
0.5
0
-0.5
-1
-1.5
-2
0
20
40
60
80
100
120
140
160

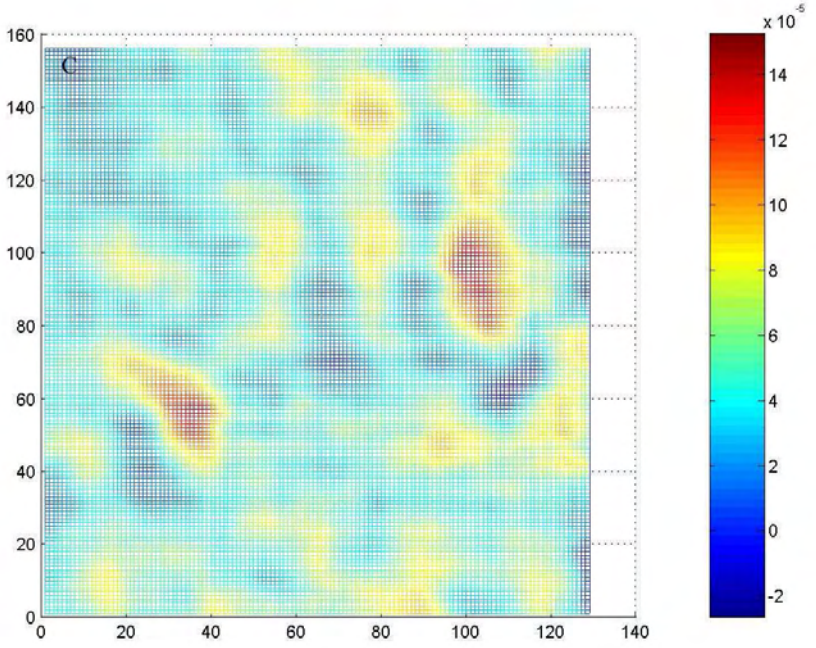
C
x 10^-5
14
12
10
8
6
4
2
0
-2
0
20
40
60
80
100
120
140
160

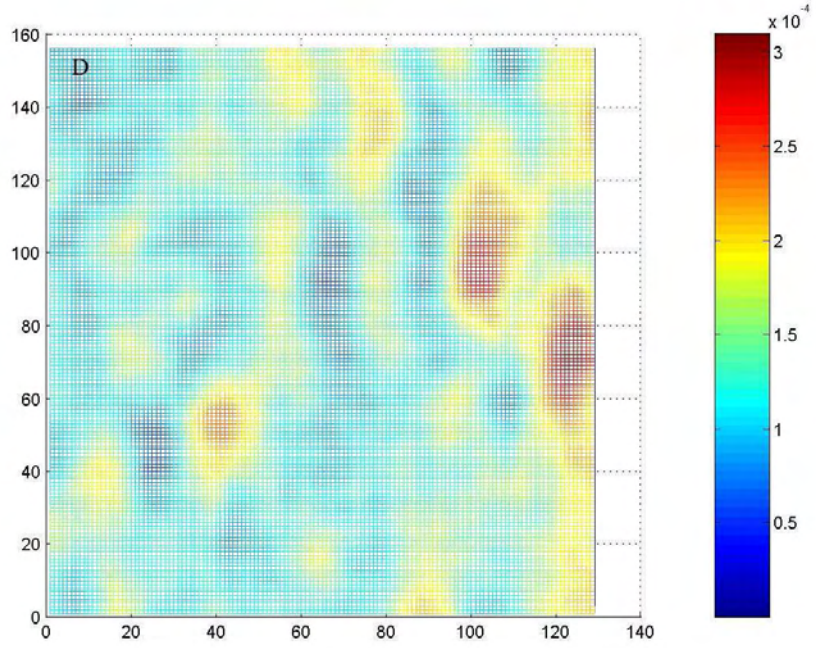
D
x 10^-4
3
2.5
2
1.5
1
0.5
0
20
40
60
80
100
120
140
160

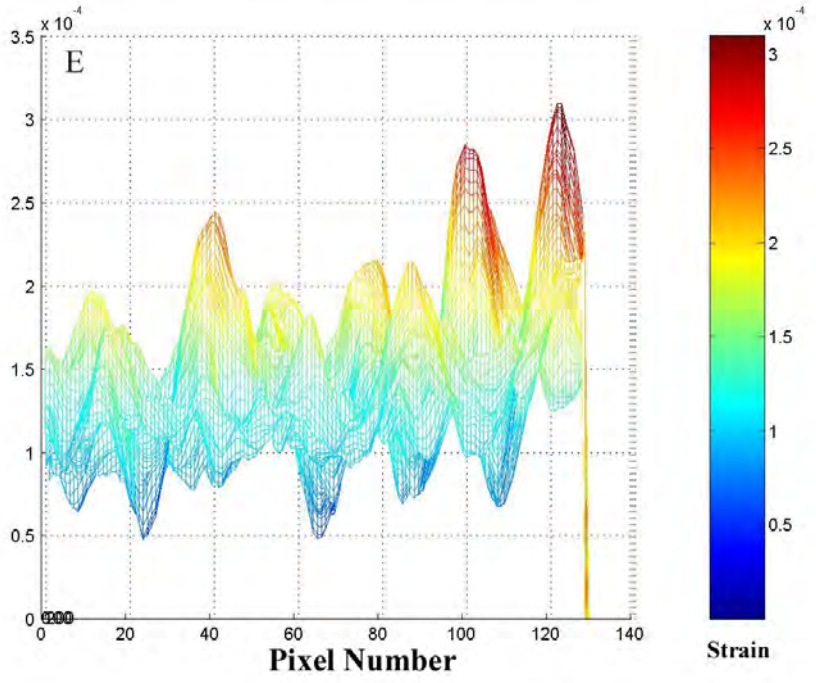
E
x 10^-4
3.5
3
2.5
2
1.5
1
0.5
0
20
40
60
80
100
120
140
Pixel Number
Strain

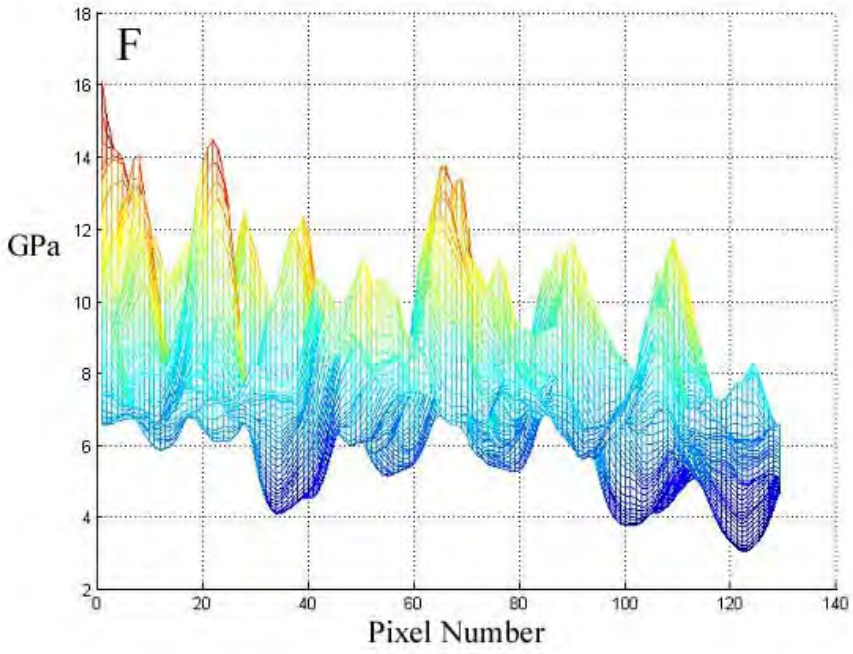
F
GPa
18
16
14
12
10
8
6
4
2
0
20
40
60
80
100
120
140
Pixel Number

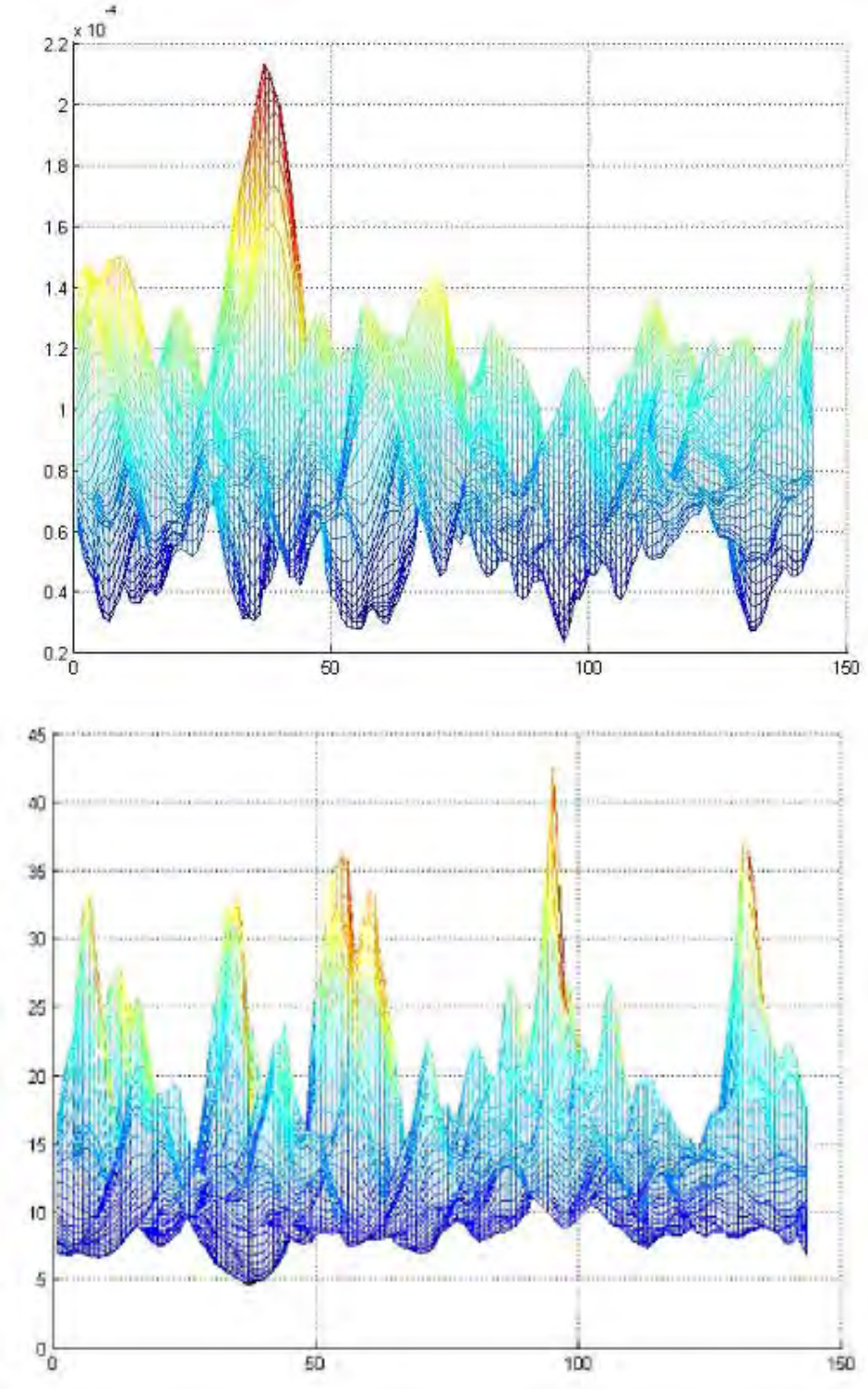

Figure 3.11 Strain and elastic modulus distributions for the tangentially compressed completely osteonal control bone sample O1 PU. In the above images, periosteum is to the right and endosteum is to the left. In both images, the unit of length for the abscissa is pixel number, where the pixel length is approximately 12 micrometers. (top) Y-strain distribution profile, the ordinate indicates strain. The site of high strain correlates with about the site of the resorption cavity in the sample. (bottom) Profile of the reciprocal of y-strain distribution. The ordinate indicates elastic modulus in GPa.

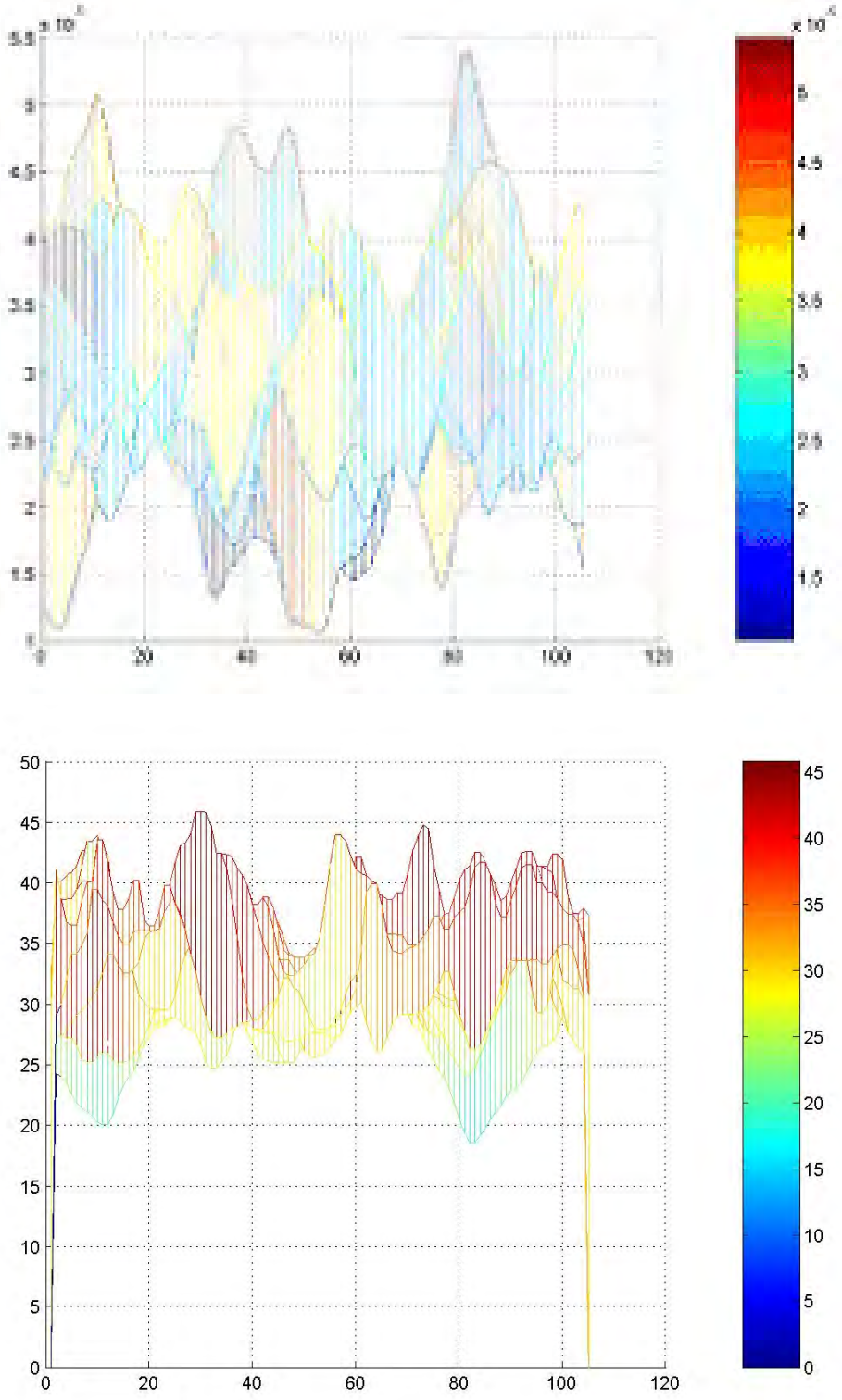

Figure 3.12 Strain and elastic modulus distributions for the axially compressed completely osteonal control bone sample O1 PU. In the above images, periosteum is to the right and endosteum is to the left. In both images, the unit of length for the abscissa is pixel number, where the pixel length is approximately 12 micrometers. (top) Y-strain distribution profile, the ordinate indicates strain. (bottom) Profile of the reciprocal of y-strain distribution for the axially compressed completely osteonal control bone. The ordinate indicates elastic modulus in GPa.

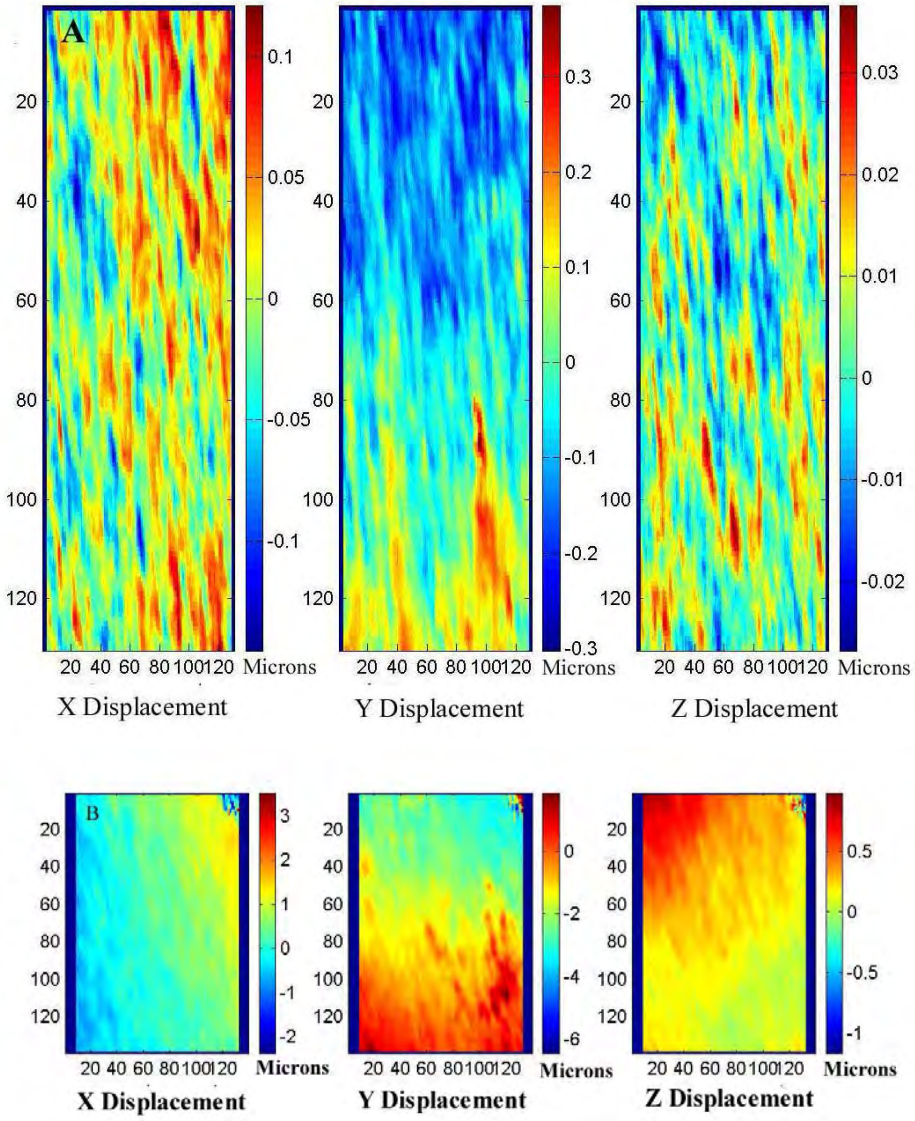

Figure 3.13 X, Y and Z total displacement maps for the five partially osteonal bones compressed radially. (From A-F) B4 PU, B5 PD, B8 PU, B8 PD, B14 PD, B20 PD. PU indicates that the sample was loaded from periosteum (at the top of the image) to the endosteum, while PD indicates that the sample was loaded from the endosteum to the periosteum (at the bottom of the image). In all images, the unit of length for the abscissa and the ordinate is pixel number, where the pixel length is approximately 12 micrometers. Colorbars indicate displacement in micrometers.

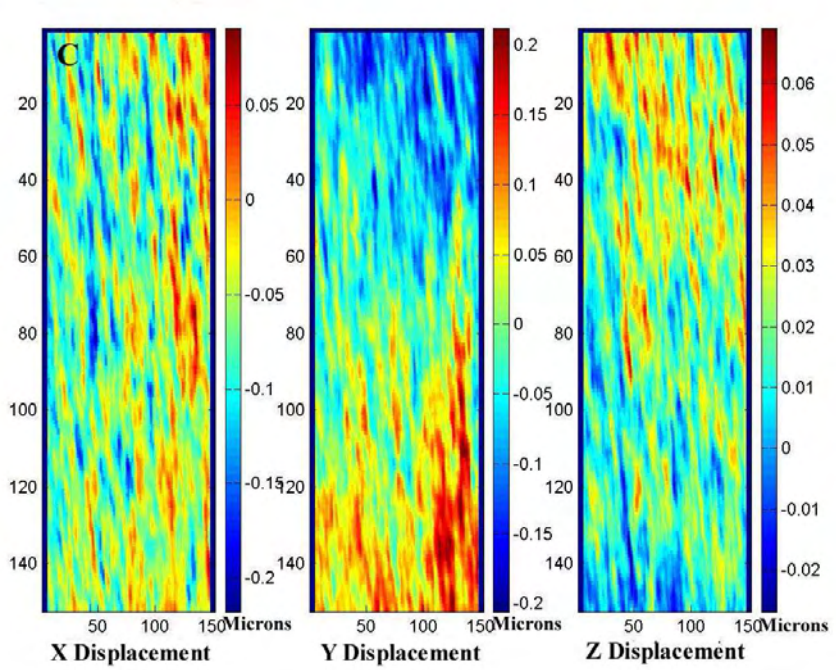
C
X Displacement
Y Displacement
Z Displacement
Microns

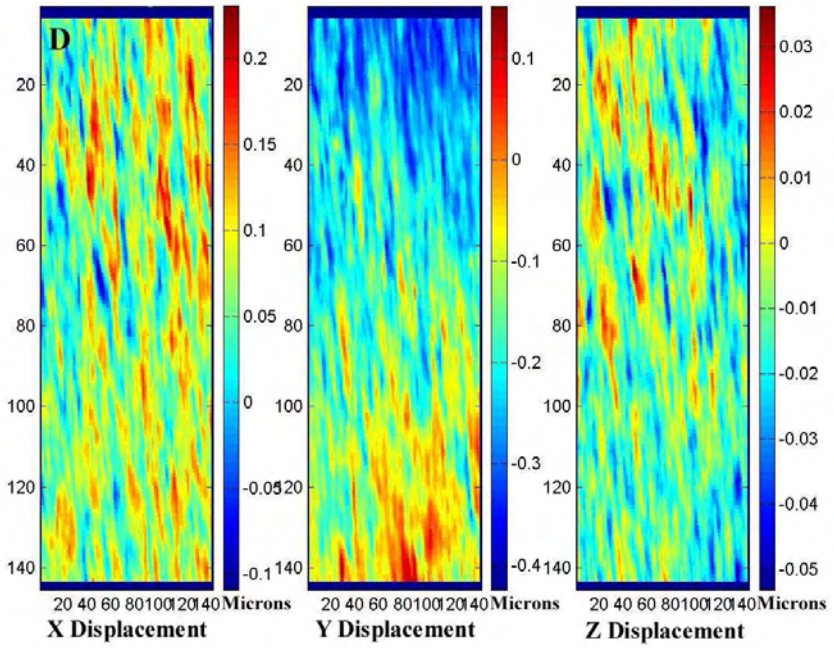
D
X Displacement
Y Displacement
Z Displacement
Microns

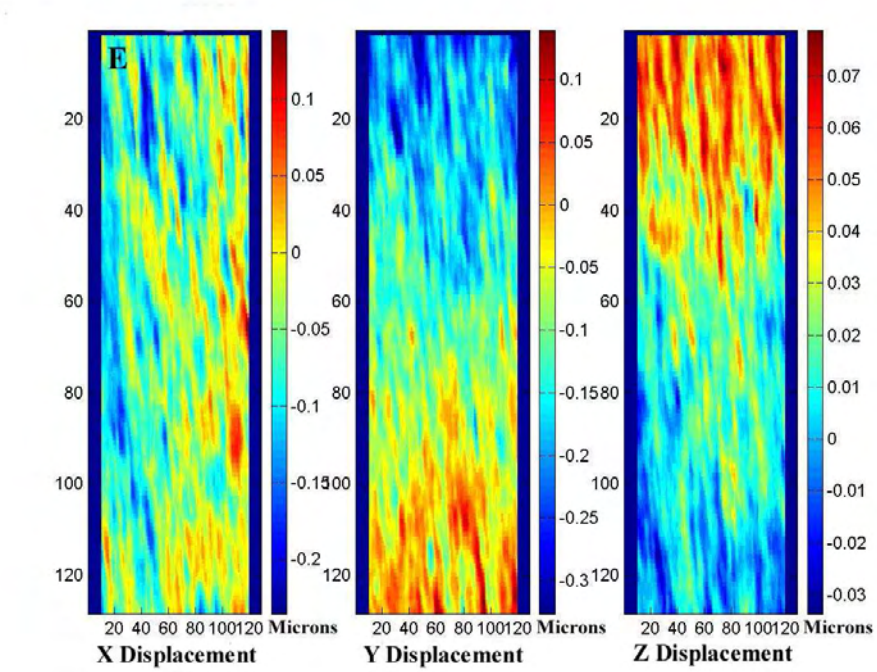
E
20 40 60 80 100120 Microns
X Displacement
20 40 60 80 100120 Microns
Y Displacement
20 40 60 80 100120 Microns
Z Displacement

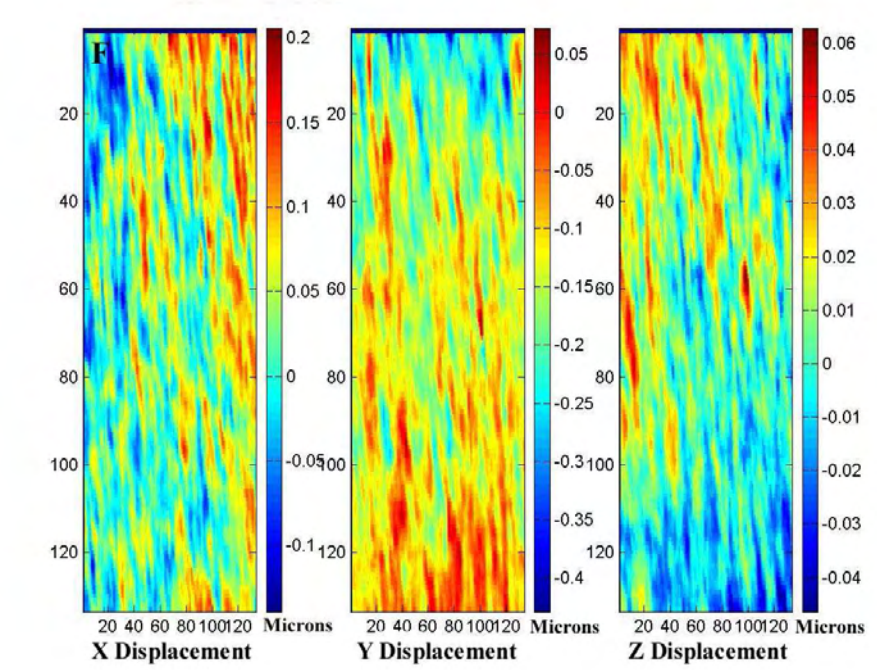
F
20 40 60 80 100120 Microns
X Displacement
20 40 60 80 100120 Microns
Y Displacement
20 40 60 80 100120 Microns
Z Displacement

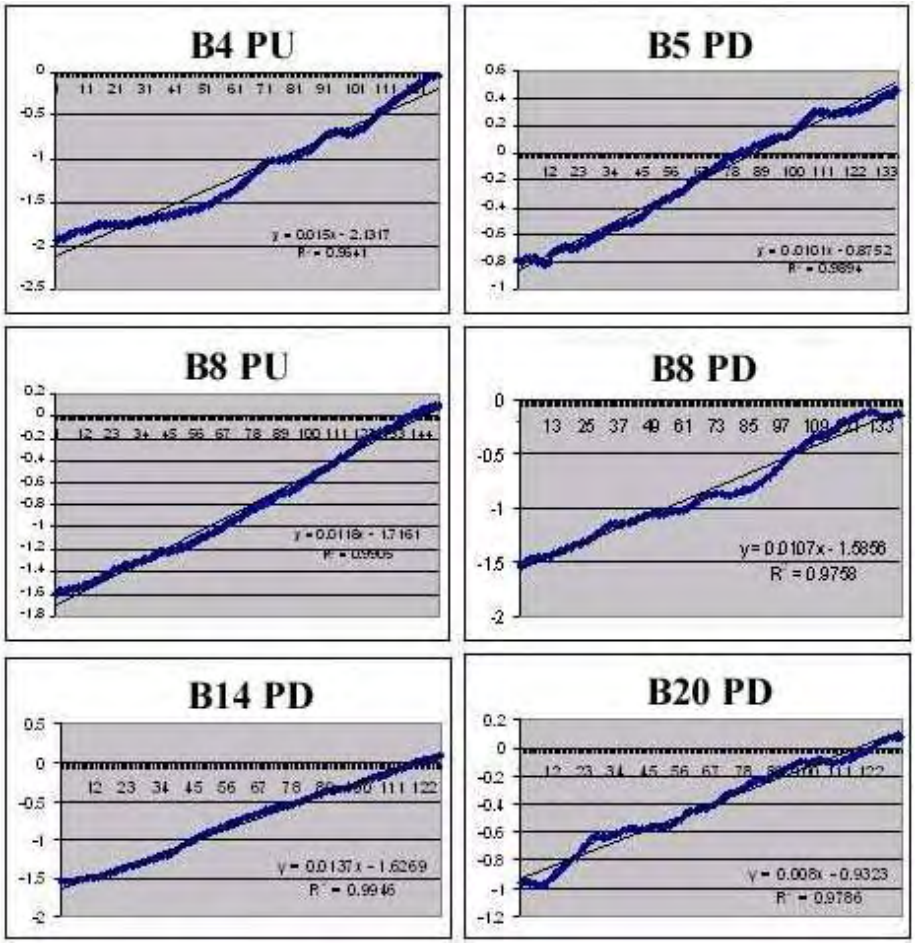

Figure 3.14 Linearity plots for the partially osteonal bones compressed radially, B4 PU, B5 PD, B8 PU, B8 PD, B14 PD, B20 PD. For the PU bones, periosteum is to the left of the plot; for the PD bones, it is to the right of the plot. The abscissa indicates pixel number, where the pixel length is approximately 12 micrometers. The ordinate indicates displacement in micrometers. Each end of the plot was used to calculate the difference in displacement unique to the CLB and OB regions of the bone samples.

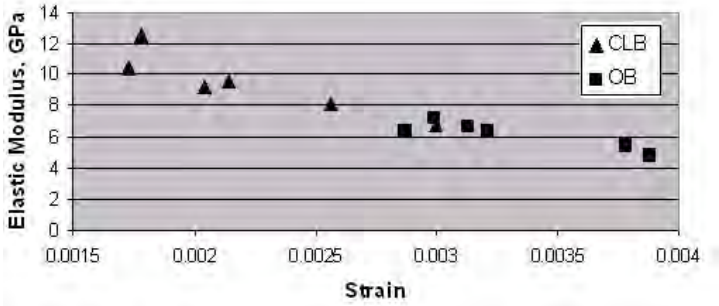

Figure 3.15 Graphic showing variation of calculated elastic modulus of circumferential lamellar and osteonal bones with strain.

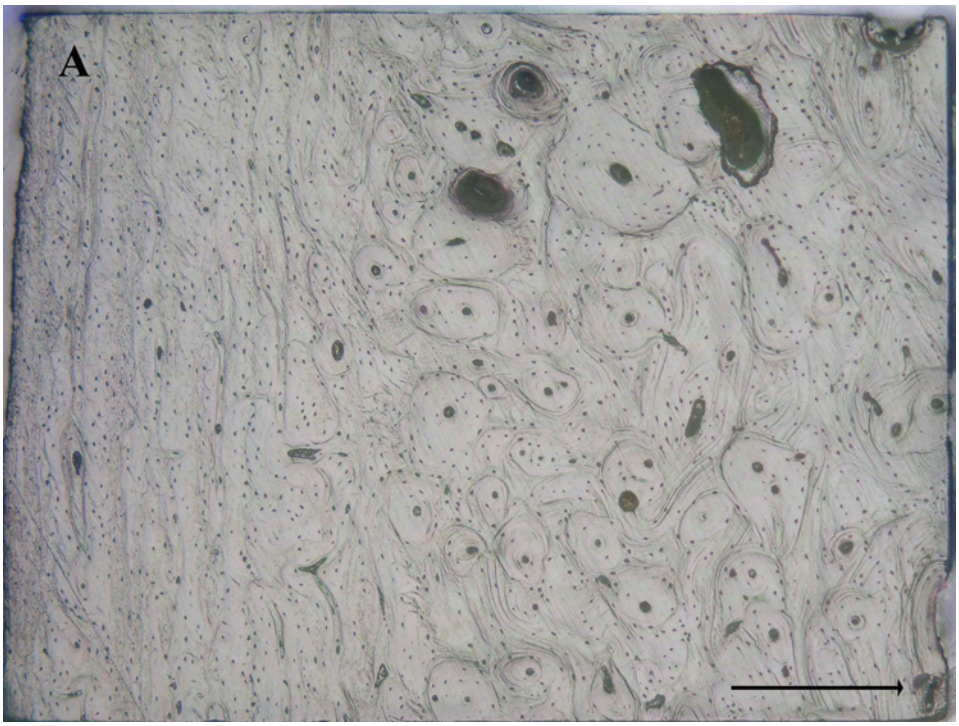

Figure 3.16 Strain and elastic modulus distributions for the radially compressed partially osteonal bone sample B8 PU. Images are oriented such that the bone sample appears to have been loaded from left to right. In the following images, periosteum is to the left and endosteum is to the right. For images B-D, colorbars indicate strain and the unit of length for the abscissa and ordinate is pixel number, where the pixel length is approximately 12 micrometers. (A) The micrograph of sample B8 PU (scale bar, 300 micrometers); (B) X-strain distribution across the surface of the bone, obtained from X-displacement data, u(i,j); (C) xy-shear strain distribution across the surface of the bone, obtained from X and Y-displacement data; (D) Y-strain distribution across the surface of bone, obtained from Y-displacement data, v(i,j). For images E-F, the unit of length for the abscissa is pixel number, where the pixel length is approximately 12 micrometers. (E) Y-strain distribution profile, the ordinate indicates strain. (F) Elastic modulus distribution profile obtained from strain distribution data. The ordinate indicates elastic modulus in GPa.

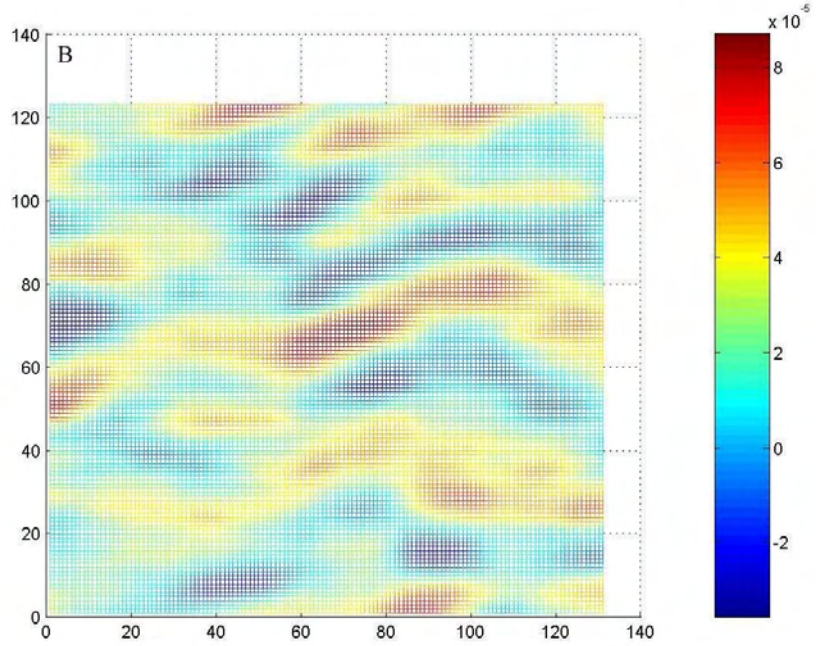
B
x 10^-5
140
120
100
80
60
40
20
0
0
20
40
60
80
100
120
140
8
6
4
2
0
-2

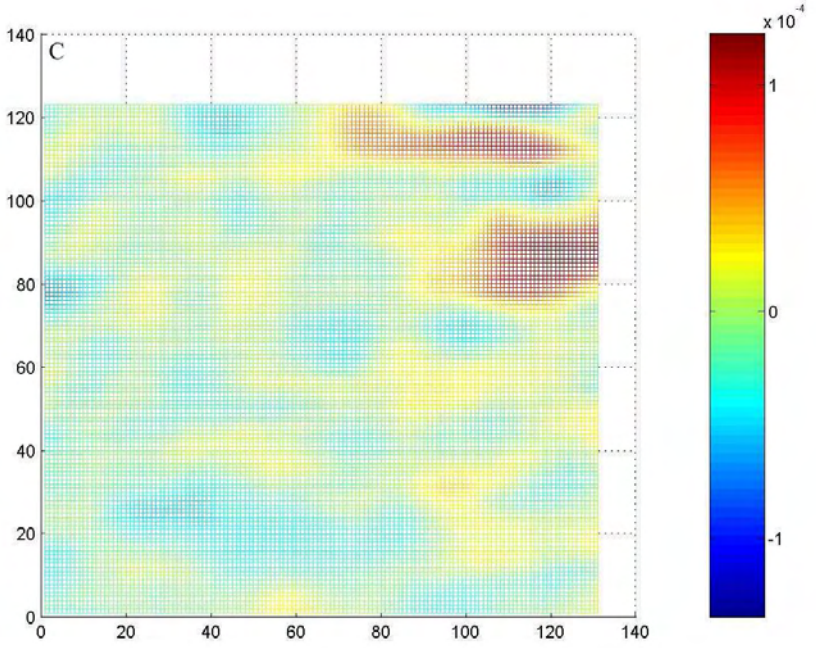
C
x 10^-4
140
120
100
80
60
40
20
0
0
20
40
60
80
100
120
140
1
0
-1

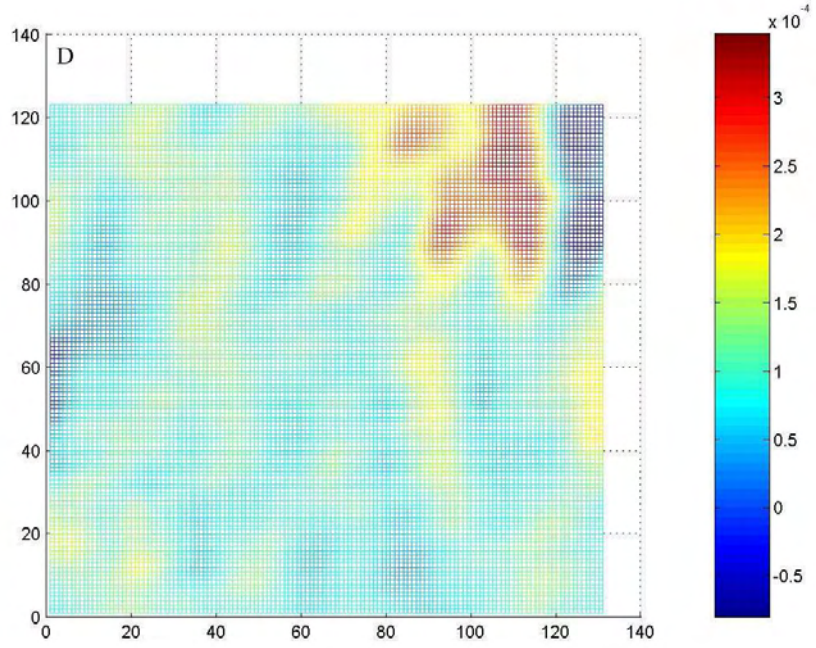
D
x 10^-4
140
120
100
80
60
40
20
0
0
20
40
60
80
100
120
140
3
2.5
2
1.5
1
0.5
0
-0.5

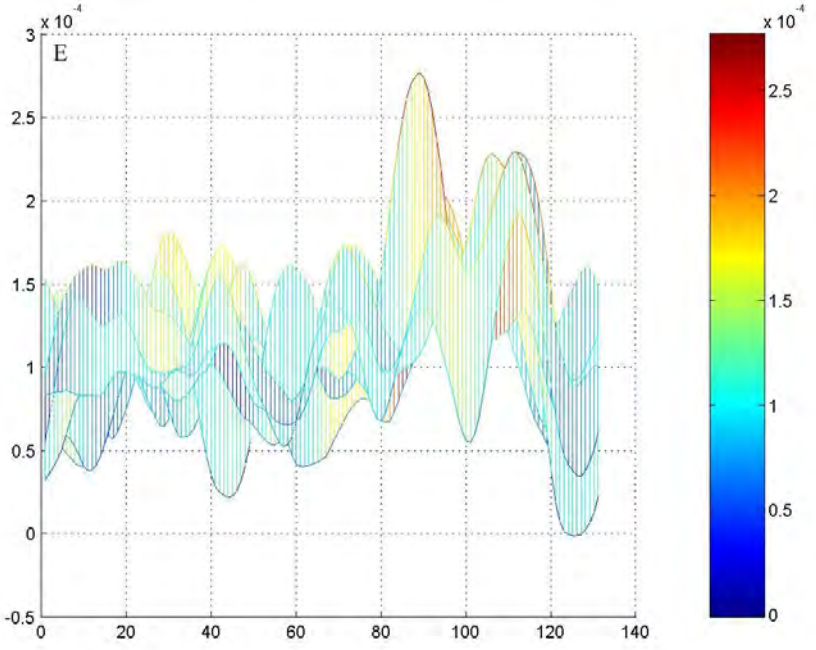
E
x 10^-4
x 10^-4
3
2.5
2
1.5
1
0.5
0
-0.5
0
20
40
60
80
100
120
140
2.5
2
1.5
1
0.5
0

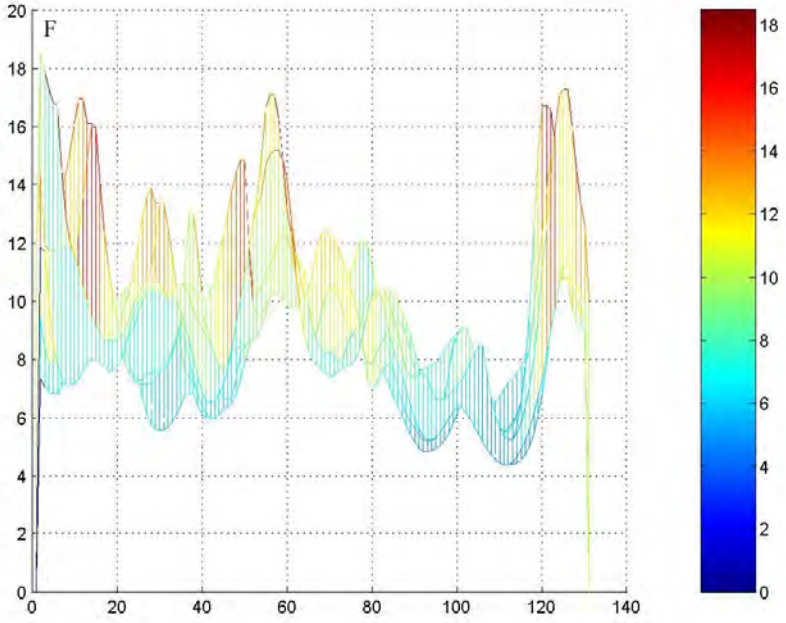
F
0
2
4
6
8
10
12
14
16
18
20
0
20
40
60
80
100
120
140
0
2
4
6
8
10
12
14
16
18

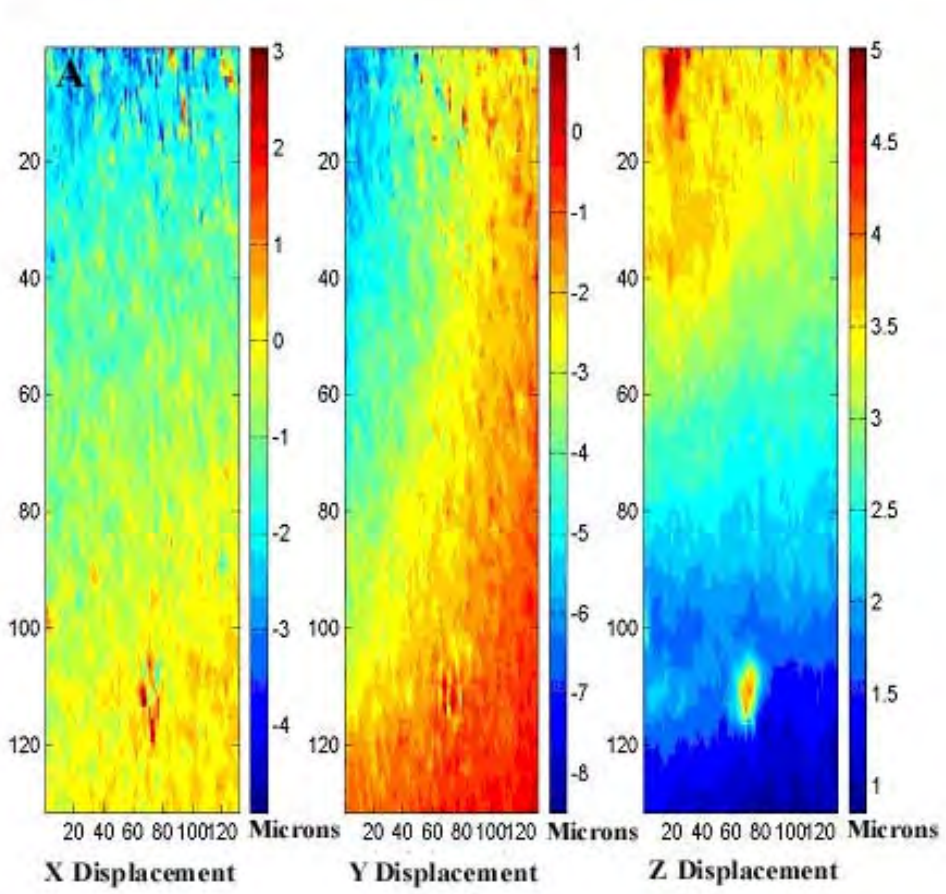

Figure 3.17 The X, Y and Z total displacement maps for the radially (A), tangentially (B) and axially (C) compressed partially osteonal bone, B1. The load is applied vertically. Colorbars indicate displacement in micrometers. The unit for the abscissa and ordinate is pixel number, where the pixel size is approximately 12 micrometers.

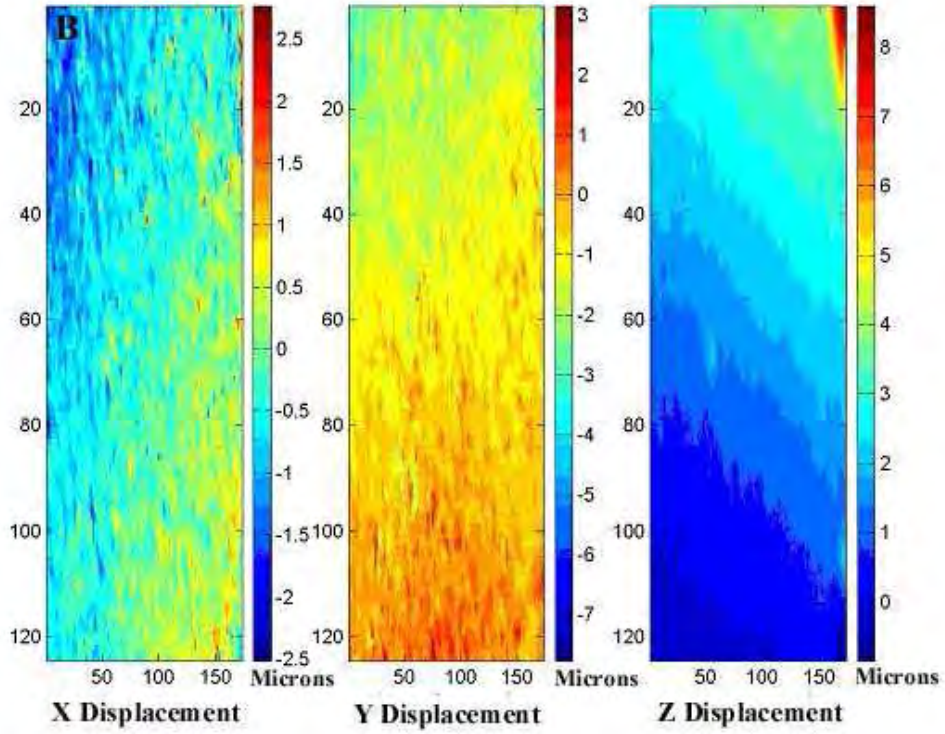
B
X Displacement
Y Displacement
Z Displacement
Microns

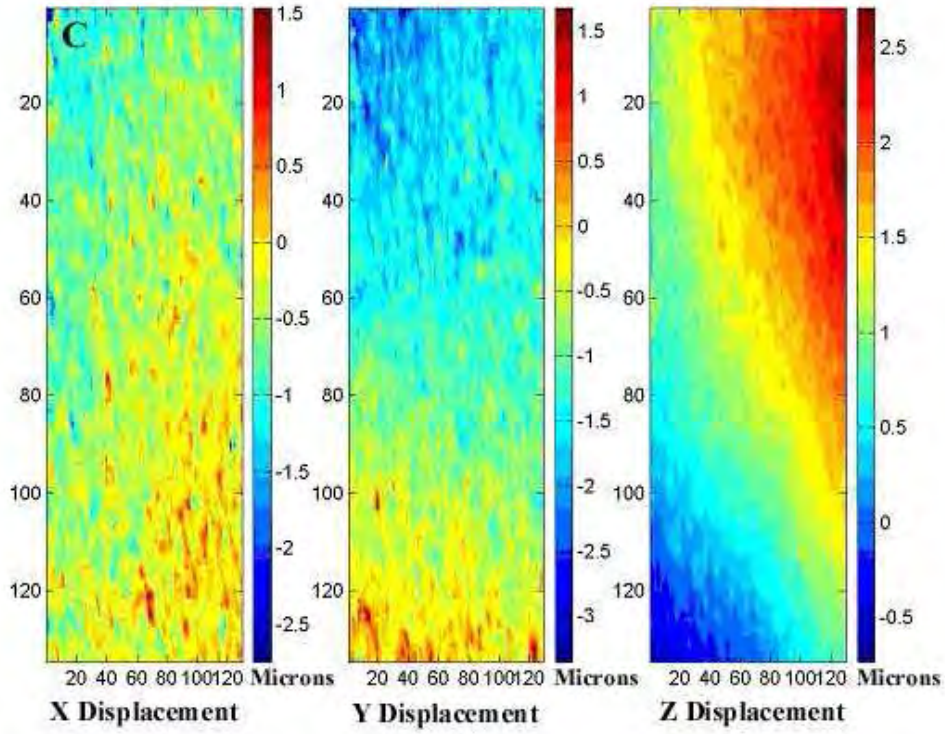
C
X Displacement
Y Displacement
Z Displacement
Microns

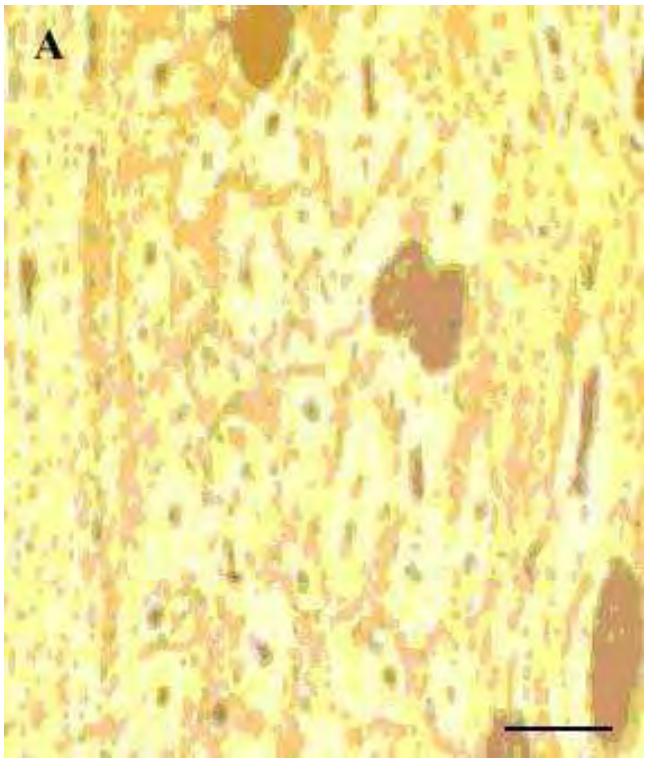

Figure 3.18 Strain and elastic modulus distributions for the radially compressed partially osteonal bone sample B1 PU. Images are oriented such that the bone sample appears to have been loaded from left to right. In the following images, periosteum is to the right and endosteum is to the left. For images B-D, colorbars indicate strain and the unit of length for the abscissa and ordinate is pixel number, where the pixel length is approximately 12 micrometers. (A) The micrograph of sample B1 PU (scale bar, 300 micrometers); (B) X-strain distribution across the surface of the bone, obtained from X-displacement data, u(i,j); (C) xy-shear strain distribution across the surface of the bone, obtained from X and Y-displacement data; (D) Y-strain distribution across the surface of bone, obtained from Y-displacement data, v(i,j). For images E-F, the unit of length for the abscissa is pixel number, where the pixel length is approximately 12 micrometers. (E) Y-strain distribution profile, the ordinate indicates strain. (F) Elastic modulus distribution profile obtained from strain distribution data. The ordinate indicates elastic modulus in GPa.

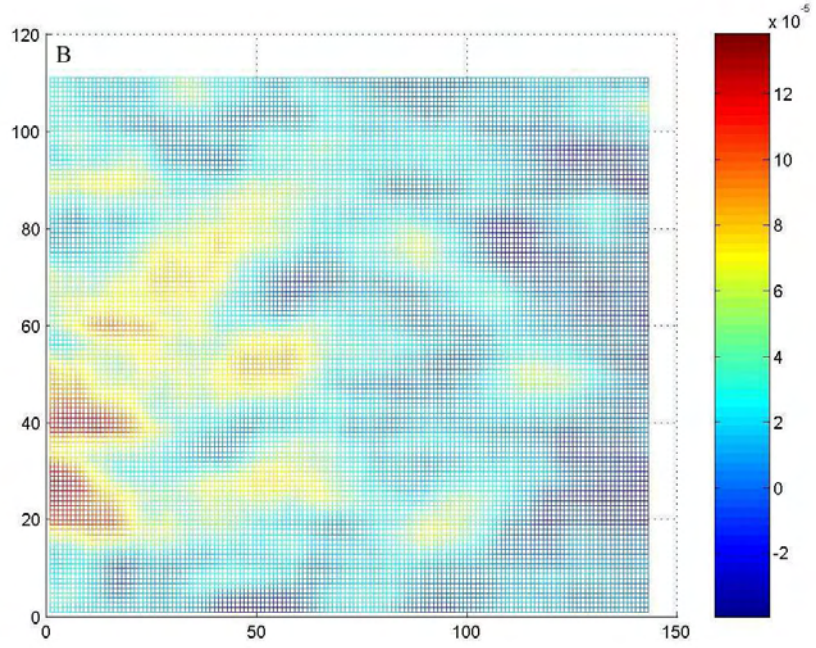
B
x 10^-5
120
100
80
60
40
20
0
0
50
100
150
12
10
8
6
4
2
0
-2

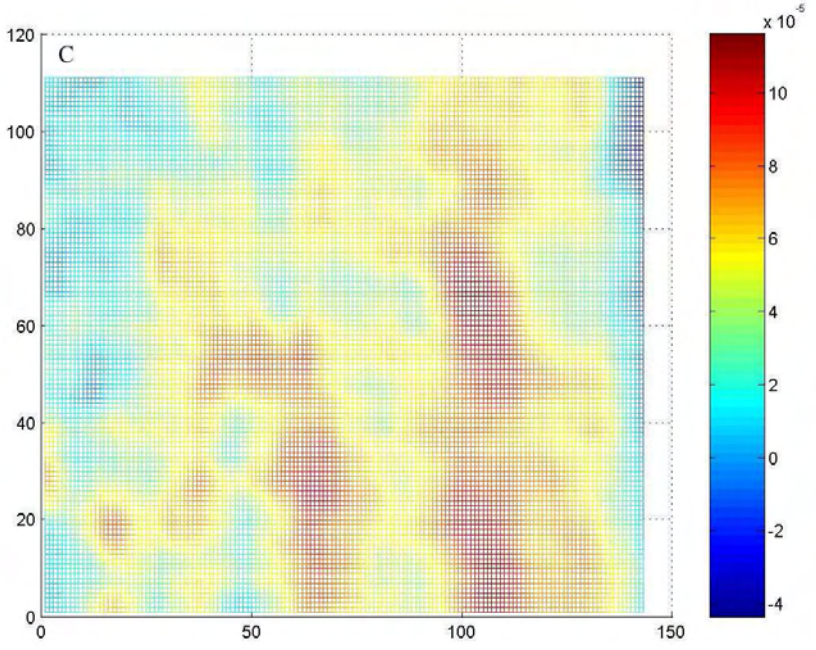
C
x 10^-5
120
100
80
60
40
20
0
0
50
100
150
10
8
6
4
2
0
-2
-4

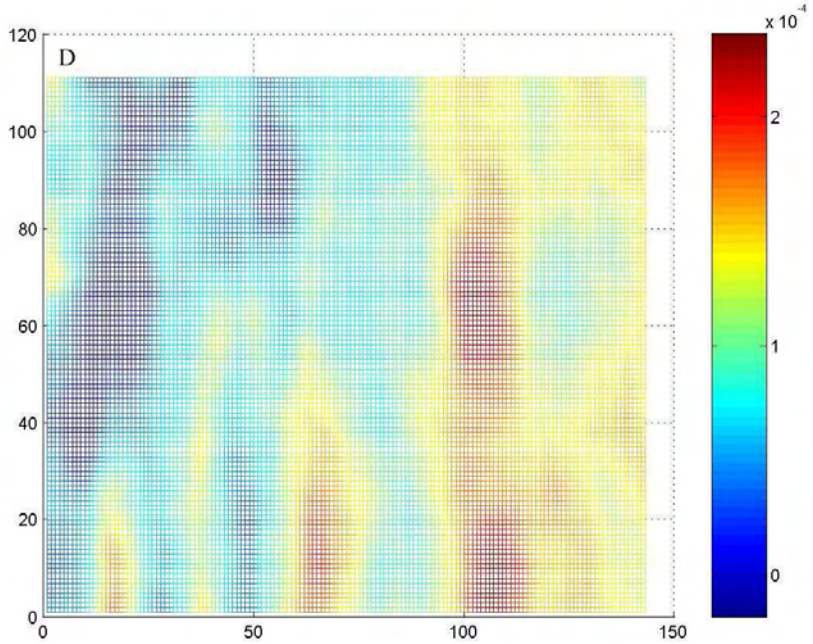
D
x 10^-4
120
100
80
60
40
20
0
0
50
100
150
2
1
0

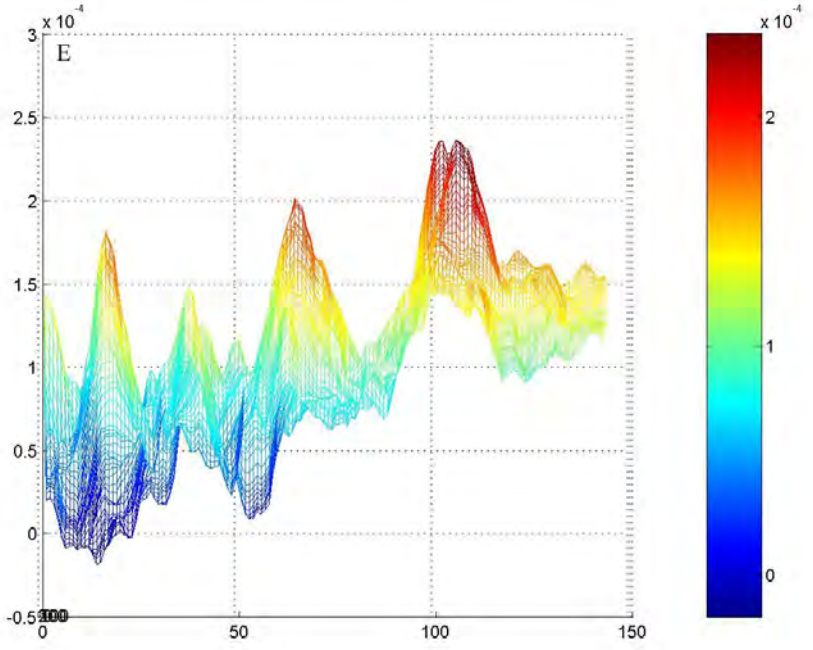
E
x 10^-4
x 10^-4
3
2.5
2
1.5
1
0.5
0
0
50
100
150
2
1
0

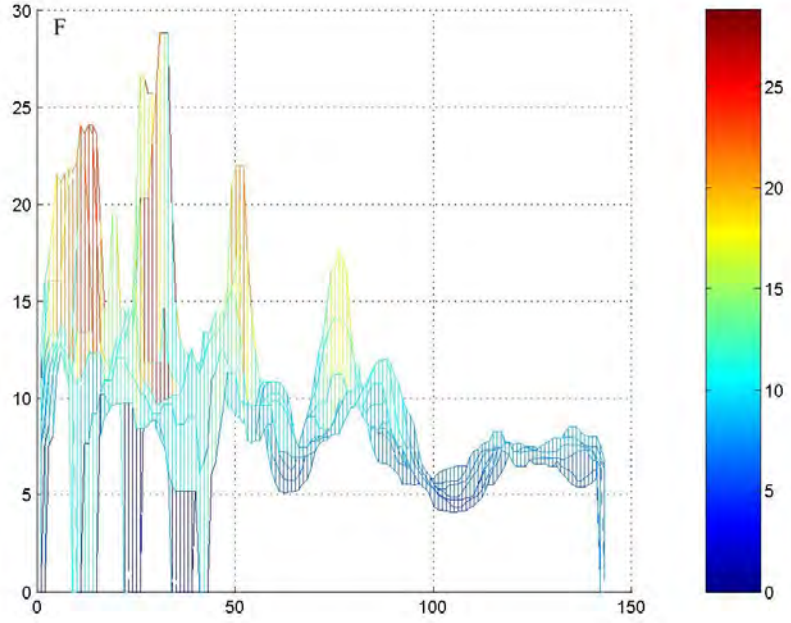
F
30
25
20
15
10
5
0
0
50
100
150
25
20
15
10
5
0

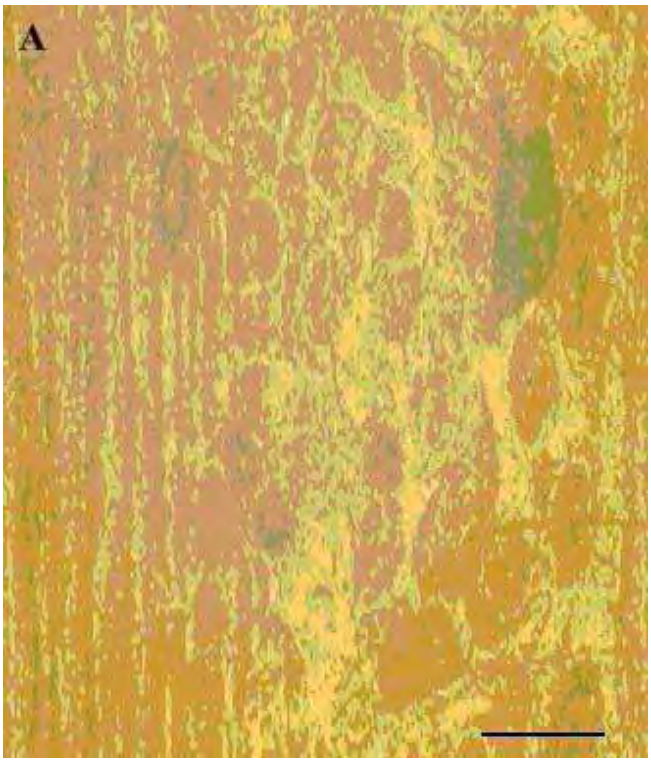

Figure 3.19 Strain and elastic modulus distributions for the radially compressed partially osteonal bone sample B2 PU. Images are oriented such that the bone sample appears to have been loaded from left to right. In the following images, periosteum is to the right and endosteum is to the left. For images B-D, colorbars indicate strain and the unit of length for the abscissa and ordinate is pixel number, where the pixel length is approximately 12 micrometers. (A) The micrograph of sample B2 PU (scale bar, 300 micrometers); (B) X-strain distribution across the surface of the bone, obtained from X-displacement data, u(i,j); (C) xy-shear strain distribution across the surface of the bone, obtained from X and Y-displacement data; (D) Y-strain distribution across the surface of bone, obtained from Y-displacement data, v(i,j). For images E-F, the unit of length for the abscissa is pixel number, where the pixel length is approximately 12 micrometers. (E) Y-strain distribution profile, the ordinate indicates strain. (F) Elastic modulus distribution profile obtained from strain distribution data. The ordinate indicates elastic modulus in GPa.

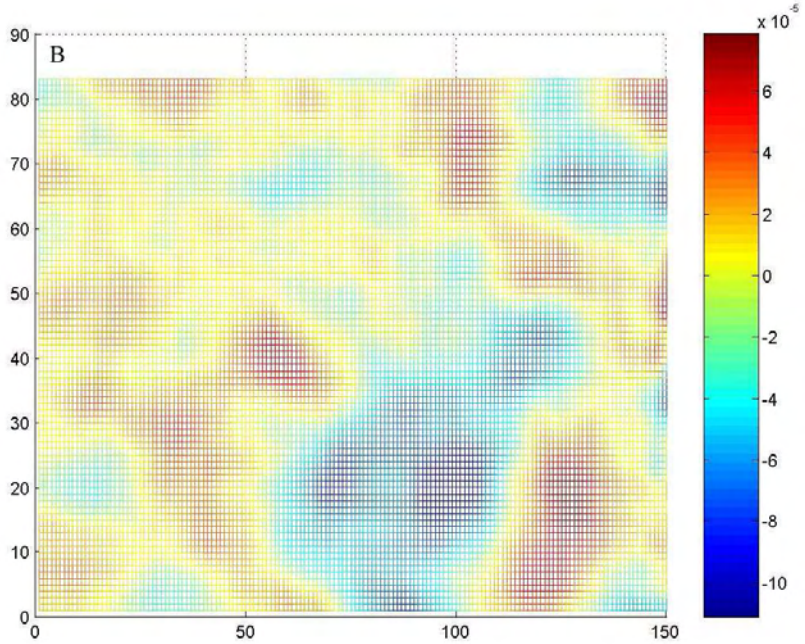
B
x 10^-5
6
4
2
0
-2
-4
-6
-8
-10
90
80
70
60
50
40
30
20
10
0
0
50
100
150

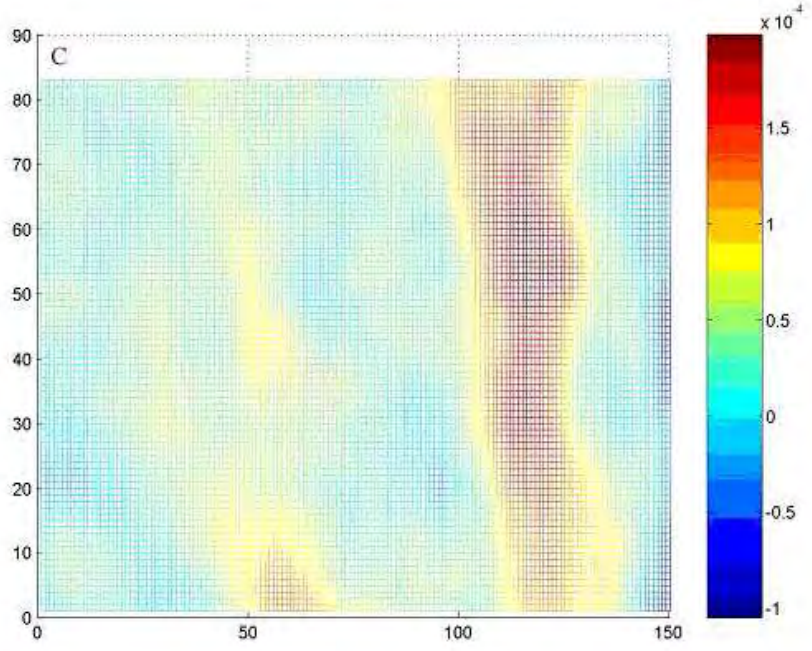
C
x 10^-4
1.5
1
0.5
0
-0.5
-1
90
80
70
60
50
40
30
20
10
0
0
50
100
150

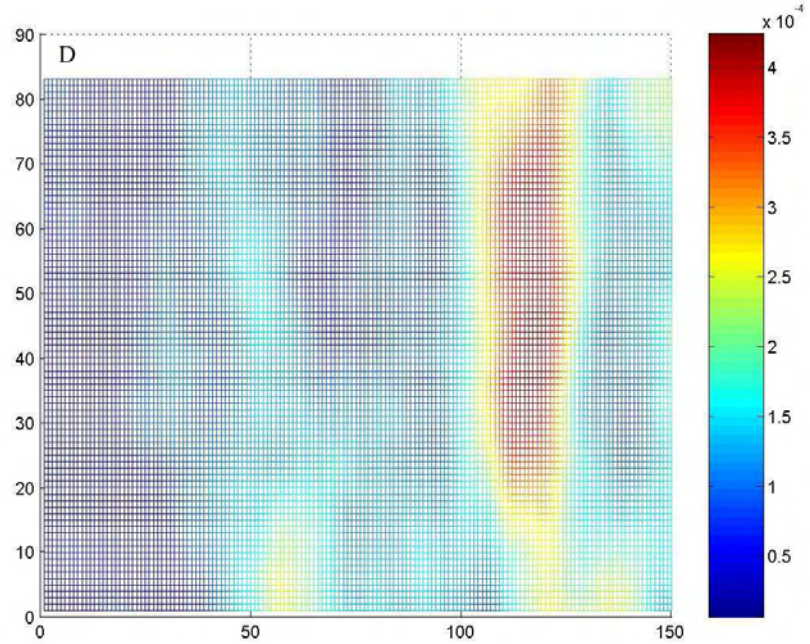
D
x 10^-4
90
80
70
60
50
40
30
20
10
0
0
50
100
150
4
3.5
3
2.5
2
1.5
1
0.5

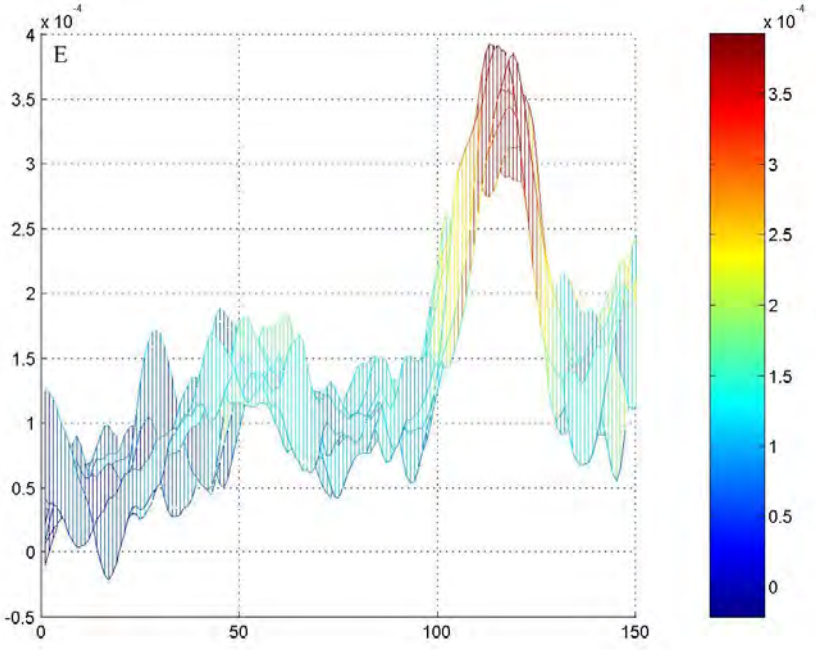
E
x 10^-4
4
3.5
3
2.5
2
1.5
1
0.5
0
-0.5
0
50
100
150
x 10^-4
3.5
3
2.5
2
1.5
1
0.5
0

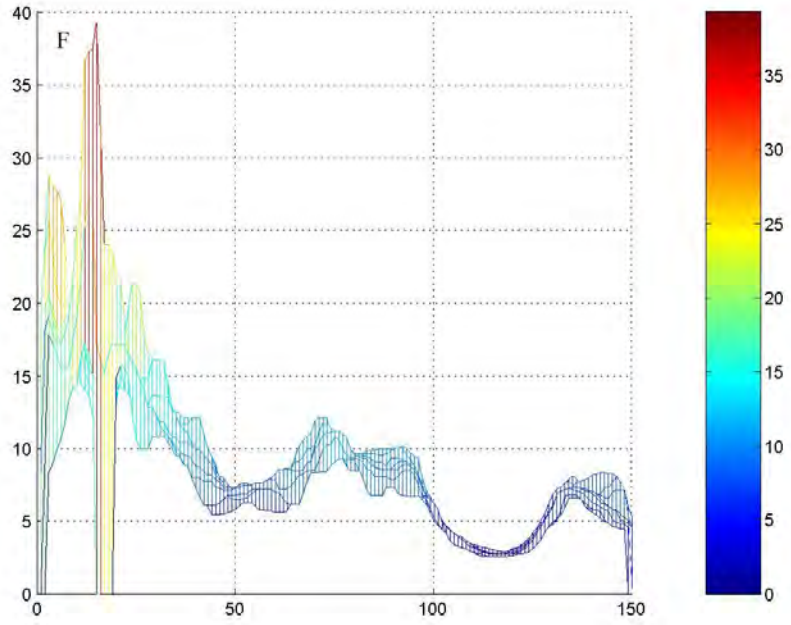
F
40
35
30
25
20
15
10
5
0
0
50
100
150
35
30
25
20
15
10
5
0

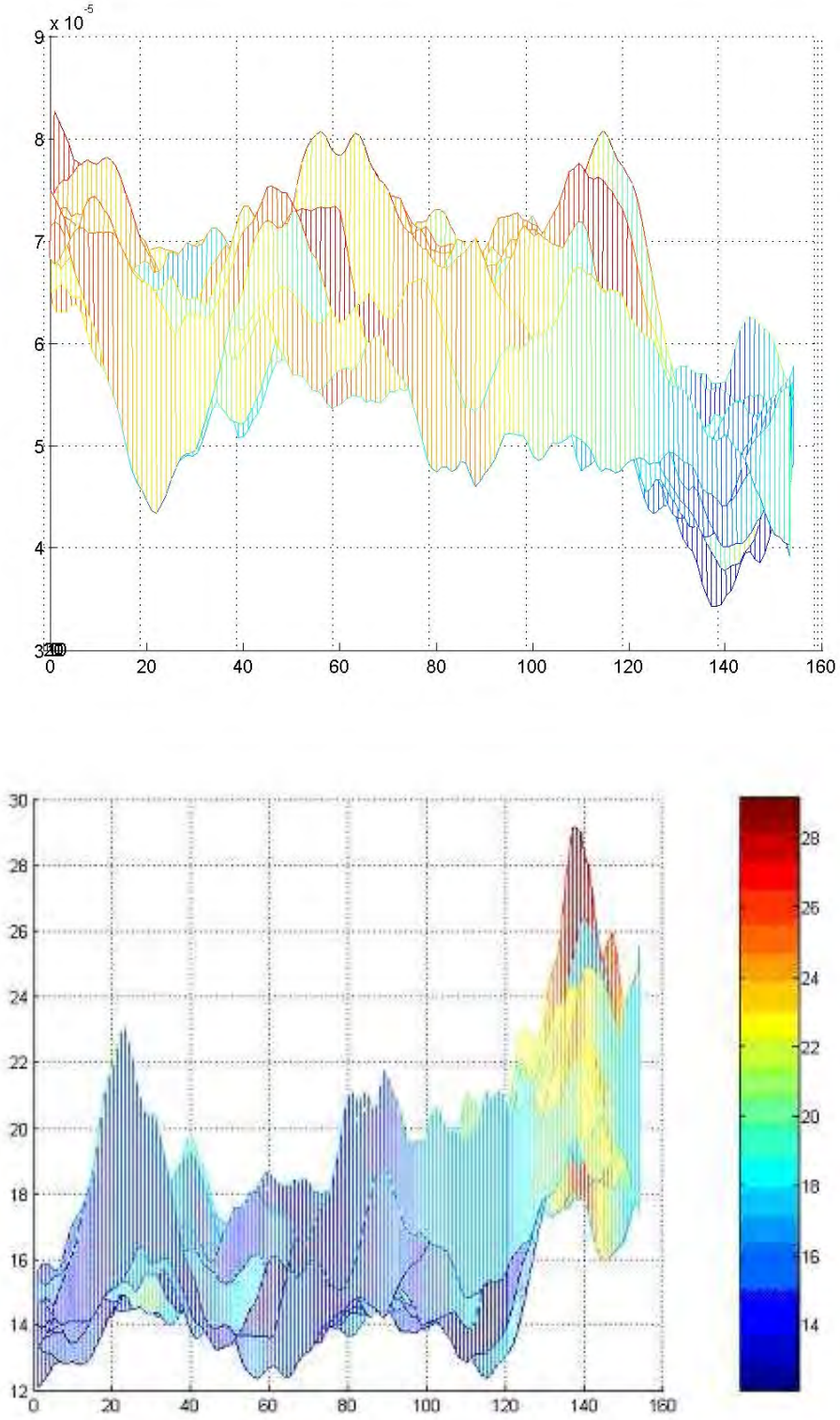

Figure 3.20 Strain and elastic modulus distributions for the tangentially compressed partially osteonal bone sample B1 PU. In the above images, periosteum is to the right and endosteum is to the left. In both images, the unit of length for the abscissa is pixel number, where the pixel length is approximately 12 micrometers. (top) Y-strain distribution profile, the ordinate indicates strain. (bottom) Profile of the reciprocal of y-strain distribution. The ordinate indicates elastic modulus in GPa.

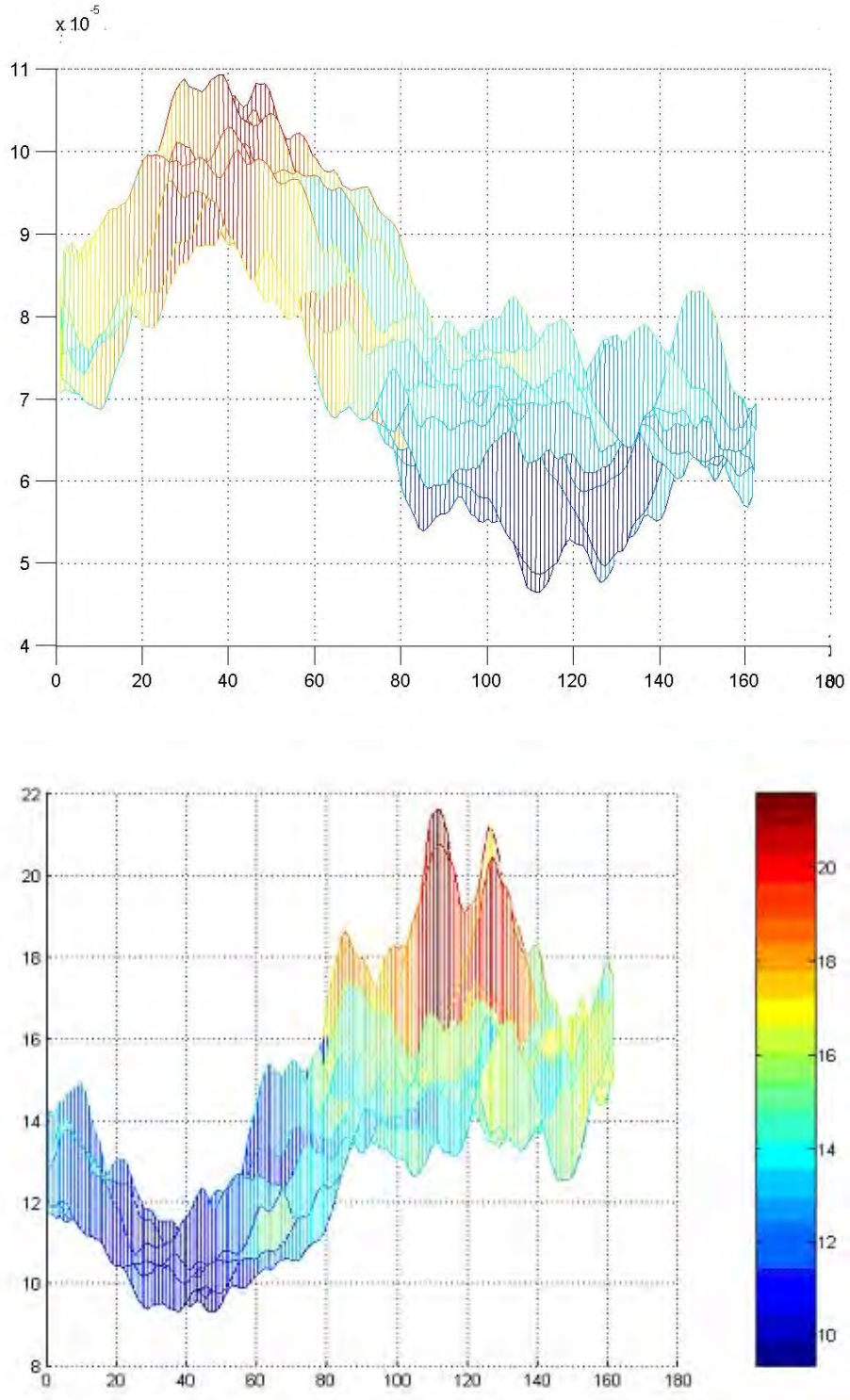

Figure 3.21 Strain and elastic modulus distributions for the tangentially compressed partially osteonal bone sample B2 PU. In the above images, periosteum is to the right and endosteum is to the left. In both images, the unit of length for the abscissa is pixel number, where the pixel length is approximately 12 micrometers. (top) Y-strain distribution profile, the ordinate indicates strain. (bottom) Profile of the reciprocal of y-strain distribution. The ordinate indicates elastic modulus in GPa.

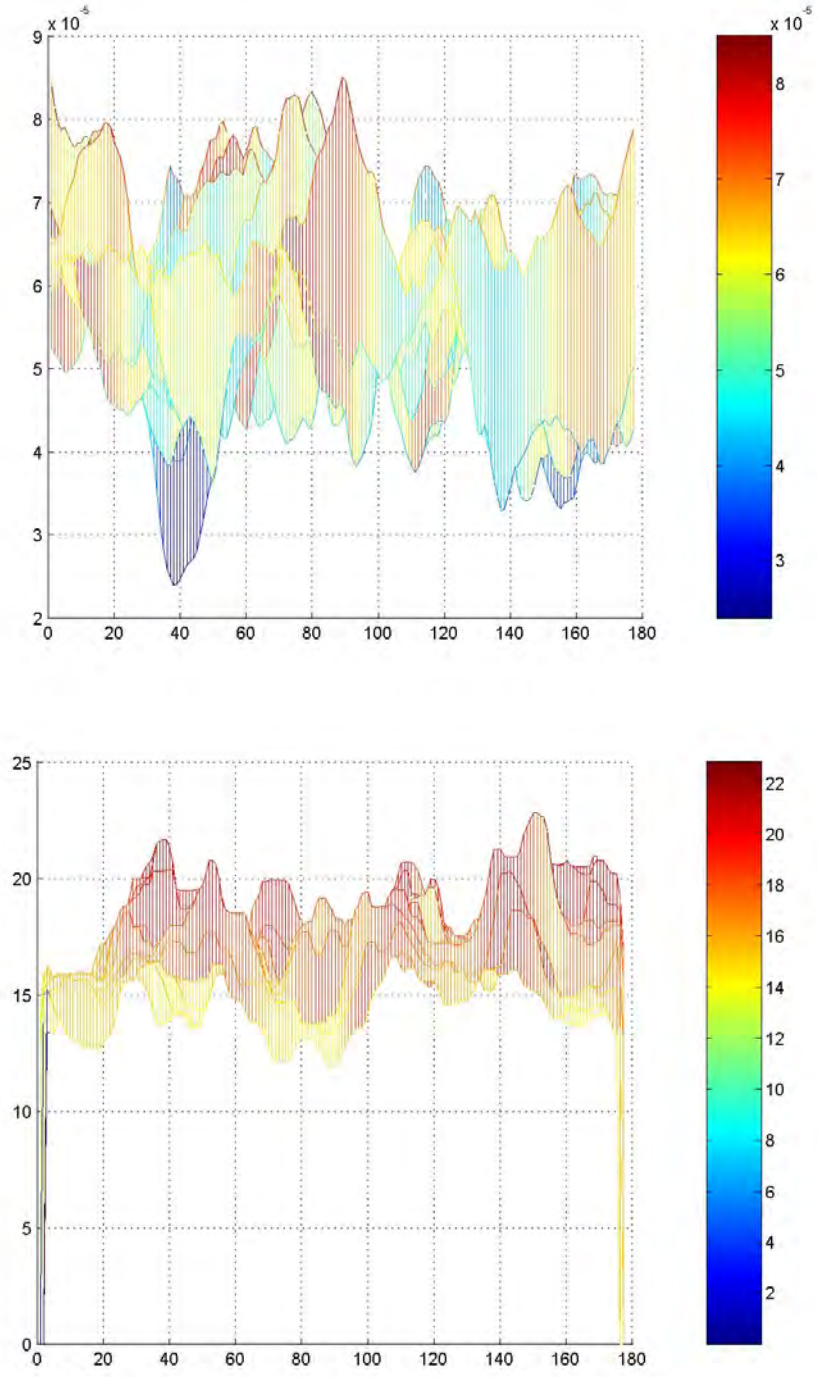

Figure 3.22 Strain and elastic modulus distributions for the axially compressed partially osteonal bone sample B1 PU. In the above images, periosteum is to the right and endosteum is to the left. In both images, the unit of length for the abscissa is pixel number, where the pixel length is approximately 12 micrometers. (top) Y-strain distribution profile. The ordinate indicates strain. (bottom) Profile of the reciprocal of y-strain distribution for the axially compressed completely osteonal control bone. The ordinate indicates elastic modulus in GPa.

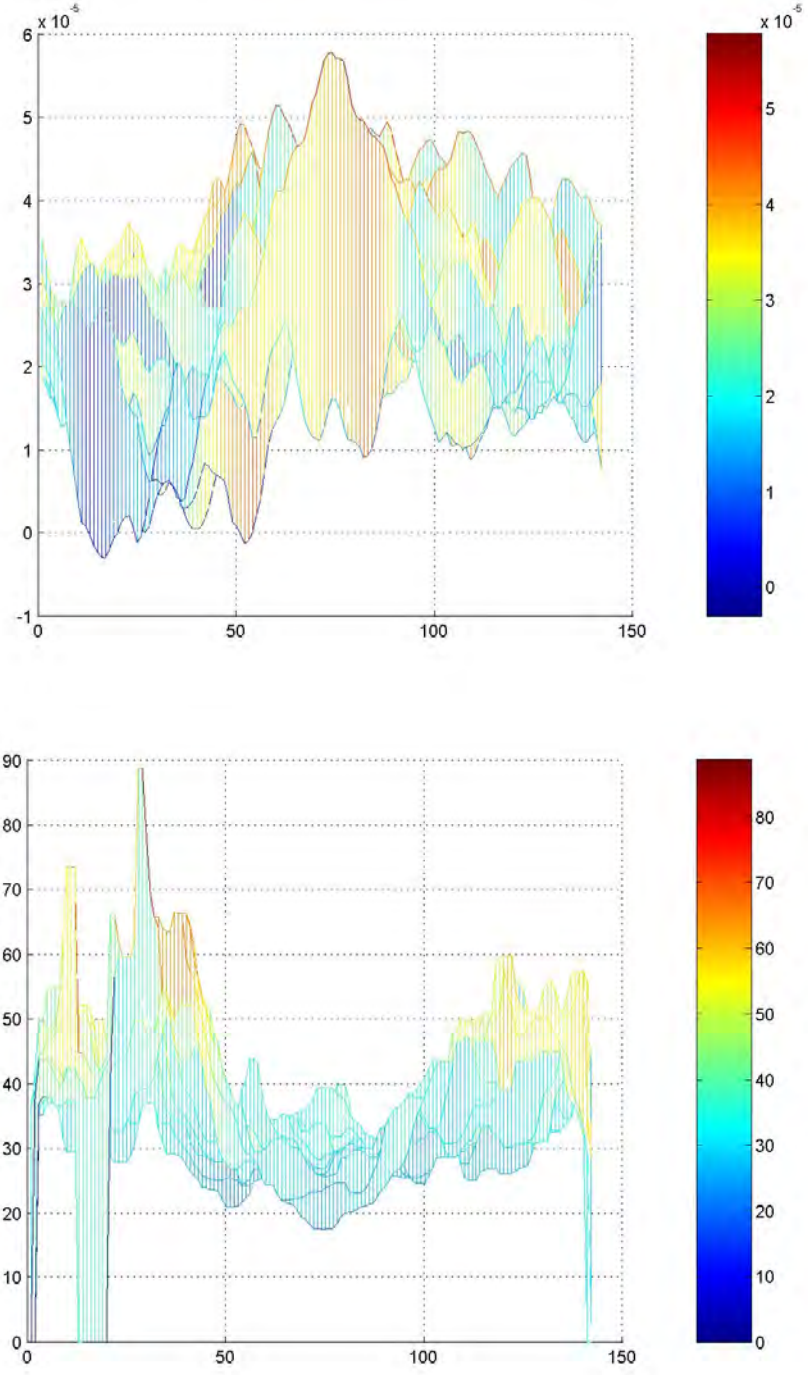

Figure 3.23 Strain and elastic modulus distributions for the axially compressed partially osteonal bone sample B2 PU. In the above images, periosteum is to the left and endosteum is to the right. In both images, the unit of length for the abscissa is pixel number, where the pixel length is approximately 12 micrometers. (top) Y-strain distribution profile. The ordinate indicates strain. (bottom) Profile of the reciprocal of y-strain distribution for the axially compressed completely osteonal control bone. The ordinate indicates elastic modulus in GPa.

4. DISCUSSION

4.1 Microstructure of Bone

This study shows that dehydration affects the dimensions of an osteon in an anisotropic manner in longitudinal sections, whereas in transverse sections the extent of contraction is almost the same in both the radial and tangential directions. Using back scattered electron imaging, it was shown that each lamella has a less mineralized portion that could contract more during dehydration, which is suggested, in part, to be responsible for this unusual contraction behavior. Therefore, the present study presents new structural information on individual lamellae and provides insight into the nature of the water component in lamellar bone.

It is known that the equatorial spacing of collagen fibril decreases with dehydration both in mineralized and unmineralized tissues. We investigated the collagen fiber organization and differences in mineralization within the lamellae with an emphasis on the role and location of water in the tissue. Our results beckon the importance of water not only on the mechanical properties of bone, but also in the anisotropic organization of the three bone components in the direction of highest loading: in longitudinal sections, dehydration causes significant contraction perpendicular to lamellae without any change in dimension in the direction parallel to lamellae at both relative humidities (Table 2.11). In transverse sections however, although radial contraction at higher humidity is significantly different from that of transverse, at lower humidity, contractions in both directions equal one another (Table 2.12). Transverse section results imply that radial contraction is consequently pursued by tangential contraction. The radial, tangential and axial direction contraction results appear to correlate with the mechanical properties for bone in the three orthogonal directions. We see the general pattern as the greatest change per length takes place radially (perpendicular to lamella), followed by tangentially and then axially. While the orientations of the canaliculi and the lacunae may partially contribute to the greater tangential contraction at 28% rh in

transverse sections, the main reason is predicted to be the presence of layers of more and less mineralized lamellae within the osteon.

The maximum change per length attained with dehydration (0.0197) is comparable to the ultimate tensile strain for longitudinally sectioned equine cortical bone (0.028-cranial, 0.016-caudal) [60]. As our experiments did not involve any external forces, we do not refer to dehydration induced change per length as "strain". The difference between contraction arising from dehydration and the ultimate tensile strain implies that much of the water, which can only be removed in vacuum is confined in such a way that the bone will break under load before this water component moves elsewhere. Therefore, this type of water is not likely to be within the vascular system or the canaliculi, but is more likely to be water intimately bound at the molecular level to the matrix and/or to the mineral surfaces of the lamellae.

4.1.1 Reduction in Collagen Fibril Equatorial Spacing

In globular proteins, water molecules can be bound to specific sites within the molecule: strongly bound to the surface of the molecule (first hydration shell) and less strongly bound at greater distances, as the water molecules grade into bulk water [80]. However, for type I collagen, this classification is less obvious; specific sites within the structure where water molecules are tightly bound are not known. Collagen, as a strongly hydrophilic molecule, normally existing in a swollen state, is thought to be structurally stabilized by water molecules existing interfibrillary. Intrafibrillary, collagen has been shown to interact with at least 1000 water molecules, arranged in alternating hydration shells of higher and lower density in computer simulations using Sterred Molecular Dynamics (SMD) [80]. Dehydration is assumed to remove the water molecules in the different hydration shells around the collagen fibrils and PGs, reduce the diameter of collagen fibrils, by forcing new H-bond formation between the various side groups. A decrease in collagen fibril equatorial spacing has been observed with dehydration [44]. When mineralized collagen is rewet, initially both the mineral and the collagen are rehydrated upto about 62% rh; above that, mainly the collagenous

matrix is rehydrated [45].

4.1.2 Implications with Regard to Water in the Lamellar Structure

The 3D stacking of stagger-arrayed collagen fibrils results in extended intrafibrillar grooves [43]. These grooves have a thickness of about 1.5 nm and extend along the length of the fibril axis for about 40 nm. Their widths depend on the 3-dimensional organization of the fibril, which, judging from the structure of mineralized collagen fibrils, could extend across the fibril diameter i.e. about 80 nm [43]. Water molecules present in the groove would be bound to the protein surfaces exposed in the grooves (analogous to the first hydration shell). Modeling of the water bound to the surface of the collagen triple helical molecule shows that it forms a layer with a thickness of about 0.4 nm [80, 32]. This implies that about half of the groove volume is filled with structural water. The crystals nucleate in the grooves and then continue to grow initially within the grooves and later extend between the layers of collagen triple helical molecules [81]. The fact that crystal growth continues and is not inhibited by the collagen, implies that the interface is not dominated by charged interactions. Based on the findings of Wilson et al. [33], a water layer exists on either side of the crystal filling the groove, which, when unmineralized, contained two more water molecules. Therefore, when the crystals grow, they only displace the water molecules located in the middle of the groove. In unmineralized collagen only the water molecules in the center of the groove would be removed by dehydration. Assuming this involves two water layers some 0.8 nm thick, the highest amount of contraction that would occur for a parallel array of triple helical molecules aligned in 3-dimensions to form a groove across the entire fibril would be about 10% (the groove constitutes a fifth of the volume and only the half of the groove that contains bulk water contracts) (Fig. 4.1). If all the groove volume was filled with mineral then no contraction upon dehydration would occur, as the structural water molecules between the collagen and the crystal surfaces remain. However, in the less mineralized part of a lamella not all the grooves can be filled with mineral. Wilson et al. [33] in fact performed their measurements under dehydrated conditions. Furthermore, following the rotated plywood model [42, 82] in

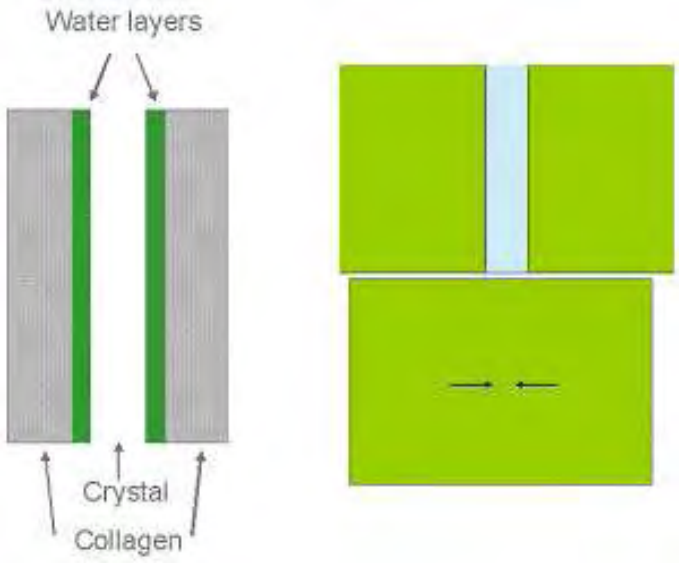

Figure 4.1 A graphic illustration of the arrangement of collagen water and crystal in the collagen fibril (left). The rearrangement of collagen and water due to dehydration in the absence of crystal in the less mineralized collagen fibril (right).

this half of the lamella most of the collagen fibrils have their grooves (inferred from the orientation of the crystal plane) more or less parallel to the lamellar boundary. Since the sublamellae oriented at 0 degree angle makes up one fifth of the lamellae, an average contraction of about 2% by calculation is expected (10% times 1/5). We thus suggest that the approximately 1 to 1.4% contraction upon dehydration observed in the longitudinal sections perpendicular to the lamellae, occurs mainly within the less mineralized region. Probably this region is also the site where contraction under load (strain) mainly occurs. In transverse sections, the lamellae also contract during dehydration in the direction parallel to the lamellar boundary. Although this may imply that the lamellar structure is not continuous along the lamella, we propose that parallel contraction in this direction is due to the differences in crystal/groove orientations. We do note however that in the BSE images, the darker and hence less mineralized portions are not continuous along the lamellae. The fact that this contraction does not occur when the osteons are disrupted in the longitudinal sections may imply that in this direction the crystal orientations may restrain contraction of the collagen fibrils as they do not contract independently.

4.1.3 Differences in Mineralization between Sublamellae

Based on our findings, we predicted that there are differences in the amount of mineralization between sublamellae. The difference between the longitudinal and the transverse sections is that in the longitudinal section the osteons are cut such that lamellae essentially form half cylinders, whereas in the transverse sections, the cylinders remain whole as shown in Fig. 4.2, where the arrows indicate the direction forces arising from dehydration are exerted. We therefore postulate for the longitudinal sections that the half cylinders could easily pack closer together by contraction perpendicular to the lamellae. This would occur if, as demonstrated, part of the structure responsive to drying was also arranged in layers parallel to the lamellae. On the other hand, in the transverse sections, the internal forces arising from dehydration would also induce the lamellae of the intact cylinders to come closer together. However, for this to happen, the lamellae would have to change dimension in the direction parallel to the lamellar boundaries.

The BSE images demonstrating the presence of more mineralized and less mineralized zones within a lamella are consistent with the nanoindentation results of Hengsberger et al. [83], which showed that the thicker lamellae have a higher elastic modulus than the thin lamellae. The presence of such differential mineralization of zones within an individual lamella, may be the key to reconciling two longstanding, seemingly contradictory views of the lamellar bone structure: densely packed fibers (thick lamellae) alternating with diffusely packed fibers (thin lamellae), as opposed to sub-lamellae consisting of different collagen fibril orientations with varying degrees of mineralization [41, 42, 82].

The less densely packed fibril zone appears to correspond to the less mineralized zone. In addition, as in this zone the fibrils are more or less in the plane of the section, both of these factors would make them more prone to pulling out during polishing and hence appearing less organized. It is conceivable that the imaged stripes could be ascribed to the different orientations of the mineralized collagen fibrils within a lamellae [42] intersecting with the observed surface, and thus revealing more or less

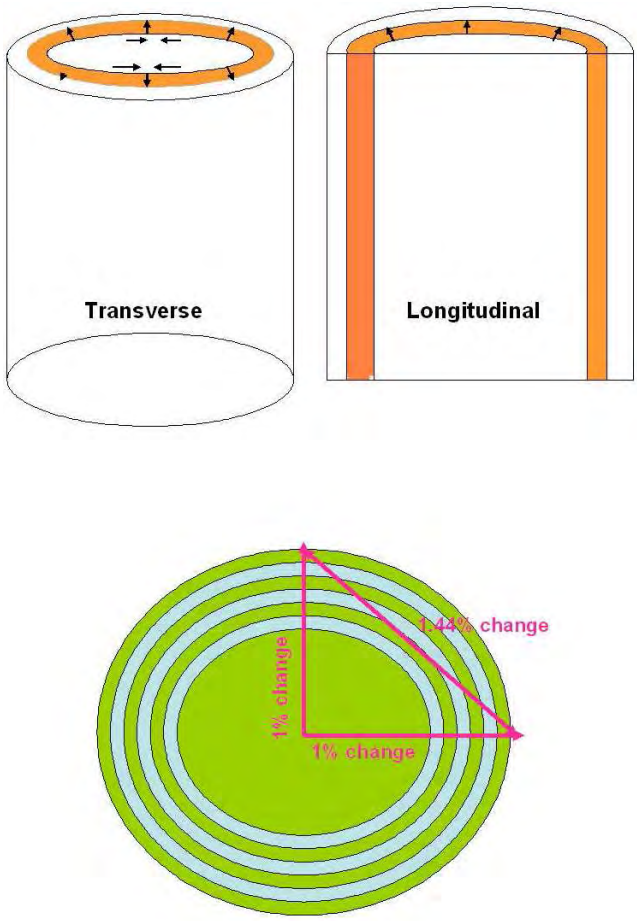

Figure 4.2 Schematic showing the longitudinally and transversely cut osteons. In the transversely sectioned osteon radial and tangential, in the longitudinally sectioned bone radial and axial contraction are visualized. The direction of forces exerted by dehydration are shown as small arrows (above). Expected percent change in length in a unit circle representing the osteon (below).

collagen relative to mineral at the surface. This is however unlikely as the mineral and collagen alternate at length scales of a few nanometers and the depth from which the signal is collected, especially in the deep penetrating BSE detector image, is from a depth of about 1 micrometer. We therefore conclude that these changes in contrast are due to different mineral densities.

These differences in mineralization of the sublamellae, with greater contraction of the less mineralized lamellae than the mineralized, leads to a high standard deviation per measured segment. As the mechanical properties of demineralized and mineralized bone [12] show that the mineralized lamellae do not contract as much as the less mineralized lamellae, it can be concluded using basic geometry that for a segment of given

length, contraction will increase with the number and thickness of less mineralized lamellae included in that segment. This also explains the difference between the calculated and observed tangential contraction in transverse sections. In a unit circle, a radial contraction of 1% would lead to a 45 degree tangential contraction of 1.44%, which is higher than the observed contraction (1.1%) at 42% rh. This difference is also due to the number, length and thickness of more mineralized sections included in the measurement.

The ESEM results on osteonal equine bone have implications on osteonal bone mechanics. Bone fluid, in addition to collagen scaffold and mineral, appears to be the third factor to affect bone mechanical properties, acting as a lubricant, a hydrant and providing hydraulic support within the osteonal system. While the less mineralized sublamellae may lead to a reduction in compressive strength, yet an increase in toughness and bending safety factor [69]. The less stiff cement lines allowing movement of the relatively stiffer osteons may again enhance the viscoelastic properties of osteonal bone [68]. Our cement line findings indicate that the more calcified, brittle cement line [48] may allow easier separation of the interstitial lamellae from the Haversian system, again enhancing ductility.

4.2 Mechanical Properties of Bone

This study shows that bone microstructure has important ramifications on the mechanical properties of bone. Using a recent optomechanical technique, we have shown both the anisotropy in the mechanical properties of bone and the strain distribution across the surface of bone, generated as a result of the anisotropic nanostructural organization in bone. Our results show that the mechanical properties of cortical bones vary with remodelling, which increases the anisotropy in mechanical properties with the loss of a pronounced degree of stiffness in the radial direction, probably in favor of a more feasible hydration and maintenance system for the organism, enhancing toughness.

4.2.1 Circumferential Lamellar Bone and Osteonal Bone

The optomechanical testing method has enabled the study of minute samples containing various microstructures, i.e. circumferential lamellar bone adjacent to osteonal bone, making the detailed study of their mechanical properties possible, which would not be determined in a classic compression test. Among the bones tested, using the criteria stated in the Section 3.2.4.3, we chose several radially compressed bones with reliable data to study the differences in the mechanical properties of circumferential lamellar bone and osteonal bone, using three different methods: the Y(j)-linearity, the linear region of the stress-strain curve and linear regression. These results show that the mechanical properties of proximo-anterior minipig tibial cortical bones, containing both circumferential lamellar and osteonal lamellar bone sections, display intermediate values of E_1 of 7.9 $\pm$ 2.1 GPa, while the primary circumferential lamellar bone displayed an E_1 of 9.4 $\pm$ 2.0 GPa compared with the E_1 of 6.8 $\pm$ 0.8 GPa for the secondary osteonal bone. The strain values in the circumferential lamellar section varied between $0.1\text{x}10^{-4}$ and $1.5\text{x}10^{-4}$, while osteonal section displayed strain values between $0.5\text{x}10^{-4}$ and $2.5\text{x}10^{-4}$.

The linear regression method has enabled us to obtain strain and elastic modulus distributions for the whole surfaces of bone samples. The data from the radially compressed bones and from the bones tested in three orthogonal directions, B1 and B2, (Table 3.11) were analyzed using the linear regression method, which, using filtering techniques, gave insight into the differences in mechanical properties of circumferential lamellar and osteonal bones. The regions with higher elastic moduli were correlated with the microstructure in the radially compressed bones, showing that the elastic moduli of the periosteal region were higher than that of the endosteal region in the partially osteonal bones. The elastic modulus distribution for the periost up and periost down bones were compared to show that the periosteal section with the circumferential lamellar bone had a higher modulus, which was shown to be true for the bones tested with the periostal side down (Figs. 3.18 and A.2). Although the elastic moduli for the circumferential lamellar bone, estimated using the linear regression analysis, were higher (in the range of 20 - 50 GPa) than those obtained by the Y(j)-linearity method

(Table 3.10). In these figures the elastic moduli for osteonal section of the bone remain close to the values obtained from both the Y(j)-linearity method and the linear region of the stress-strain curve. We think that such high modulus values in the in the radially compressed bones are due to the size of the 20 x 20 pixel frame we have used, which was a compromise between getting accurate local values and a reduced signal-to-noise ratio. The elastic modulus results of the transversely compressed partially osteonal bone samples, B1 and B2, (Fig. 3.20 and 3.21) obtained by linear regression analysis, also indicate that the circumferential lamellar region displays a higher modulus than the osteonal lamellar region; whereas such a variation in elastic modulus and strains does not exist in the completely osteonal control bone samples (Figs. 3.10 and 3.11).

4.2.2 Elastic Moduli and Poisson's Ratios

The results obtained using the stress-strain curve and two-point linear regression analysis show that the samples with more reliable data, containing both circumferential lamellar and osteonal lamellar bone sections, have E_1 of 7.9 $\pm$ 2.1 GPa and ν_{12} of 0.3. Our elastic modulus results comply quite well with Crenshaw et al.'s, who have also studied minipig bones. We may assume that their samples were partially osteonal (although such an information has not been presented by the authors) as our completely osteonal control bone elastic modulus results are lower than their findings. It is rather difficult to compare our findings, listed in Tables 3.6, 3.9 and 3.11 , with the findings of other researchers as there are very few studies on the mechanical properties of pig and minipig bones with information on the microstructure of the samples. Since the aim of this study was to compare mechanical values and microstructure, we have placed great importance to microstructure of the samples, while other researchers listed in Tables 3.6 and 3.11 have not specified the extent of bone remodelling in their bone samples. To the best of our knowledge, only Crenshaw et al. [79] and Vidal et al.[78] have studied the compression moduli of various pig and minipig bones in the radial direction using classical mechanical testing methods. Therefore, due to scarcity of data on pig/minipig bones and the taxonomical proximity of swine and bovine, we have compared our results on miniature swine with bovine osteonal bone as well, since

taxonomically cows and pigs are from the order of artiodactyla, even toed-ungulates (cattle, sheep, goats, deer, buffalo, etc.), yet from different suborders (pigs are from Suiformes; whereas, cows are from Ruminantia). Mechanical properties of bones tested in three orthogonal directions indicate that our samples were not transversely isotropic because the compression elastic moduli display 50 - 100% difference. The moduli of partially osteonal bone, B1, which contains about 20% CLB and 80% OB, compare well with those of Ashman et al., who have tested the bones using ultrasound, and Reilly and Burstein. Despite the difficulties in making comparisons between samples which might have different microstructures, our values lie within the range of other researchers' results. We have obtained Poisson's ratios that are close to those of Ashman et al.

4.2.3 Remodelling and Osteonal Bone Design

The shape and material content of bone also varies with the force pattern placed on the tissue, whether the force remains in one plane or not. Force generates strain that varies in magnitude, frequency and orientation. Bones adapt to strain at three levels: structurally, transductionally and by design. It is thought that bones adapt to strain macrostructurally by modelling its size and shape, depositing new bone, or by remodelling, resorbing and depositing new bone, and microstructurally by organization of its collagen and mineral orientation and density and lamellar organization [84]. For example, compressive strength in bone is increased by the closely packed crystals with a high elastic modulus, while tensile strength is achieved by collagen, which has not only a high energy storage capacity but also a maximum damping capacity for vibrations in the frequency range of nerves which stimulate muscle contraction. To increase its strength, bone changes its material properties by increasing its compressive strength with increased crystallization and increasing its tensile strength by increasing the number of fibers in that direction as well as orientation of osteons and trabeculae [85]. Transductional adaptation involves cellular responses by either detecting strain through the nerves in the periosteum or through the fluid - filled canaliculi and the piezoelectric potentials generated by collagen and mineral deformation. Bone tissue is then designed considering conservation of mass and attainment of certain structural

properties and growth to specific dimensions. Bone design involves the safety factor, i.e. strength in excess of expected load, or the feasibility of having a stronger bone with the cost of extra material versus the cost of having more additional mass during movement.

Osteonal bone may demonstrate the advanced biological design to meet functional requirements under the constraint of microstructural (modelling/remodelling of bone tissue) and biomechanical concerns (attachment of muscles, connective tissues). Bone tissue varies in composition to embody different mechanical properties in different locations in the organism as the main concern is that of adaptation of structural design to meet functional requirements in a mechanically viable solution. As force generates strain that varies locally in magnitude, frequency and orientation, an osteonal design may enable a more feasible distribution of stress under mass and space restraining conditions. To maximize resistance to stress, bone may change its material properties by increasing mineralization, as well as changing the orientation of osteons. The shape and material content of osteonal bone increases the bending strength of bone, its safety factor, i.e. strength in excess of expected load and maintains the integrity of bone during the changes that take place as part of macrostructural adaptation mechanisms (resorption of microcracks) [86]. Osteonal bone may offer a feasible design with a lower elastic modulus and less mass, e.g. in the lower parts of the body where fast movement may be crucial for survival of highly mobile organisms [86, 85, 84].

5. CONCLUSIONS

The water component of the lamellar structure clearly fulfills important structural and mechanical functions. Dehydration of osteonal bone results in contractions that are almost as high as those that occur during tensile loading just prior to failure. About half of an individual lamella is less mineralized than the other half, and hence must have a higher proportion of grooves/channels within the collagen fibrils that are not filled by crystals. We suggest that it is the removal of the water from these grooves that accounts for much of the observed contraction. Bone microstructure has important ramifications on the mechanical properties of bone. The anisotropy in the mechanical properties of bone has been revalidated in this study using optomechanics. In addition, the strain distribution across the surface of bone, generated as a result of the anisotropic nanostructural organization in bone, has been shown to vary with remodelling, which results in a pronounced decrease in stiffness in the radial direction; yet, without a reduction in the axial direction. Remodelling in bone may be a mechanism to introduce a more feasible hydration and maintenance system for the organism, enhancing toughness.

APPENDIX A. STRAIN AND ELASTIC MODULUS DISTRIBUTION IN PARTIALLY OSTEONAL BONES

A.1 Sample B4 PU

Fig. A.1 shows the x-, xy- and y-strain distribution for the whole surface and the y-strain distribution profile, the microscopic image and the [3x3] median filtered elastic modulus distribution profile. X-normal strain distribution varies between -2x10^{-5} and 8x10^{-5}; xy-shear strain distribution varies between -1x10^{-4} and 2.5x10^{-4}; while, the y-normal strain distribution varies between 0.5x10^{-4} and 2.5x10^{-4} in the osteonal section and between 0.5x10^{-4} and 1.5x10^{-4} in the circumferential lamellar section of the sample. The elastic modulus varies between 5-10 GPa in the osteonal section and 8-14 GPa in the circumferential lamellar section of the bone.

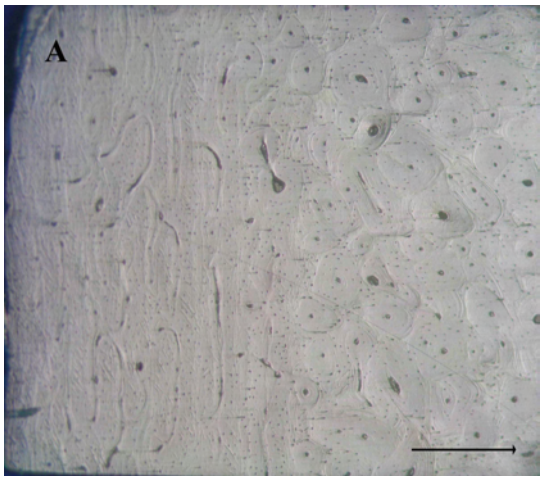

Figure A.1 Strain and elastic modulus distributions for the radially compressed partially osteonal bone sample B4 PU. Images are oriented such that the bone sample appears to have been loaded from left to right. In the following images, periosteum is to the left and endosteum is to the right. For images B-D, colorbars indicate strain and the unit of length for the abscissa and ordinate is pixel number, where the pixel length is approximately 12 micrometers. (A) The micrograph of sample B4 PU (scale bar, 300 micrometers); (B) X-strain distribution across the surface of the bone, obtained from X-displacement data, u(i,j); (C) xy-shear strain distribution across the surface of the bone, obtained from X and Y-displacement data; (D) Y-strain distribution across the surface of bone, obtained from Y-displacement data, v(i,j). For images E-F, the unit of length for the abscissa is pixel number, where the pixel length is approximately 12 micrometers. (E) Y-strain distribution profile, the ordinate indicates strain. (F) Elastic modulus distribution profile obtained from strain distribution data. The ordinate indicates elastic modulus in GPa.

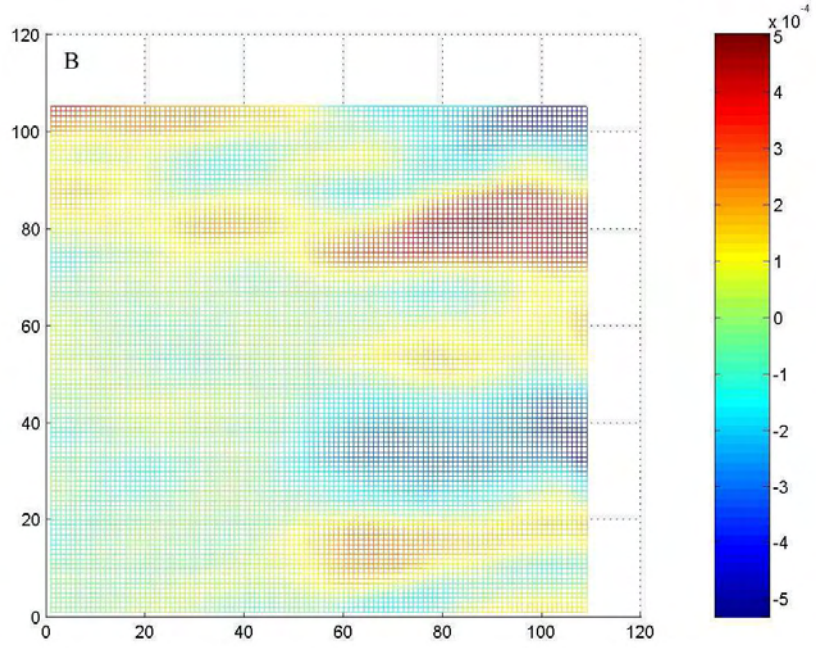
B
x 10^-4
5
4
3
2
1
0
-1
-2
-3
-4
-5
0
20
40
60
80
100
120

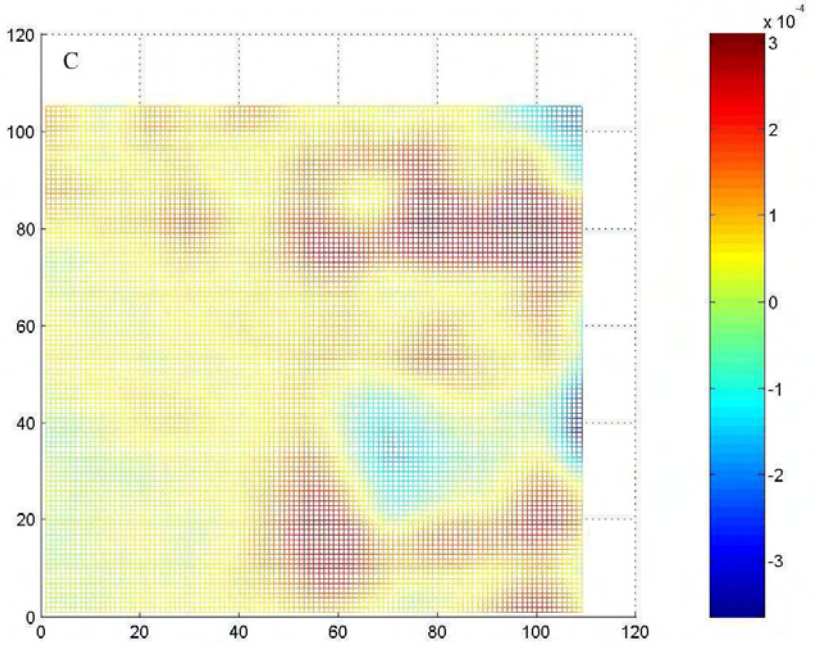
C
x 10^-4
3
2
1
0
-1
-2
-3
0
20
40
60
80
100
120

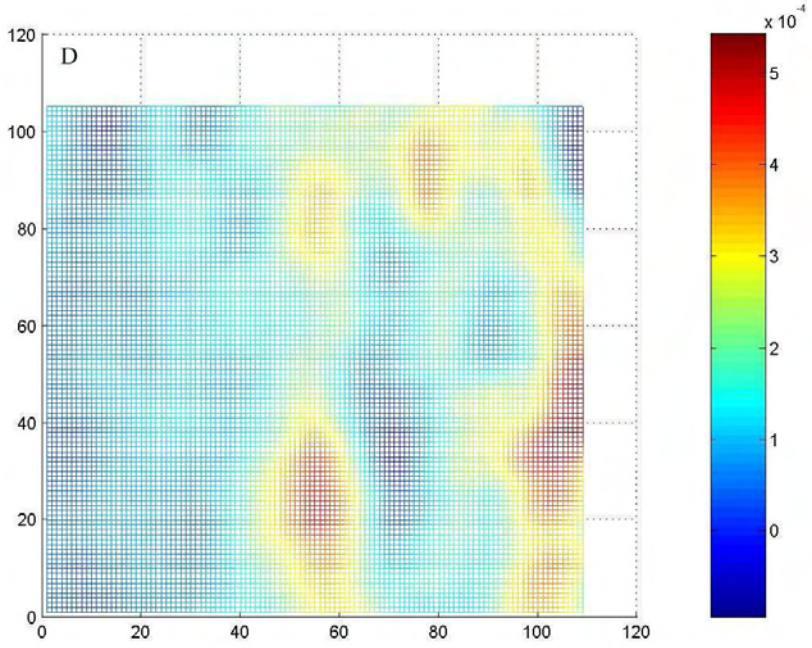
D
x 10^-4
120
100
80
60
40
20
0
0
20
40
60
80
100
120
5
4
3
2
1
0

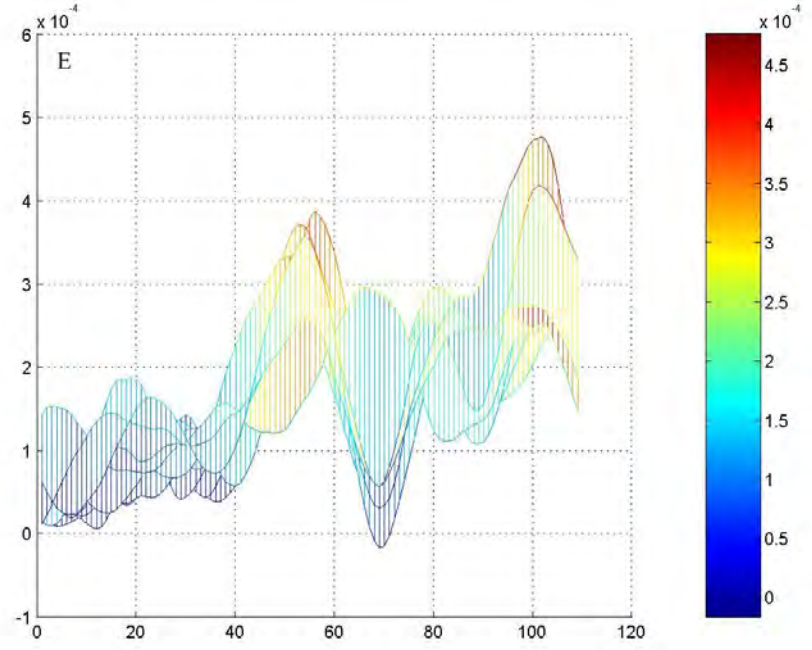
E
x 10^-4
x 10^-4
6
5
4
3
2
1
0
-1
0
20
40
60
80
100
120
4.5
4
3.5
3
2.5
2
1.5
1
0.5
0

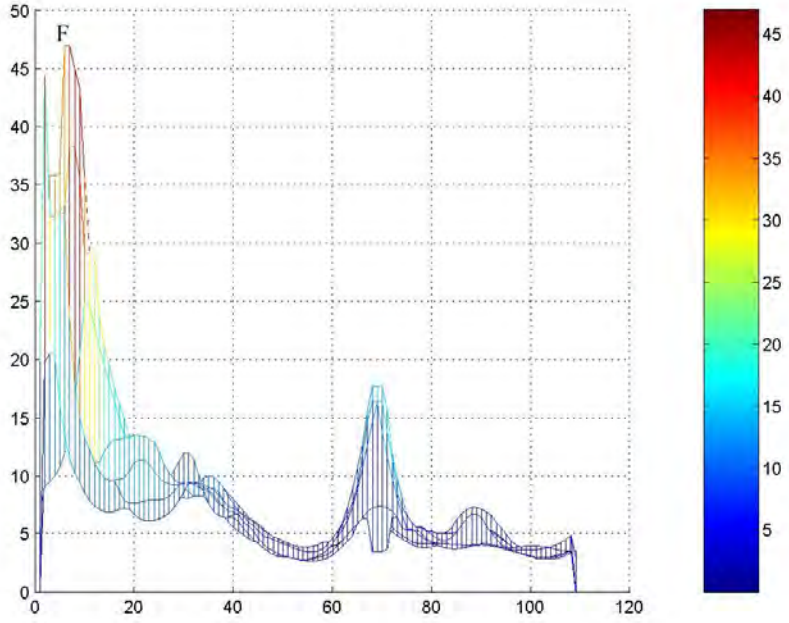
F
50
45
40
35
30
25
20
15
10
5
0
0
20
40
60
80
100
120
45
40
35
30
25
20
15
10
5

A.2 Sample B5 PD

Fig. A.2 shows the x-, xy- and y-strain distribution for the whole surface and the y-strain distribution profile, the microscopic image and the [5x5] median filtered elastic modulus distribution profile. X-normal strain distribution varies between -1.5x10^{-4} and 2x10^{-4}; xy-shear strain distribution varies between -4x10^{-5} and 14x10^{-5}; while, the y-strain distribution varies between 0.2x10^{-4} and 2.2x10^{-4} in the osteonal section and between 0 and 1.5x10^{-4} in the circumferential lamellar section of the sample. The elastic modulus varies between 5-8 GPa in the osteonal section and 8-13 GPa in the circumferential lamellar section.

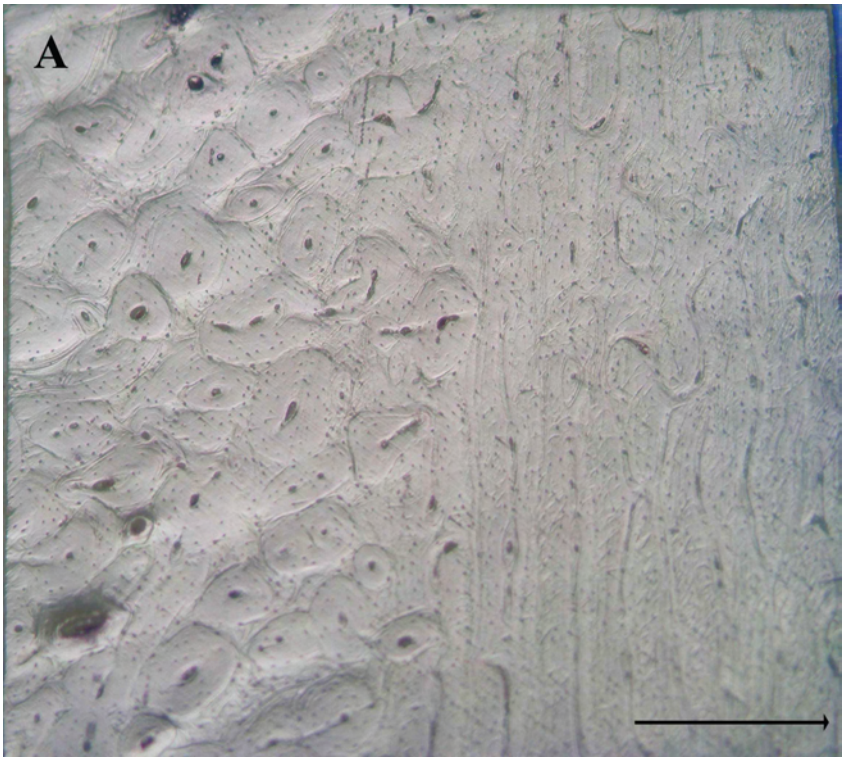

Figure A.2 Strain and elastic modulus distributions for the radially compressed partially osteonal bone sample B5 PD. Images are oriented such that the bone sample appears to have been loaded from left to right. In the following images, periosteum is to the right and endosteum is to the left. For images B-D, colorbars indicate strain and the unit of length for the abscissa and ordinate is pixel number, where the pixel length is approximately 12 micrometers. (A) The micrograph of sample B5 PD (scale bar, 300 micrometers); (B) X-strain distribution across the surface of the bone, obtained from X-displacement data, u(i,j); (C) xy-shear strain distribution across the surface of the bone, obtained from X and Y-displacement data; (D) Y-strain distribution across the surface of bone, obtained from Y-displacement data, v(i,j). For images E-F, the unit of length for the abscissa is pixel number, where the pixel length is approximately 12 micrometers. (E) Y-strain distribution profile, the ordinate indicates strain. (F) Elastic modulus distribution profile obtained from strain distribution data. The ordinate indicates elastic modulus in GPa.

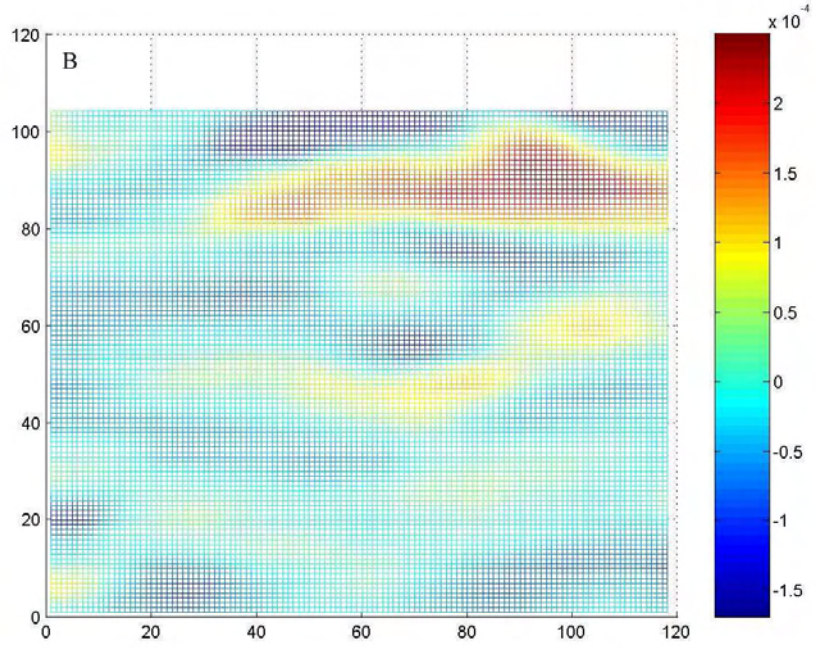
B
x 10^-4
2
1.5
1
0.5
0
-0.5
-1
-1.5
120
100
80
60
40
20
0
0
20
40
60
80
100
120

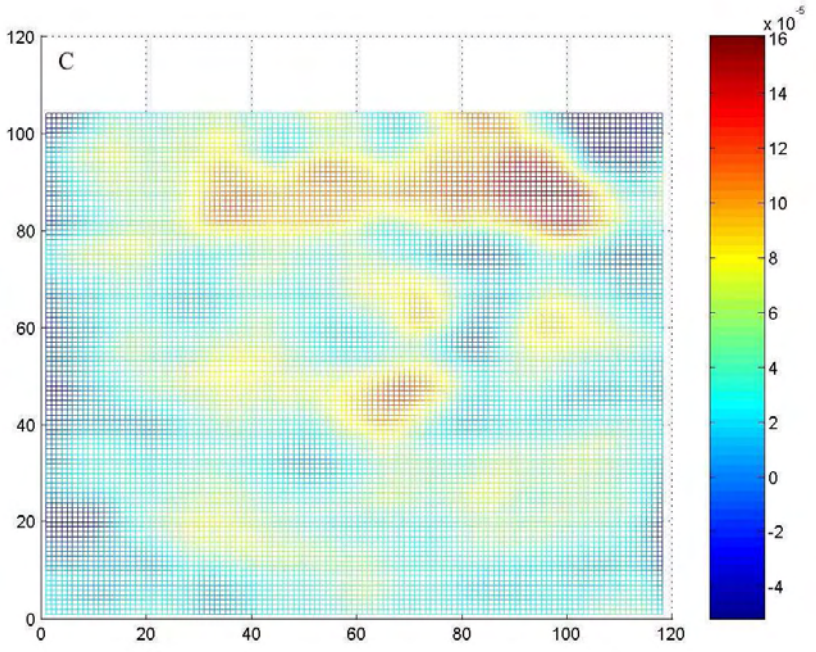
C
x 10^-5
16
14
12
10
8
6
4
2
0
-2
-4
120
100
80
60
40
20
0
0
20
40
60
80
100
120

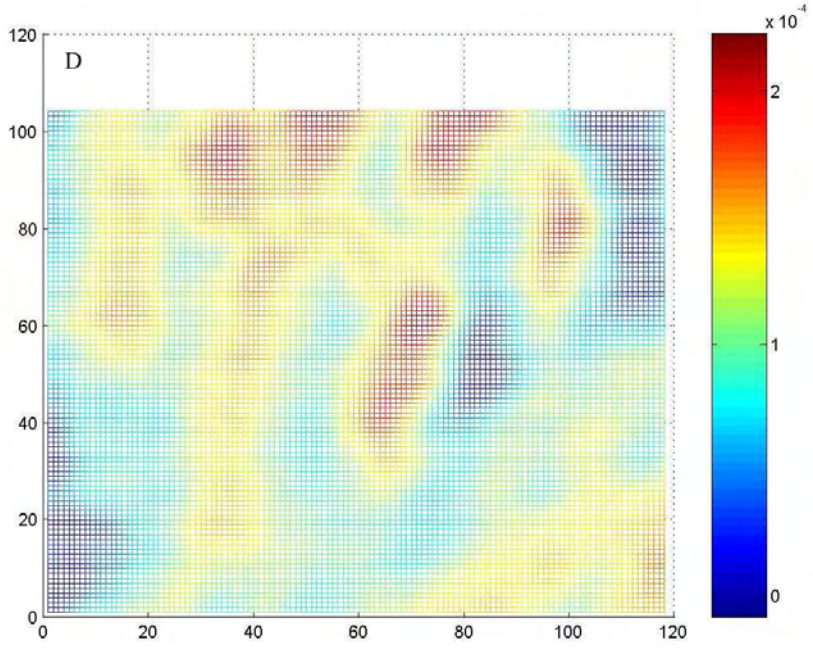
D
x 10^-4
2
1
0
120
100
80
60
40
20
0
0
20
40
60
80
100
120

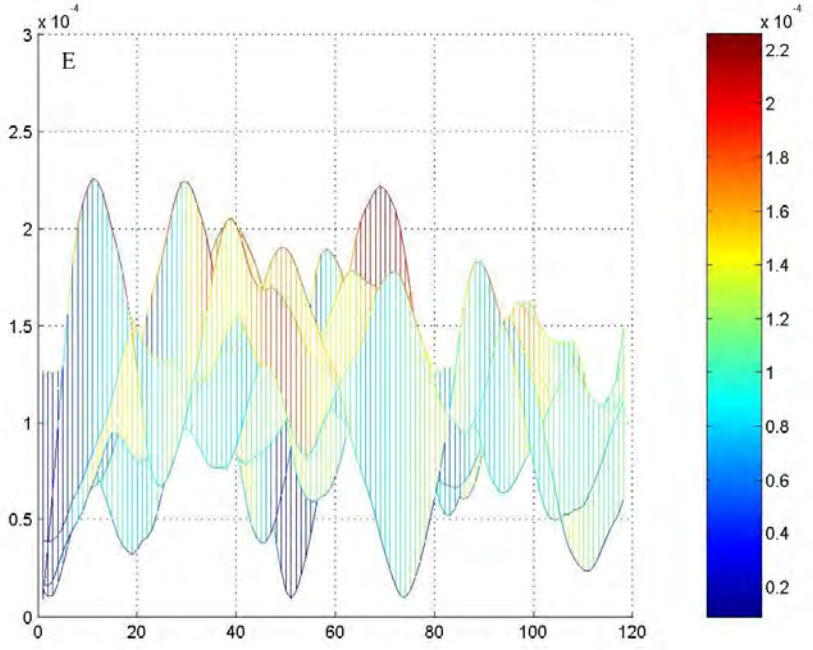
E
x 10^-4
3
2.5
2
1.5
1
0.5
0
0
20
40
60
80
100
120
x 10^-4
2.2
2
1.8
1.6
1.4
1.2
1
0.8
0.6
0.4
0.2

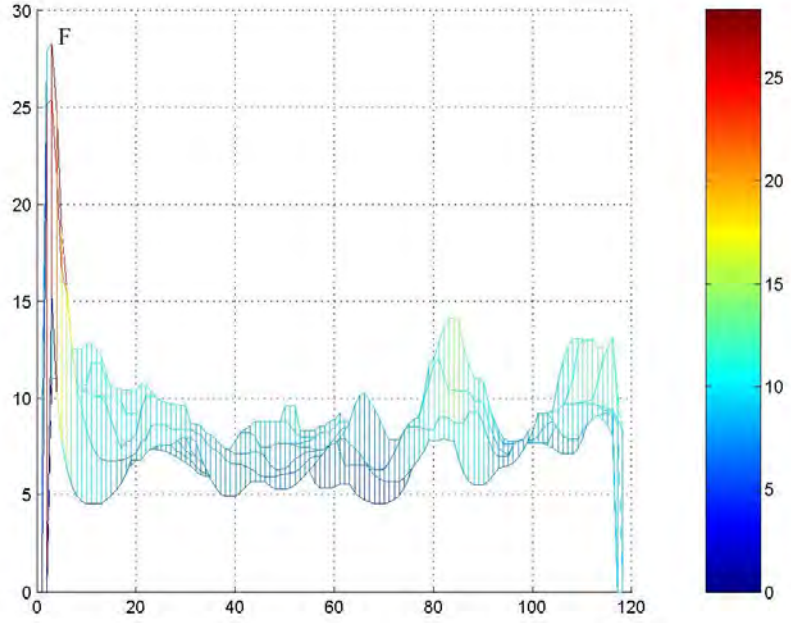
F
30
25
20
15
10
5
0
0
20
40
60
80
100
120
25
20
15
10
5
0

A.3 Sample B8 PD

Fig. A.3 shows the x-, xy- and y-strain distribution for the whole surface and the y-strain distribution profile, the microscopic image and the [3x3] median filtered elastic modulus distribution profile. X-normal strain distribution varies between -4x10^{-5} and 10x10^{-5}; xy-shear strain distribution varies between -1x10^{-4} and 1x10^{-4}; while, the y-strain distribution varies between 0.5x10^{-4} and 2.5x10^{-4} in the osteonal section and between 1.0x10^{-4} and 2.5x10^{-4} in the circumferential lamellar section of the sample. The elastic modulus varies between 5-15 GPa in the osteonal section and 5-20 GPa in the circumferential lamellar section. When the results for B8 PD are correlated with the microstructure, the effect of the presence of several holes in the circumferential can be clearly seen.

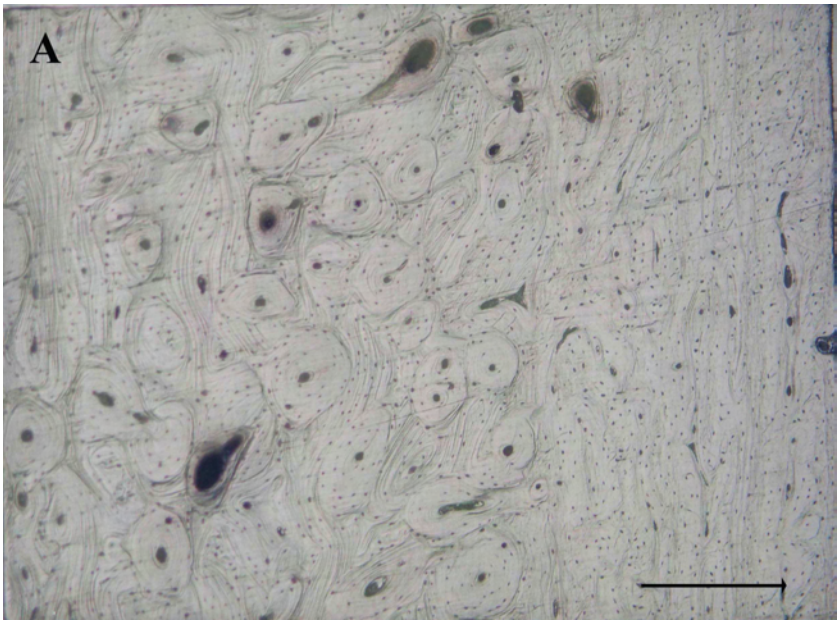

Figure A.3 Strain and elastic modulus distributions for the radially compressed partially osteonal bone sample B8 PD. Images are oriented such that the bone sample appears to have been loaded from left to right. In the following images, periosteum is to the right and endosteum is to the left. For images B-D, colorbars indicate strain and the unit of length for the abscissa and ordinate is pixel number, where the pixel length is approximately 12 micrometers. (A) The micrograph of sample B8 PD (scale bar, 300 micrometers); (B) X-strain distribution across the surface of the bone, obtained from X-displacement data, u(i,j); (C) xy-shear strain distribution across the surface of the bone, obtained from X and Y-displacement data; (D) Y-strain distribution across the surface of bone, obtained from Y-displacement data, v(i,j). For images E-F, the unit of length for the abscissa is pixel number, where the pixel length is approximately 12 micrometers. (E) Y-strain distribution profile, the ordinate indicates strain. (F) Elastic modulus distribution profile obtained from strain distribution data. The ordinate indicates elastic modulus in GPa.

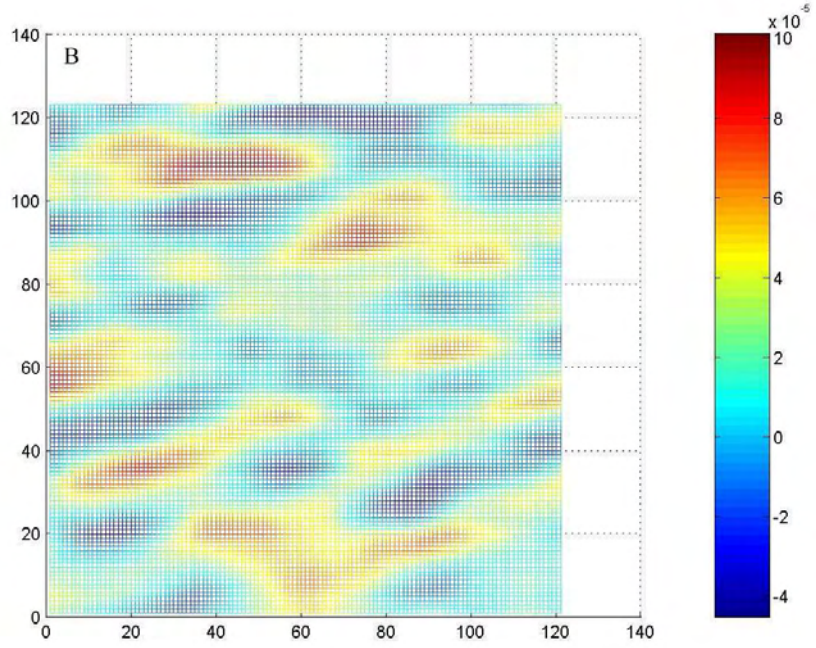
B
x 10^-5
10
8
6
4
2
0
-2
-4
140
120
100
80
60
40
20
0
0
20
40
60
80
100
120
140

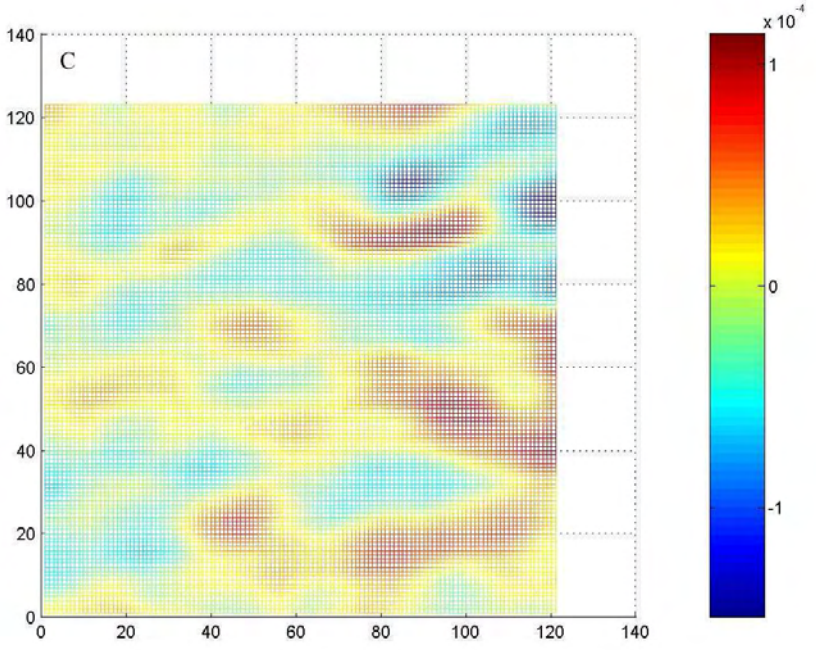
C
x 10^-4
1
0
-1
140
120
100
80
60
40
20
0
0
20
40
60
80
100
120
140

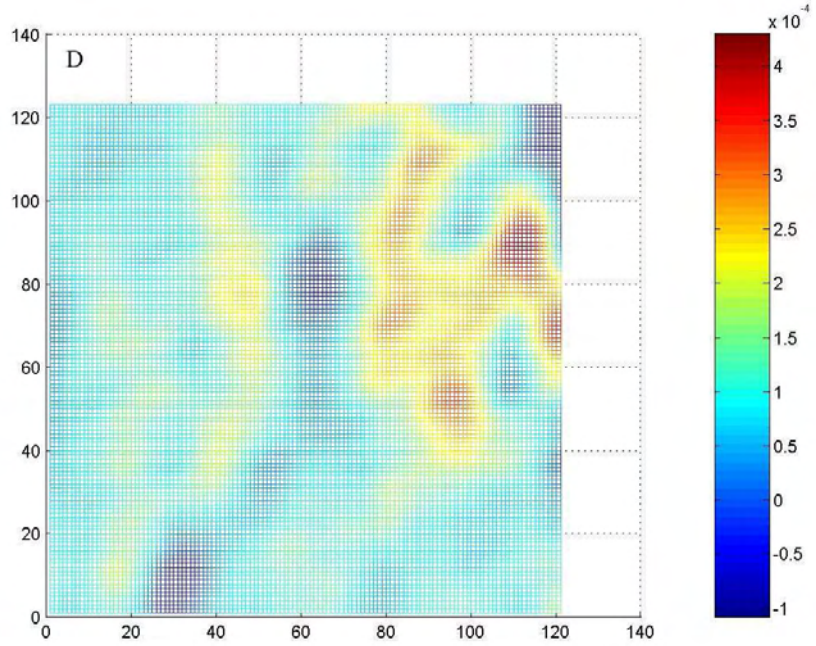
D
x 10^-4
4
3.5
3
2.5
2
1.5
1
0.5
0
-0.5
-1
140
120
100
80
60
40
20
0
0
20
40
60
80
100
120
140

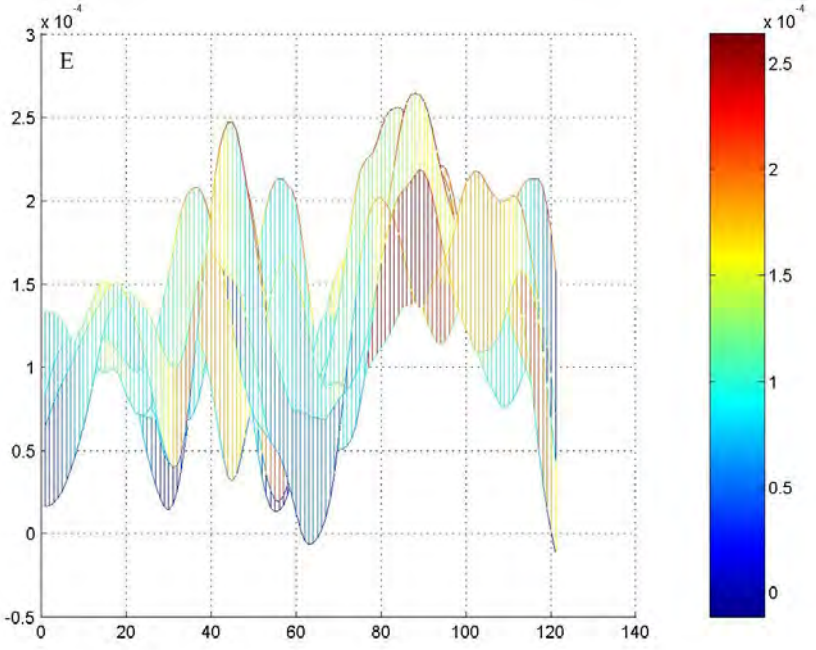
E
x 10^-4
3
2.5
2
1.5
1
0.5
0
-0.5
0
20
40
60
80
100
120
140
x 10^-4
2.5
2
1.5
1
0.5
0

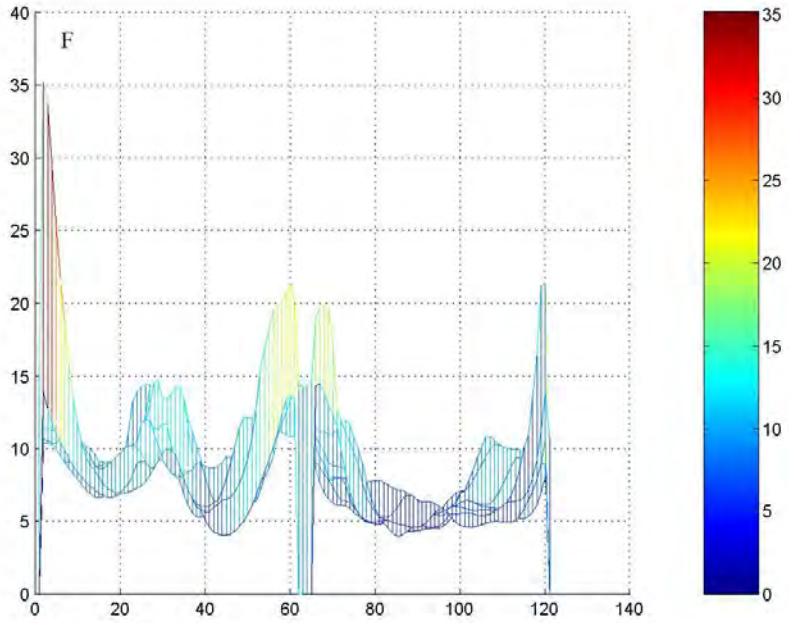
F
40
35
30
25
20
15
10
5
0
0
20
40
60
80
100
120
140
35
30
25
20
15
10
5
0

A.4 Sample B14 PD

Fig. A.4 shows the x-, xy- and y-strain distribution for the whole surface and the y-strain distribution profile, the microscopic image and the [3x3] median filtered elastic modulus distribution profile. X-normal strain distribution varies between -4x10^{-5} and 12x10^{-5}; xy-shear strain distribution varies between -6x10^{-5} and 6x10^{-5}; while, the y-strain distribution varies between 1.5x10^{-4} and 2.7x10^{-4} in the osteonal section and between 0.1x10^{-4} and 1.5x10^{-4} in the circumferential lamellar section of the sample. The elastic modulus varies between 5-8 GPa in the osteonal section and 5-20 GPa in the circumferential lamellar section.

Figure A.4 Strain and elastic modulus distributions for the radially compressed partially osteonal bone sample B14 PD. Images are oriented such that the bone sample appears to have been loaded from left to right. In the following images, periosteum is to the right and endosteum is to the left. For images B-D, colorbars indicate strain and the unit of length for the abscissa and ordinate is pixel number, where the pixel length is approximately 12 micrometers. (A) The micrograph of sample B14 PD (scale bar, 300 micrometers); (B) X-strain distribution across the surface of the bone, obtained from X-displacement data, u(i,j); (C) xy-shear strain distribution across the surface of the bone, obtained from X and Y-displacement data; (D) Y-strain distribution across the surface of bone, obtained from Y-displacement data, v(i,j). For images E-F, the unit of length for the abscissa is pixel number, where the pixel length is approximately 12 micrometers. (E) Y-strain distribution profile, the ordinate indicates strain. (F) Elastic modulus distribution profile obtained from strain distribution data. The ordinate indicates elastic modulus in GPa.

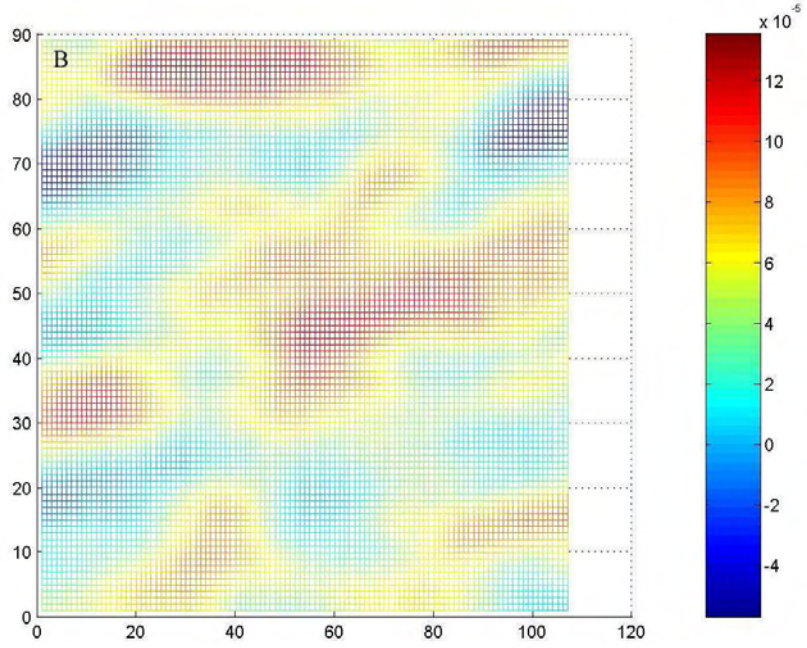
B
x 10^-5
12
10
8
6
4
2
0
-2
-4
0
10
20
30
40
50
60
70
80
90
0
20
40
60
80
100
120

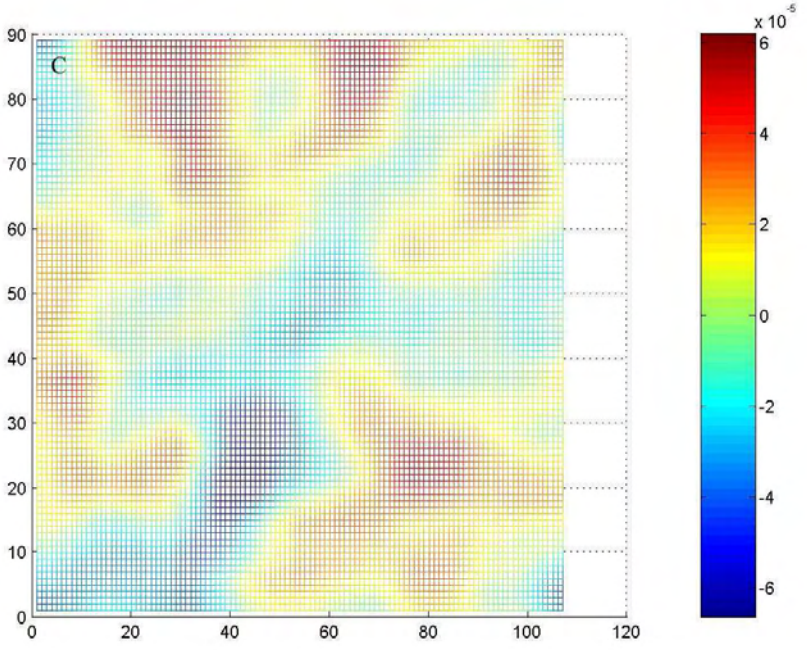
C
x 10^-5
6
4
2
0
-2
-4
-6
0
10
20
30
40
50
60
70
80
90
0
20
40
60
80
100
120

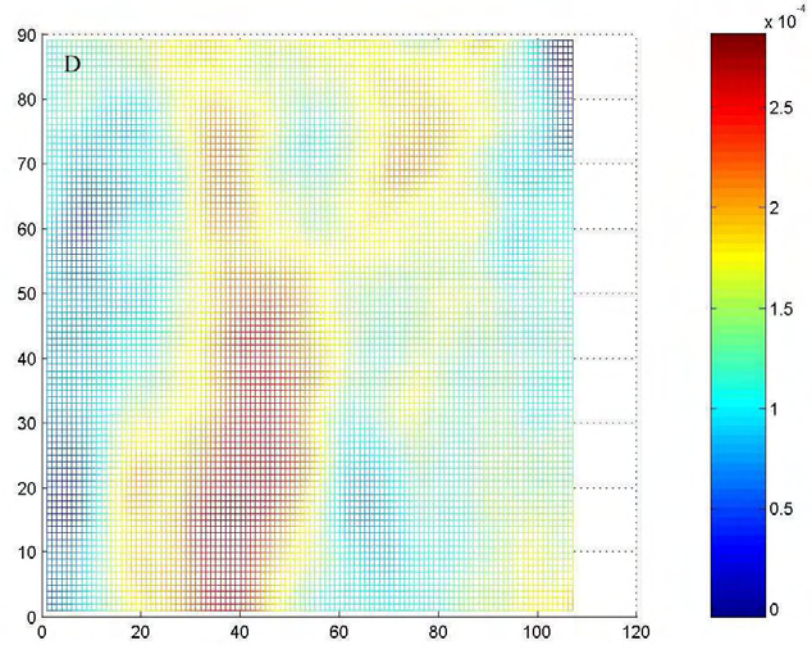
D
x 10^-4
2.5
2
1.5
1
0.5
0
90
80
70
60
50
40
30
20
10
0
0
20
40
60
80
100
120

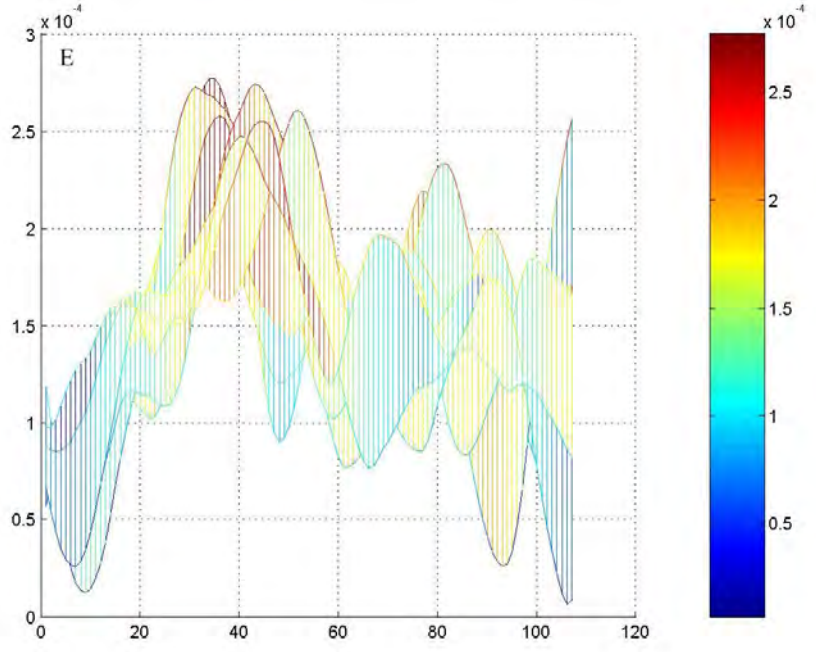
E
x 10^-4
3
2.5
2
1.5
1
0.5
0
0
20
40
60
80
100
120

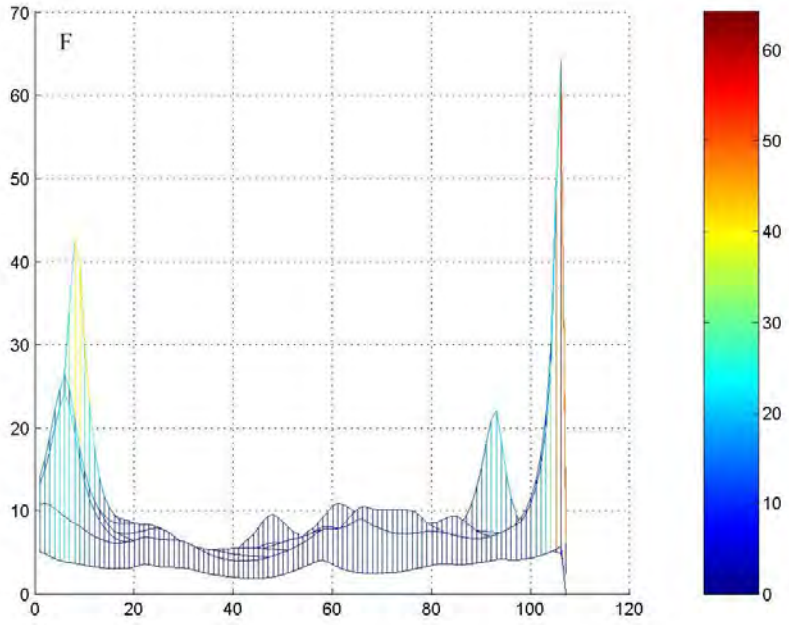
F
70
60
50
40
30
20
10
0
0
20
40
60
80
100
120
60
50
40
30
20
10
0

A.5 Sample B20 PD

Fig. A.5 shows the x-, xy- and y-strain distribution for the whole surface and the y-strain distribution profile, the microscopic image and the [3x3] median filtered elastic modulus distribution profile. X-normal strain distribution varies between -2x10^{-5} and 10x10^{-5}; xy-shear strain distribution varies between -0.5x10^{-4} and 2.5x10^{-4}; while, the y-strain distribution varies between 0.5x10^{-4} and 2x10^{-4} in the osteonal section and between 0.1x10^{-4} and 1.25x10^{-4} in the circumferential lamellar section of the sample. The elastic modulus varies between 5-12 GPa in the osteonal section and 10-20 GPa in the circumferential lamellar section.

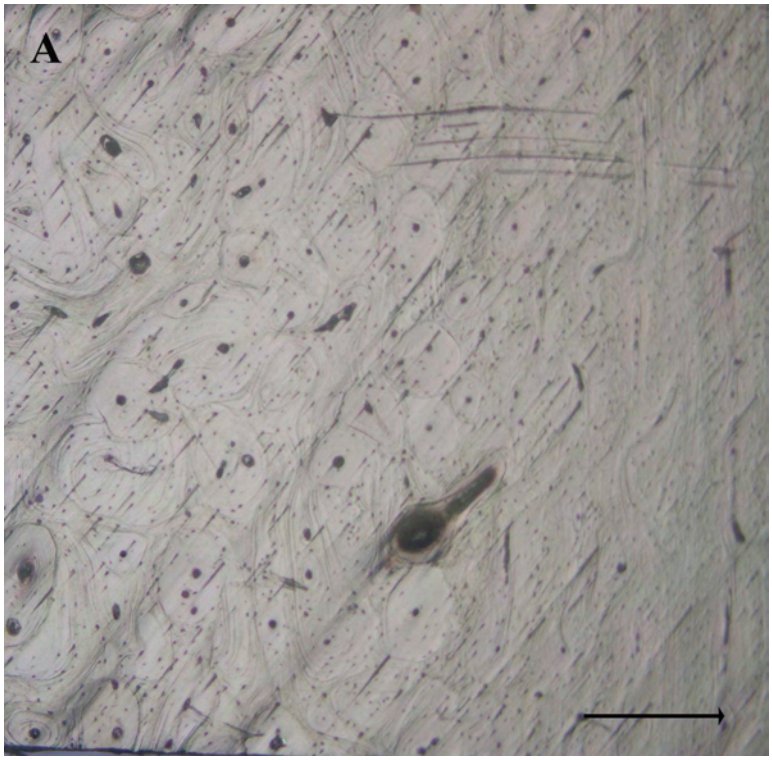

Figure A.5 Strain and elastic modulus distributions for the radially compressed partially osteonal bone sample B20 PD. Images are oriented such that the bone sample appears to have been loaded from left to right. In the following images, periosteum is to the right and endosteum is to the left. For images B-D, colorbars indicate strain and the unit of length for the abscissa and ordinate is pixel number, where the pixel length is approximately 12 micrometers. (A) The micrograph of sample B20 PD (scale bar, 300 micrometers); (B) x-strain distribution across the surface of the bone, obtained from X-displacement data, u(i,j); (C) xy-shear strain distribution across the surface of the bone, obtained from X and Y-displacement data; (D) y-strain distribution across the surface of bone, obtained from Y-displacement data, v(i,j). For images E-F, the unit of length for the abscissa is pixel number, where the pixel length is approximately 12 micrometers. (E) Y-strain distribution profile, the ordinate indicates strain. (F) Elastic modulus distribution profile obtained from strain distribution data. The ordinate indicates elastic modulus in GPa.

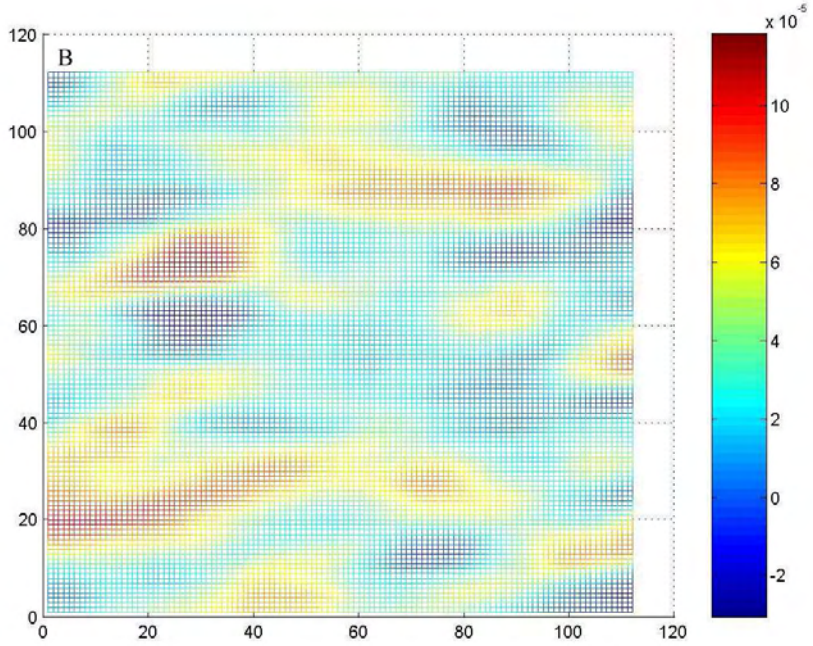
B
x 10^-5
10
8
6
4
2
0
-2
120
100
80
60
40
20
0
0
20
40
60
80
100
120

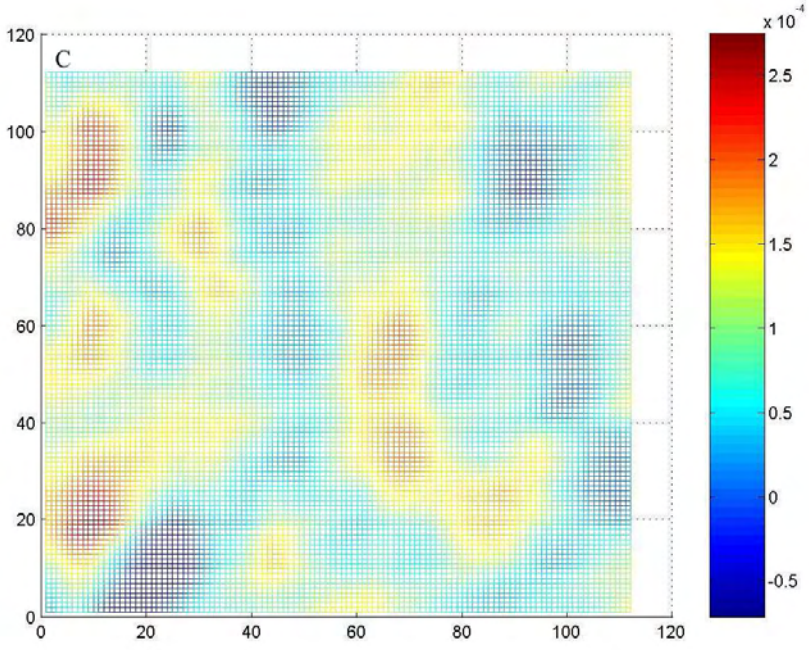
C
x 10^-4
2.5
2
1.5
1
0.5
0
-0.5
120
100
80
60
40
20
0
0
20
40
60
80
100
120

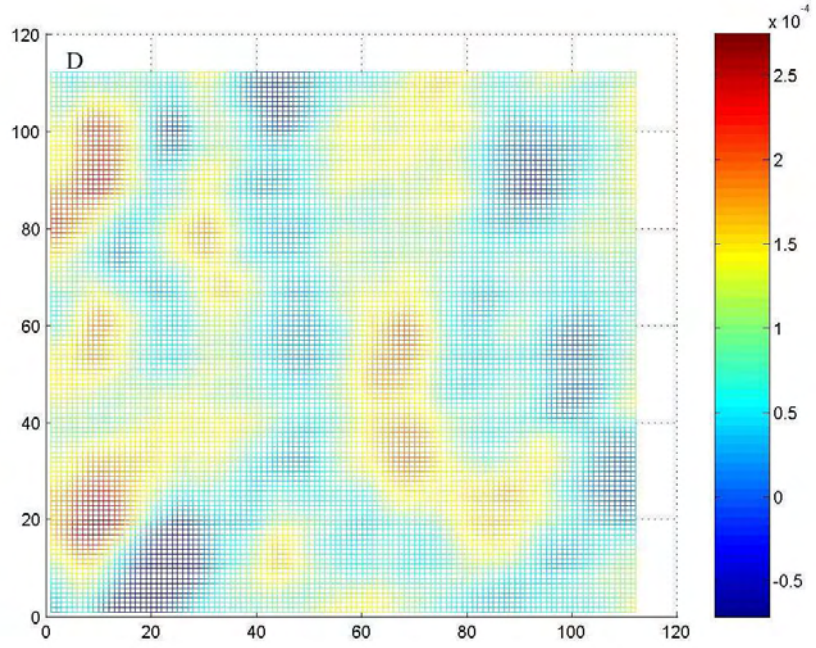
D
x 10^-4
2.5
2
1.5
1
0.5
0
-0.5
120
100
80
60
40
20
0
0
20
40
60
80
100
120

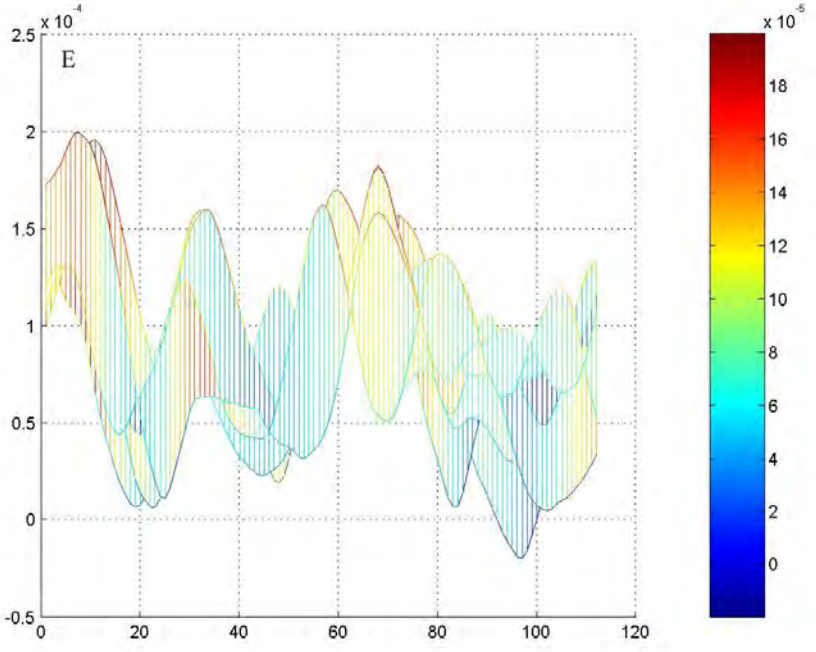
E
x 10^-4
2.5
2
1.5
1
0.5
0
-0.5
0
20
40
60
80
100
120
x 10^-5
18
16
14
12
10
8
6
4
2
0

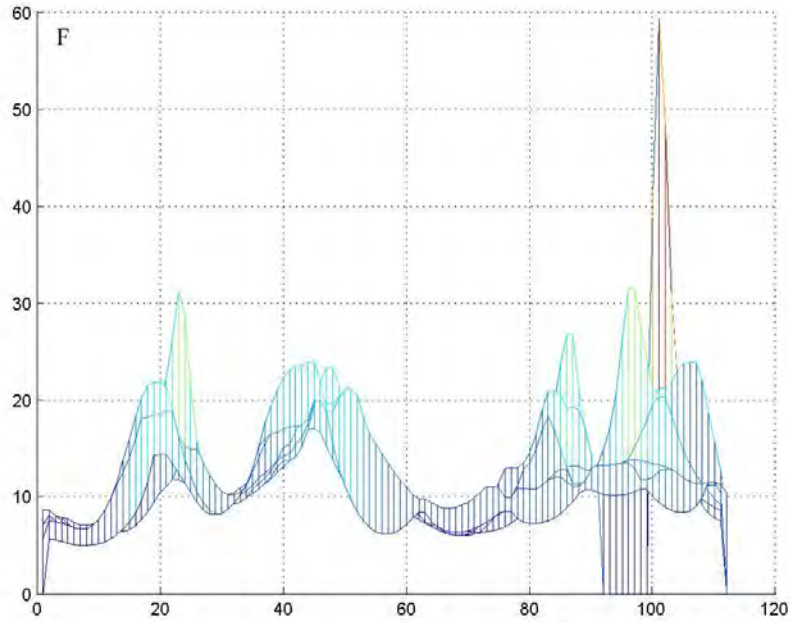
F
60
50
40
30
20
10
0
0
20
40
60
80
100
120

REFERENCES

1. Lowenstam, H., and S. Weiner, *On Biomineralization*, Oxford University Press, 1983.

2. Martin, R., and J. Ishida, "The relative effects of collagen fiber orientation porosity density and mineralization on bone strength," *Journal of Biomechanics*, Vol. 22, pp. 419–426, 1989.

3. Martin, R., "Determinants of the mechanical properties of bones," *Journal of Biomechanics*, Vol. 24, pp. 79–88, 1991.

4. Currey, J., "Effects of differences in mineralization on the mechanical properties of bone," *Philolosophical Transactions R. Soc. B Biol. Sciences*, Vol. 304, pp. 509–518, 1984.

5. Currey, J., "Role of collagen and other organics in the mechanical properties of bone," *Osteoporosis International*, Vol. 14, pp. S29–S36, 2003.

6. Nomura, S., A. Hiltner, J. Lando, and E. Baer, "Interaction of water with native collagen," *Biopolymers*, Vol. 16, pp. 231–246, 1977.

7. Pineri, M., M. Escoubes, and G. Roche, "Water-collagen interactions: calorimetric and mechanical experiments," *Biopolymers*, Vol. 17, pp. 2799–2815, 1978.

8. Robinson, R., and M. Elliot, "The water content of bone," *Journal of Bone Joint Surgery*, Vol. 39A, pp. 167–188, 1957.

9. Robinson, R., "Bone tissue: composition and function," *The Johns Hopkins Medical Journal*, Vol. 145, pp. 10–24, 1979.

10. Yamashita, J., X. Li, B. Furman, H. Rawls, X. Wang, and C. Agrawal, "Collagen and bone viscoelasticity: a dynamic mechanical analysis," *Journal of Biomedical Material Research*, Vol. 63, pp. 31–36, 2001.

11. Kishen, A., and A. Asundi, "Experimental investigation on the role of water in the mechanical behavior of structural dentine," *Journal of Biomedical Materials Research*, Vol. 73A, pp. 192–200, 2005.

12. Fois, M., A. Lamure, M. Fauran, and C. Lacabanne, "Study of human cortical bone and demineralized human cortical bone viscoelasticity," *Journal of Applied Poultry Sciences*, Vol. 79, pp. 2527–2533, 2001.

13. Fernandez-Seara, M., S. Wehrli, M. Takahashi, and F. Wehrli, "Water content measured by proton deuteron exchange nmr predicts bone mineral density and mechanical properties," *Journal of Bone and Mineral Research*, Vol. 19, pp. 289–296, 2004.

14. Weiner, S., and H. Wagner, "The material bone, structure mechanical function relations," *Annual Review of Material Science*, Vol. 28, pp. 271–298, 1998.

15. Alberts, B., D. Bray, J. Lewis, M. Raff, K. Roberts, and J. D. Watson, *The Cell*, New York: Garland Publishing, 1994.

16. Engel, J., and D. Prockop, "Does bound water contribute to the stability of collagen," *Matrix Biology*, Vol. 17, pp. 679–680, 1998.

17. Frost, H., *Orthopaedic Biomechanics*, Springfield: Charles C Thomas, 1973.

18. Jones, S., and A. Boyde, "Is there a relationship between osteoblasts and collagen orientation in bone?," *Israeli Journal of Medical Sciences*, Vol. 12, no. 2, pp. 98–106, 1976.

19. Hodge, A., and J. Petruska, *Aspects of protein structure*, ch. Recent studies with the electron microscope on ordered aggregates of the tropocollagen molecule, pp. 269–300. New York: Academic Press, 1963.

20. Yamauchi, M., E. Katz, K. Otsubo, K. Teraoka, and G. Mechanic, "Cross-linking and stereospecific structure of collagen in mineralized and nonmineralized skeletal tissues," *Connective Tissue Research*, Vol. 21, pp. 159–167, 1989.

21. Nyman, J., M. Reyes, and X. Wang, "Effect of ultrastructural changes on the toughness of bone," *Micron*, Vol. 36, pp. 566–582, 2005.

22. Hulmes, D., T. Wess, D. Prockop, and P. Fratzl, "Radial packing, order and disorder in collagen fibrils," *Biophysical Journal*, Vol. 68, pp. 1661–1670, 1995.

23. Jager, I., and P. Fratzl, "Mineralized collagen fibrils: a mechanical model with staggered arrangement of mineral particles," *Biophysical Journal*, Vol. 79, pp. 1737–1746, 2000.

24. Fratzl, P., "Cellulose and collagen, from fibres to tissues," *Current Opinion Coll. Interf. Sciences*, Vol. 8, pp. 32–39, 2003.

25. Trus, B., and K. Piez, "Compressed microfibril models of the native collagen fibril," *Nature*, Vol. 286, pp. 300–301, 1980.

26. Lees, S., and H. Mook, "Equatorial diffraction spacing as a function of water content in fully mineralized cow bone determined by neutron diffraction," *Calcified Tissue International*, Vol. 39, pp. 291–292, 1986.

27. Fratzl, P., N. F. Zelman, and K. Klaushofer, "Collagen packing and mineralization," *Biophysical Journal*, Vol. 64, pp. 260–266, 1993.

28. Vogel, A., and V. Venugopalan, "Mechanisms of pulsed laser ablation of biological tissues," *Chemical Reviews*, Vol. 103, no. 5, pp. 2079–2079, 2003.

29. Mecham, R., "Overview of extracellular matrix," *Current Protocols in Cell Biology*, Vol. 10.1, pp. 1–14, 1998.

30. Currey, J., *Bones: Structure and Mechanics*, New Jersey: Princeton University Press, 2002.

31. Timmins, P., and J. Wall, "Bone water," *Calcified Tissue Research*, Vol. 23, pp. 1–5, 1977.

32. Wilson, E., A. Awonusi, M. Morris, D. Kohn, M. Tecklenburg, and L. Beck, "Highly ordered interstitial water observed in bone by nuclear magnetic resonance," *Journal of Bone and Mineral Research*, Vol. 20, pp. 625–634, 2005.

33. Wilson, E., A. Awonusi, M. Morris, D. Kohn, M. Tecklenburg, and L. Beck, "Three structural roles for water in bone observed by solid state nmr," *Biophysical Journal*, Vol. 90, pp. 3722–3731, 2006.

34. LeGeros, R., G. Bonel, and R. Legros, "Types of water in human enamel and in precipitated apatites," *Calcified Tissue Research*, Vol. 26, pp. 111–118, 1978.

35. Marzec, E., and W. Warchol, "Dielectric properties of a protein-water system in selected animal tissues," *Bioelectrochemistry*, Vol. 65, pp. 89–94, 2005.

36. Cowin, S., "Bone poroelasticity," *Journal of Biomechanics*, Vol. 32, pp. 217–238, 1999.

37. Gao, H., B. Ji, I. Jager, E. Arzt, and P. Fratzl, "Materials become insensitive to flaws at nanoscale: lessons from nature," *Proceedings of National Academy of Sciences*, Vol. 100, pp. 5597–5600, 2003.

38. Rho, J.-Y., L. Kuhn-Spearing, and P. Zioupos, "Mechanical properties and the hierarchical structure of bone," *Medical Engineering and Physics*, Vol. 20, pp. 92–102, 1998.

39. Weiner, S., and L. Addadi, "Design strategies in mineralized biological materials," *Journal of Materials Chemistry*, Vol. 7, pp. 689–702, 1997.

40. Luciano, D., A. Vander, and J. Sherman, *Human Function and Structure*, New York: McGraw Hill, Inc., 1978.

41. Guille, M. G., "Twisted plywood architecture of collagen fibrils in human compact bone osteons," *Calcified Tissue International*, Vol. 42, pp. 167–180, 1988.

42. Weiner, S., L. Arad, I. Sabanay, and W. Traub, "Rotated plywood structure of primary lamellar bone in the rat: orientations of the collagen fibril arrays," *Bone*, Vol. 20, pp. 509–514, 1997.

43. Weiner, S., and W. Traub, "Bone structure: from angstroms to microns," *FASEB Journal*, Vol. 6, pp. 879–885, 1992.

44. Eanes, E., D. Lundy, and G. Martin, "X ray diffraction study of the mineralization of turkey leg tendon," *Calcified Tissue International*, Vol. 6, pp. 239–248, 1970.

45. Eanes, E., G. Martin, and D. Lundy, "The distribution of water in calcified turkey leg tendon," *Calcified Tissue International*, Vol. 20, pp. 313–316, 1976.

46. Bonar, L., S. Lees, and H. Mook, "Neutron diffraction studies of collagen in fully mineralized bone," *Journal of Molecular Biology*, Vol. 181, pp. 265–270, 1985.

47. Chippada, U., and D. Zhang, "Smd studies of effects of structural water on the stiffness of collagen," *Bone Fluid Workshop*, 2005.

48. Skedros, J., J. Holmes, E. Vajda, and R. Bloebaum, "Cement lines of secondary osteons in human bone are not mineral deficient: new data in a historical perspective," *The Anatomical Record Part A*, Vol. 286A, pp. 781–803, 2005.

49. Skedros, J., R. Bloebaum, K. Bachus, and T. Boyce, "The meaning of graylevels in backscattered electron images of bone," *Journal Biomedical Materials Research*, Vol. 27, pp. 47–56, 1993.

50. Langton, C., and C. Njeh, *The Physical Measurement of Bone*, Bristol: Institute of Physics Publishing, 2004.

51. Speciale, S., F. Jiang, C. Caylor, and S. Kriminski, "Sound velocity and elasticity of tetragonal lysozyme crystals by brillouin spectroscopy," *Biophysical Journal*, Vol. 85, pp. 3202–3213, 2003.

52. Carew, T., N. Ramesh, and D. Patel, "Compressibility of arterial wall," *Circulation Research*, Vol. 23, pp. 61–68, 1968.

53. Fung, Y., *Biomechanics. Mechanical properties of living tissues*, New York: Springer-Verlag, 1981.

54. Tanioka, A., T. Tazawa, K. Miyasaka, and K. Ishikawa, "Effects of water on the mechanical properties of gelatin films," *Biopolymers*, Vol. 13, p. 735, 1974.

55. Doty, S., R. Robinson, and B. Schofield, *Handbook of Physiology*, ch. Basic Biomechanics of the Musculoskeletal System, pp. 3–23. American Physiology Society, 1976.

56. Akiva, U., H. Wagner, and S. Weiner, "Modelling the three-dimensional elastic constants of parallel - fibred and lamellar bone," *Journal of Materials Science*, Vol. 33, no. 6, pp. 1497–1509, 1998.

57. Shahar, R., P. Zaslansky, M. Barak, A. Friesem, J. Currey, and S. Weiner, "Anisotropic poisson's ratio and compression modulus of cortical bone determined by speckle interferometry," *Journal of Biomechanics*, Vol. 40, no. 2, pp. 252–264, 2007.

58. Wagner, H., and S. Weiner, "On the relationship between the microstructure of bone and its mechanical stiffness," *Journal of Biomechanics*, Vol. 25, pp. 1311–1320, 1992.

59. Ziv, V., I. Sabanay, T. Arad, W. Traub, and S. Weiner, "Transitional structures in lamellar bone," *Microscopy Research and Technique*, Vol. 33, pp. 203–213, 1996.

60. Riggs, C., L. Vaughan, G. Evans, L. Lanyon, and A. Boyde, "Mechanical implications of collagen fibre orientation in cortical bone of the equine radius," *Anatomical Embryology*, Vol. 187, pp. 239–248, 1993.

61. Skedros, J., M. Mason, M. Nelson, and R. Bloebaum, "Evidence of structural and material adaptation to specific strain features in cortical bone," *The Anatomical Record*, Vol. 246, pp. 47–63, 1996.

62. Landis, W., "The strength of calcified tissue depends in part on the molecular structure and organization of its constituent mineral crystals in their organic matrix," *Bone*, Vol. 16, pp. 533–544, 1995.

63. Magne, D., P. Weiss, J.-M. Bouler, O. Laboux, and G. Daculsi, "Study of the maturation of the organic (type i collagen) and mineral (nonstoichiometric apatite) constituents of a calcified tissue (dentin) as a function of location: A fourier transform infrared microspectroscopic investigation," *Journal of Bone and Mineral Research*, Vol. 16, no. 4, pp. 750–757, 2001.

64. Yeni, Y., M. Schaffler, G. Gibson, and D. Fyhrie, "Prestress due to dimensional changes caused by demineralization: A potential mechanism for microcracking in bone," *Annals of Biomedical Engineering*, Vol. 30, pp. 217–225, 2002.

65. Nyman, J., A. Roy, X. Shen, R. Acuna, J. Tyler, and X. Wang, "The influence of water removal on the strength and toughness of cortical bone," *Journal of Biomechanics*, Vol. 39, pp. 931–938, 2006.

66. Rho, J., P. Zioupos, J. Currey, and G. Pharr, "Variations in the individual thick lamellar properties within osteons by nanoindentation," *Bone*, Vol. 25, pp. 295–300, 1993.

67. Katz, J., "The elastic anisotropy of bone," *Journal of Biomechanics*, Vol. 20, pp. 1063–70, 1987.

68. Park, H., and R. Lakes, "Cosserat micromechanics of human bone: strain redistribution by a hydration sensitive constituent," *Journal of Biomechanics*, Vol. 19, pp. 385–397, 1986.

69. Frasca, P., "Scanning electron microscopy studies of ground substance in the cement lines, resting lines hypercalcified rings and reversal lines of human cortical bone," *Acta Anatomica*, Vol. 109, pp. 114–121, 2001.

70. Jones, R., and C. Wykes, *Electronic Speckle pattern Correlation Interferometry*, Cambridge: Cambridge University Press, 1989.

71. Bedzinski, R., "Experimental methods of investigating bone structures and implants," in *ASME Summer Bioengineering Conference Proceedings*, (Snowbird, Utah), ASME Summer Bioengineering Conference, June 27-July 1 2001.

72. nie wicz, M. S., E. Gawin, and R. Bedzinski, "Application of electronic speckle pattern interferometry for " anisotropic mechanical behavior of bone," *Proceedings of Bioengineering Conference*, Vol. 50, pp. –, 2001.

73. Zhang, D., D. Arola, and J. Rouland, "Evaluating the elastic modulus of bone using electronic speckle pattern interferometry," *Experimental Techniques*, Vol. 25, no. 5, pp. 32–34, 2001.

74. Zaslansky, P., J. Currey, A. Friesem, and S. Weiner, "Phase shifting speckle interferometry for determination of strain and youngs modulus of mineralized biological materials: a study of tooth dentin compression in water," *Journal of Biomedical Optics*, Vol. 10, pp. 374–383, 2005.

75. Gamba, J., J. Forchelet, M. Cattani-Lorente, V. Chatelain, I. Krejci, and S. Bouillaguet, "Cuspal deformation during light-curing of resin-based restorative materials measured by espi (electronic speckle pattern interferometry)," *European Cells and Materials*, Vol. 7, no. 2, pp. 32–33, 2004.

76. Roman, J., P. Fernandez, V. Moreno, M. Abeleira, M. Gallas, and D. Suarez, "Behaviour of human mandibles studied by electronic speckle pattern interferometry," *European Journal of Orthodontics*, Vol. 21, pp. 413–421, 1999.

77. Lancaster, P., and K. Salkauskas, *Curve and Surface Fitting: An Introduction*, London: Academic Press, 1986.

78. Vidal, M., S. Kaup, W. Johnson, and T. Crenshaw, "Relationships among mechanical-properties and mineral-composition of femurs from miniature swine ranging in age from 0.4 to 14 years," *Journal of Bone and Mineral Research*, Vol. 10, p. S478, 1995.

79. Crenshaw, T., E. Peo, A. Lewis, B. Moser, and D. Olson, "Influence of age, sex and calcium and phosphorus levels on the mechanical-properties of various bones in swine," *Journal Of Animal Science*, Vol. 52, no. 6, pp. 1319–1329, 1981.

80. Handgraaf, J., and F. Zerbetto, "Molecular dynamics study of onset of water gelation around the collagen triple helix," *Proteins: Structure Function Bioinformatics*, Vol. 64, pp. 711–718, 2006.

81. Arsenault, A., "Image-analysis of collagen-associated mineral distribution in cryogenically prepared turkey leg tendons," *Calcified Tissue International*, Vol. 48, pp. 56–62, 1991.

82. Weiner, S., W. Traub, and H. Wagner, "Lamellar bone: structure-function relations," *Journal of Structural Biology*, Vol. 126, pp. 241–255, 1999.

83. Hengsberger, S., A. Kulik, and P. Zysset, "Nanoindentation discriminates the elastic properties of individual human bone lamellae under dry and physiological conditions," *Bone*, Vol. 30, pp. 178–184, 2002.

84. Liebermann, D., and A. Crompton, *Principles of Animal Design: the optimization and symmorphosis debate*, ch. Responses to bone stress: constraints on symmorphosis, pp. 78–86. Cambridge University Press, 1998.

85. Dullemeijer, P., *Principles of Animal Design: the optimization and symmorphosis debate*, ch. Optimality in the Design of Bony Elements, pp. 64–69. Cambridge University Press, 1998.

86. Maddrell, S., *Principles of Animal Design: the optimization and symmorphosis debate*, ch. Bone Design and Biomechanics, p. 63. Cambridge University Press, 1998.